GROWTH AND MAGNETISM OF LOW-DIMENSIONAL METALLIC NANOSTRUCTURES ON THE PT(997) SURFACE

Tae-Yon LEE

M.Sc. in Materials Science & Engineering, Séoul National University, Corée du Sud
et de nationalité coréenne

Abstract

The thesis presents experimental results on the growth and magnetism of metallic nanostructures on the vicinal Pt surface. The aim of the research project consists of two parts: First, to find conditions for growing nanostructures of dimensionalities from 1D to 2D initiated from the step edges of a vicinal surface. Second, to investigate the magnetic properties of the nanostructures and ultrathin films fabricated with the knowledge from the first part.

The first part of the thesis studies molecular beam epitaxy (MBE) of Fe, Rh, Ru, and Mo nanostructures on the vicinal Pt(997) surface for various temperatures employing thermal energy He atom scattering (TEAS), Auger electron spectroscopy (AES) and low electron energy diffraction (LEED) as characterizing methods. The parameters for the growth of a wide variety of Fe nanostructures, from monatomic chains to monolayers and surface alloys, were obtained and a detailed comparison of Fe growth on Pt(997) and Pt(111) is presented. Rh deposition creates structures similar to the ones of Fe although with higher defect density. A complex growth mode involving double layer growth is observed for Ru. For Mo no ordered structures could be identified.

In the second part of the thesis measurements by X-ray magnetic circular dichroism (XMCD) and magneto optical Kerr effect (MOKE) were employed as probes to the magnetic properties of the structures. Ultrathin Fe films show different magnetic properties depending on the step density of the substrate. The relation between magnetism and structure is shown by the comparison of films on Pt(997) and Pt(111). The variety of Fe structures characterized in the first part is investigated finding an increase of orbital magnetic moments when the dimension and thus the coordination in the structure is reduced. It is shown that a stabilization of the magnetization in Fe nanostructures which is reflected by an increased remanence and coercivity is achieved simply by alloying with Pt from the substrate. Finally, it is demonstrated that well measurable magnetic moments are induced in the Pt for a FePt alloy with a total Fe coverage of only 0.5 ML. The Pt moments are found to couple collinearly to the Fe moments.

Version abrégée

L'objectif de cette thèse est l'analyse de la croissance et du magnétisme de nanostructures métalliques deposées sur une surface vicinale de Pt(997). Le projet de recherche se concentre sur deux aspects: Tout d'abord, rechercher les conditions de croissance de nanostructures de dimension 1D et 2D obtenues par décoration des marches d'une surface vicinale. Puis, étudier les propriétés magnétiques des nanostructures et des couches minces élaboreés.

La première partie de cette thèse traite de la croissance par epitaxie par jet moléculaire de Fe, Rh, Ru et Mo sur la surface vicinale Pt(997) pour une gamme de température étendue. Les structures sont caracterisées en utilisant la diffusion d'Helium, la spectroscopie d'electrons Auger et la diffraction d'electrons lents. Les paramètres qui permettent la croissance de nanostructures de Fe ont été obtenus: chaines monoatomiques, monocouches et alliages de surface. Une comparaison detaillée de la croissance de Fe sur Pt(997) et sur Pt(111) est presentée. Le dépôt de Rh amène à des structures comparables à celle du Fe mais avec une densité de défaut plus elevée. Un mode de croissance compliqué, en bicouche, est observé pour le Ru. Pour le Mo aucune structure ordonnée est observée.

La deuxième partie de cette thèse utilise la méthode de dichroisme circulaire magnétique des rayons X ainsi que l'effet magnéto-optique Kerr afin d'étudier les propriétés magnétiques des structures. Les couches extrêmement minces de Fe présentent des propriétés magnétiques qui dépendent de la densité des marches. La relation entre le magnétisme et la structure est montrée en comparant les couches de Fe sur Pt(997) et sur Pt(111). Ensuite, la variété de structures de Fe identifiée dans la première partie est etudiée par du point de vue de magnétisme. Le moment orbital magnétique décroit avec la dimension et donc la coordination dans les structures. C'est montré que l'aimantation est stabilisée simplement par la formation d'une alliage de surface entre le Fe et le substrat de Pt. Cette stabilisation est mise en évidence par l'augmentation du champ rémanent. Finalement, il est demontré qu'il est possible de mesurer les moments magnétiques du Pt induit dans un alliage de FePt contenant seulement 0.5 monocouche de Fe. Les moments magnétiques du Pt sont collineaires aux moments du Fe.

Contents

Abbreviations and common symbols

fcc	face-centered cubic
bcc	body-centered cubic
hcp	hexagonal close-packed
TEAS	Thermal Energy He-Atom Scattering
LEED	Low-Energy Electron Diffraction
MOKE	Magneto-Optical Kerr Effect
XAS	X-ray Absorption Spectrum
MCD	Magnetic Circular Dichroism
XMCD	X-ray Magnetic Circular Dichroism
STM	Scanning Tunneling Microscopy
1D	One-Dimensional
2D	Two-Dimensional
3D	Three-Dimensional
s	seconds, unit of measurement time
min.	minutes, unit of measurement time
UHV	Ultra-High Vacuum
ML	monolayer
TEY	Total Electron Yield
MCA	Magneto-Crystalline Anisotropy
DOS	Density of States
LDOS	Local Density of States
SRT	Spin Reorientation Transition
POI	Plane of incidence of photons
Re	Real part of a complex argument
Im	Imaginary part of a complex argument

θ_j	Coverage of adsorbate j, (j = Fe, Rh, Ru, and Mo)
	θ_j=1 ML is the monolayer coverage defined for a pseudomorphic layer.
H	(applied) magnetic field
M$_s$	Saturation magnetization
M$_r$	Remanent magnetization
B	Magnetic induction, $\mathbf{B} = \mathbf{H} + 4\pi\mathbf{M_s}$ in cgs unit
μ_B	Bohr magneton, 1 μ_B = 5.79×10^{-5} eV/T
$\mathcal{E}$	Electric field
P	Electric polarization
D	Electric displacement, $\mathbf{D} = \mathcal{E} + 4\pi\mathbf{P}$ in cgs unit
E	photon energy (if not otherwise stated)
E_F	Fermi energy level
n	principal quantum number
l	orbital quantum number
m_l	magnetic quantum number
s	spin quantum number
μ	absorption coefficient of photons
m_S	spin magnetic moment
m_L	orbital magnetic moment
k_B	Boltzmann constant, k_B = 0.087 meV/K
T	(substrate) temperature
E_{MCA}	Magneto-crystalline anisotropy energy

Chapter 1

Introduction: Low-dimensional magnetic nanostructures

Magnetism is one of the physical properties which is in widespread use and affects our life. Magnetic storage devices are one example. Since the introduction of the magnetic tape for data storage, significant progress has been made in miniaturization while increasing access speed and storage capacity. As a result, the physical length scale of the smallest unit for writing information, *i.e.* the bit, has been reduced to the μm scale and finally reached the **nm** scale nowadays. In devices with **nm** scale bits such as hard-disk drive[1,2] , magneto-optical disk[3] , magneto-resistive random access memory (MRAM)[4] , *etc.*, new technological issues such as the information instability, small reading sensitivity, and large noise level emerge. These issues are linked to fundamental properties such as magnetic anisotropy, magnetic moments, superparamagnetism, exchange interactions, *etc*[1–5] . Thus, understanding such fundamentals of nanoscale magnetic structures becomes more and more important.

Those magnetic properties of nanostructures are closely related to the dimensionality, local symmetry and hybridization at the interface, which result in distinctive magnetic properties which are usually different from bulk magnetism[6–10] ; Magneto-crystalline anisotropy energy and orbital magnetic moment increase as the dimension of nanostructures decreases[11–13] . At the interface of ferro- and antiferro-magnetic materials, large exchange biased interactions occurs[14,15] . Atoms like Pt or Pd, which are paramagnetic in the bulk, show magnetic moments induced by neighboring ferromagnetic elements[16] . These phenomena become significant on the **nm** scale.

In this thesis, an effort is made to link the structural characteristics to the magnetic properties of nanostructures: In the first part the thesis will focus on the growth of Fe, Rh, Ru, and Mo ordered nanostructures on the vicinal Pt single crystal surface,

for coverages from monatomic chains to several monolayers. In the following part, the magnetism of Fe nanostructures will be presented. Through control of the atomic scale ordering of adlayers, an understanding of the relation between adlayer's structure and resulting magnetism can be obtained. This study will point out that the array of surface steps can facilitate growth of monatomic chains, layered adlayer structures, and ordered surface alloys. It will be shown from the comparison of Fe on Pt(997) and on Pt(111) that such morphologies and the local symmetry of adlayers result in different magnetic properties. For Fe atomic chains on Pt(997), a large increase of orbital magnetic moment and the oscillation of the easy magnetization direction with chain width will be reported. It will be shown that alloying of Fe and Pt at the surface increases the hybridization at the interface to show several important properties: stabilization of perpendicular anisotropy, induction of a magnetic moment on the Pt atoms, and collinear coupling of the magnetic moments on Fe and Pt.

This section will introduce methods to make ordered nanostructures in Sec.1.1, and the use of Pt(997) as a template for nanostructures in Sec.1.2. The structure of this thesis will be given in Sec.1.3.

1.1   How to prepare ordered nanostructures

An object of a certain volume can be made in two ways: either sculpturing from bulk source material which has a larger volume in comparison to the intended object, or making a mosaic starting from tiny source material whose volume is far less than that of the object. In making small structures, the former is typically referred as *top-down*, and the latter is called *bottom-up* approach.

The mass production of multi-layered thin film devices has been developed through *top-down* technologies as optical projection lithography and etching[17] . The limit of this method is the diffraction limit given by the wavelength of the incident beam. X-rays[18] or electron-beams[19] have been used as beam sources with smaller wavelength. However, such technologies become very expensive: X-ray lithography requires synchrotron radiation and electron-beam lithography requires ultra-high vacuum. Several methods in the projection scheme are still pursued with novel ideas such as optical interference lithography[20, 21] . On the laboratory level, direct writing with electron-beams[22] is used. Combined with reactive-ion-etching, this method can provide a good resolution of nm size of almost any kind of material. A drawback is the long time to obtain an intended object. Recently, an imprinting technique, in which a compression molding is used to

create a thickness contrast pattern[23] , is reported. Because the technique does not require lithography and an etching process, the time required to fabricate nanostructure with a resolution of 10 nm requires only a few seconds[24] .

Bottom-up approaches use the inherent properties of the materials: self-replication or self-assembling. It was von Neumann[25] who first pointed out in the early 1940's the role of a universal computer and a universal constructor. Because atoms, molecules, or nanoparticles (universal constructors) feel coulomb interaction, van der Waals interaction, hydrophilic/hydrophobic interaction, short-range repulsive force, *etc.* (universal computers), the constructor always positions in the right place in a parallel process, as usually observed in viruses or bio-molecules. Because of its parallelism, the self-assembly approach is not time consuming[26] . Naturally, bio-molecules are good examples of self assembled nanostructures. Furthermore, bio-molecules can be used as a template for nanostructure formation. For instance, the tobacco virus was successfully adopted as a template of Fe nanowires[27] . Chemistry also offers several methods. The repeated anodization and oxide removal on an Al surface has been used to form anodized-aluminum-oxide (AAO)[28] , which contains a periodic array of pores elongated perpendicular to the surface on a few hundred nm scale. AAO has been demonstrated as a template for the array of carbon nanotubes[29,30] , ZnO[31] , Nb[32] *etc.* Block-copolymers[33] , using the separation of a mixture of two polymers into a periodic array of nm domains, provides a template for periodic nanostructures. Arrays of nano dots of Co[34] , NiFe, CoFe/Cu/NiFe[35] , *etc.* have been successfully fabricated from templates prepared by block-copolymers. Certain organic molecules, which self-organize to show periodic arrangements, have been studied to obtain arrays of magnetic nanostructures, such as nanoparticles of PtFe[36] , CoRh, CoRu[37] , Co[38] , *etc.* Other contributions are from surface science: In epitaxial systems the formation of dislocation networks can define a periodic arrangement of hexagonal cells surrounded by diffusion barriers[39] . The network can be employed to grow a separate adatom cluster in each cell with high uniformity. The dissolution and formation of random islands around grains is also a possibility to form nanostructures.

Even though *bottom-up* approaches are attractive, long range chemical ordering, and magnetic ordering, required for mass production of nanoscale magnetic devices have not yet been achieved. Therefore, hybrid methods connecting *bottom-up* characteristics of materials and *top-down* control of ordering are required. Introducing regular defects by lithography to generate heterogenous nucleation of nano-particles can be one of the promising methods[40,41] .

1.2 Vicinal Pt(997) single crystal as a template for the growth of atomic nanostructures

Not many methods are available for the generation of atomic nanostructures. It is possible to manipulate single atoms by the lateral movement of STM tips[42, 43] , which is a serial process and thus time-consuming. Another method can be the use of a vicinal single crystal surface as a template, such as Pt(997).

Surfaces with low crystallographic indicees are usually the ones with the lowest surface free energies[44] as the atoms at the surface experience a maximum of average coordination to neighboring atoms. In comparison to insulator and semiconductor surfaces a low index metal surface exhibits a low terrace diffusion barrier. As a result of these two properties a single crystal low index metal surface often represents the energetically most stable arrangement which, in addition, can be established already at moderate temperature. Such a surface can be well prepared in UHV, typically by repeated cycles of sputtering and annealing. During sputtering, adsorbates and contaminants close to the surface are removed while the following annealing significantly reduces the defects created during sputtering[45, 46] . Well prepared single crystal surfaces contain wide terraces of typical widths of 10 to 100 nm with single atomic height steps and kinks. These surface defects cannot be removed completely because of a non-zero miscut angle with respect to the low index surface and of the non-vanishing disorder due to the thermodynamic entropy term.

However, one can purposely choose a miscut angle to obtain *periodic arrays of steps of monolayer height*. The growth of ultrathin layers on a vicinal surface exhibits several advantageous properties in comparison to low index surfaces with respect to growth and alloying behavior. First, true one and two dimensional structures can be formed by step edge decoration, suppressed island nucleation on terraces and forced layer-by-layer growth. Second, alloying can be promoted due to a facilitated intermixing at step edges[47] . It is experimentally found that a stable staircase structure can be obtained for several surfaces such as Pt(997)[48] , Pt(779), Si(557)[49] , vicinal Au(111)[50] , *etc.*

In this work, a Pt(997) single crystal is used for the formation of metallic magnetic nanostructures for several reasons: First, the surface can be prepared reproducibly to result in a regular array of steps and terraces[48] . Compared to other metals, Pt is less sensitive to contamination. Second, previous studies show that the Pt(997) surface can be used as a template for the formation of 1D nanostructures of various metals such as Co,[51] Ag[52] , and Cu[53] . Third, the magnetic properties of the adlayer on Pt can be tuned due to the magnetic coupling between adlayer and Pt atoms through electronic

(a)   (b)
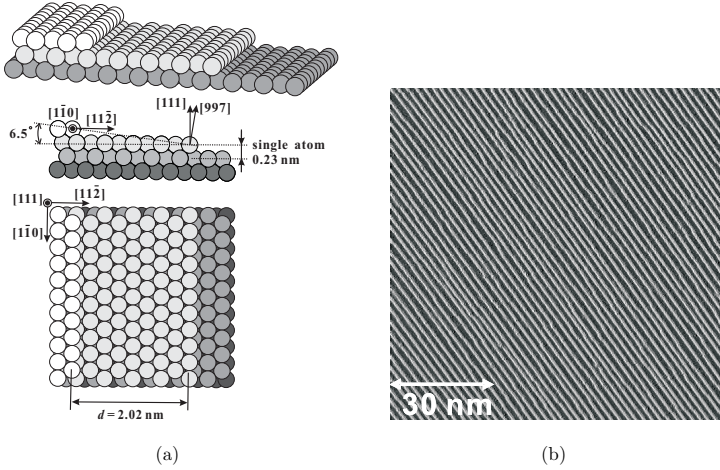
Figure 1.1 (a) Sketch of the atomic arrangement on the Pt(997) surface in perspective view (top), side view (center) and top view (bottom). (b) Constant current STM image of the well prepared Pt(997) surface measured at 7 K. Tunnelling current was 0.108 nA at 0.39 V bias voltage. For clarity, the image is presented in a lateral differentiation $\partial z/\partial x$.

hybridization. Like Pd, Pt is highly polarizable and exhibits an induced magnetic moment through the hybridization due to the large density of states at the Fermi level even though bulk Pt is paramagnetic[54–56].

Fig.1.1(a) shows the schematic diagram of the ideal Pt(997) surface. The surface consists of 8 atoms wide close-packed (111) terraces separated by steps with a (11$\bar{1}$) microfacet of monolayer height, also called B-type steps. The surface is well ordered with an average step-step distance of 20.2 Å and a standard deviation of 2.9 Å[48].

The clean and ordered Pt(997) surface is prepared by repeated cycles of 1 keV Ar$^+$ sputtering at 750 K surface temperature and annealing at 850 K. In order to avoid freezing-in defects which are created at high temperature, the sample was cooled down slowly with a rate below 40 K/min. Fig.1.1 (b) shows that the thus prepared surface has an ordered staircase structure over a large area. Results from surface sensitive diffraction methods such as TEAS or LEED typically show that ordering can be obtained in an area as large as 5×5 mm^2.

From these reasons, Pt(997) is expected to be one of the best-suited templates for the formation of metallic nanostructures. Fig.1.2 shows an example of the decoration of Fe monatomic chains at the steps of Pt(997). It is readily shown that an array of
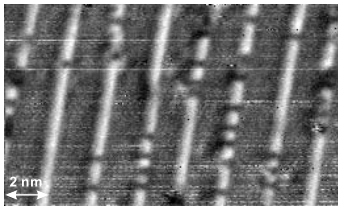
Figure 1.2 STM image (dI/dV map) of 0.13 ML Fe decorating the step edges of the Pt(997) surface, measured at 7 K. The tunnelling parameters are $I = 1.08$ nA, $V = 0.39$ V, and 4.6 kHz lock-in modulation of the bias voltage by 20 mV.

straight Fe chains with relatively few defects are formed.

1.3   The structure of this thesis

Chap.1 presented a general introduction of the method to obtain periodic nanostructures and the vicinal Pt(997) single crystal surface. The following parts of this thesis comprise mainly two topics; Chap.2 presents the growth of Fe, Rh, Ru, and Mo nanostructures on Pt(997) and Fe on Pt(111), and Chap.3 contains studies of the magnetism of Fe nanostructures on Pt(997) and Pt(111).

The description of Thermal Energy He-Atoms Scattering (TEAS), a major method to study *in-situ* the adlayer growth on Pt(997), will be given in Sec.2.1. The investigation of the role of local coordination and symmetry of the nanostructures in their magnetic properties is the motivation of the study of Fe growth on Pt(997) and Pt(111) in Sec.2.2 and Sec.2.3. Sec.2.2 presents the conditions for the formation of Fe monatomic chains at the steps of Pt(997), the growth of Fe monolayer, and the formation of Fe-Pt monolayer alloy. For comparison, the growth of Fe on the flat Pt(111) surface is studied by low energy electron diffraction (LEED) in Chap.2.3, which shows 3D island growth of Fe in contrast to step-flow growth of Fe on Pt(997).

Calculations on $4d$ metals showing large local magnetic moment in low-dimensional structures of Rh, Ru, and Mo[57–59] motivated the study of the growth of those metals on the Pt(997) surface by TEAS (Chap.2.4): Rh and Ru show layer-by-layer growth on Pt(997). On the other hand, 3D island growth of Mo on Pt(997) is observed. With a summary, an attempt is made to find a physical parameter which is correlated to the quality of step decoration observed on Pt(997) (Chap.2.5) .

Magnetic properties of a variety of Fe nanostructures on Pt(997) will be presented in Chap.3. Two complementary experimental methods, the X-ray Magnetic Circular Dichroism (XMCD) and the Magneto Optical Kerr Effect (MOKE), will be introduced in Sec.3.1. The magnetism of Fe on Pt(997) studied by XMCD will be discussed in Sec.3.2. First, differences of the magnetism of Fe on Pt(997) and Fe on Pt(111) will

be presented: In comparison to Fe on Pt(111), a strongly enhanced perpendicular magnetization is observed for Fe on Pt(997). It will be pointed out in Sec.2.2 and 2.3 that the different magnetic properties found for the two systems are connected to the different morphology and lattice symmetry of the Fe layer on the two surfaces. Second, a dramatic increase in orbital magnetic moment with decreasing Fe coverage and an oscillatory magnetic anisotropy variation as a function of Fe chain width on Pt(997) will be presented. Based on the systematic change of the local coordination in Fe chains as a function of their width, an attempt is made to explain those two observations in terms of the variation of the local crystal field. Third, the magnetic properties of the ordered Fe-Pt surface alloy on Pt(997) will be presented: Enhanced hybridization between Fe and Pt atoms results in induced magnetic moments on Pt atoms. Moreover collinear coupling of the magnetic moments of Fe and Pt, a strongly enhanced orbital magnetic moment of Fe whose magnitude is comparable to the case of an Fe monatomic chain, and dramatically increased perpendicular magnetic anisotropy of the ordered Fe-Pt surface alloy will be presented. The magnetism of Fe layers on Pt(111) is also studied by MOKE in Sec.3.3.

After conclusion in Chap.4, the on-going projects related to the study of this thesis are presented in Sec.5. The possibility of the use of a kinked vicinal single crystal surface as a template for nanostructure formation will be discussed in Sec.5.1. In Sec.5.2, the magnetism of $4d$ metals and a first trial of XMCD measurements of Rh on Pt(997) and Ag(001) will be presented.

Two chapters are given as an appendix. Appendix A explains the calculation of the magneto-crystalline anisotropy energy E_{MCA} from the local crystal field based on the pair interaction model. Appendix B discusses artifacts observed in XMCD experiments resulting from the trajectories of secondary electrons in a magnetic field. An improved method to remove the artifacts in the measurements of hysteresis loops by XMCD will be given.

Chapter 2

Growth of low-dimensional
metallic nanostructures on Pt(997)

This chapter introduces the principles of thermal energy atom scattering (TEAS) (Sec.2.1). From the combined use of TEAS with other methods such as scanning tunnelling microscopy (STM), low energy electron diffraction (LEED), Auger electron spectroscopy (AES), the structure and growth of Fe (Sec.2.2), Rh, Ru, and Mo (Sec.2.4) on Pt(997) of the coverage from a monatomic row to several ML were studied *in situ*. The growth and microstructure of Fe on Pt(111) is studied by LEED in Sec.2.3.

LEED and TEAS are surface diffraction methods. The information of surface structure which they provide is averaged over a macroscopic area determined by the lateral size of the incident beam. The beam diameter is of the order of 1 mm for the He beam and about one order of magnitude smaller for the electron beam. The penetration depth of the electron beam used for LEED is typically several ML. Therefore, the resulting information always carries information from the top-most layer as well as underlayers. On the other hand, the information of TEAS is exclusively from the top-most layer because of the low energy of the incident He-beam and its strongly repulsive interaction with surface atoms. This section briefly introduces TEAS which was used for the study of Fe, Rh, Ru, and Mo growth on Pt(997) in Sec.2.2. Detailed explanations of the principles of LEED[60] , AES[61] , and STM[62] which are standard surface science techniques, as well as TEAS[63] can be found in the references.

2.1 TEAS as a tool to study the growth and structure at surfaces

2.1.1 Principles and applications

Principles

In a He scattering experiment, a monochromatic beam of neutral He atoms is directed to the sample surface and its scattered intensity is measured by an ionization detector. A supersonic expansion of the He gas from a nozzle into the vacuum results in a He beam of the energy range 10-100 meV depending on the nozzle temperature. Because of such a low kinetic energy of the incident He beam, the interaction between He atoms and the surface is dominated by two contributions: A weak long-range attractive potential due to van der Waals force and a stronger short-range repulsive potential from Pauli's exclusion principle which prohibits the overlap between the electronic cloud of the He atoms and the electrons of the solid at the surface[63] . In a classical picture, the reflection of the He atoms takes place around 3-4 Å above the surface atom cores as in Fig.2.1. Therefore the He beam does not penetrate the sample and the scattering happens exclusively from the top-most surface layer.

Determination of surface structures

Because the de Broglie wavelength of the He beam is comparable to the interatomic distances of a typical solid surface, structural information of the periodic crystalline surface can be obtained from the diffraction of TEAS.

For instance, a scattering geometry as in Fig.2.2 can be considered where the plane of He-beam incidence is taken to be perpendicular to the steps. The angles θ_i and θ_f are
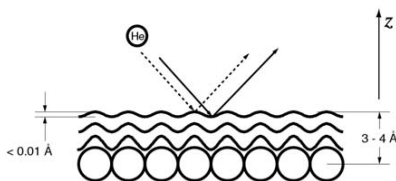
Figure 2.1 He atom being reflected from a crystal surface.
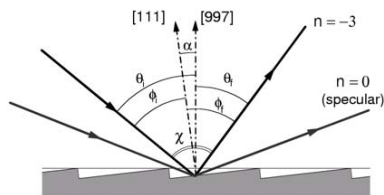
Figure 2.2 Sketch of step-down scattering from the vicinal Pt(997) surface.

defined with respect to the [997] direction which is normal to the macroscopic surface, and ϕ_i and ϕ_f are defined with respect to the [111] direction which is normal to the microscopic terrace. These values are inter-related as $(\theta_i, \theta_f) = (\phi_i + \alpha, \phi_f - \alpha)$ where $\alpha = 6.45°$ is the miscut angle of the fcc(997) surface with respect to the fcc(111) surface. $\chi = \theta_i + \theta_f = \phi_i + \phi_f$ is the total scattering angle. Then, the scattered intensity I can be described as a product of the structure factor G and the shape factor A as following:

$$I = cA^2G^2 \tag{2.1}$$

where c is a normalization constant. The structure factor G determines the position of the diffraction peaks and is given by the one-dimensional Bragg equation for the case of the scattering geometry in Fig.2.2[64] :

$$G^2 = \sum_n \delta(\sin\theta_f - \sin\theta_i - \frac{n\lambda}{d}) \tag{2.2}$$

where λ is the wavelength of the He-beam, n the diffraction order, and d the terrace width. The shape factor A can be obtained on the assumption that the He-beam is a plane wave and incident on a rectangular slit which corresponds to the illuminated part of one substrate terrace[64] :

$$A^2 = \frac{\sin^2(\beta/2)}{(\beta/2)^2} \tag{2.3}$$

$$\text{with } \beta = \frac{2\pi}{\lambda}\,\widetilde{d}\,(\sin\phi_i - \sin\phi_f) \tag{2.4}$$

$$\widetilde{d} = h \cdot (\frac{1}{\tan\alpha} - \tan\phi_i) \tag{2.5}$$

where h is the single step height which is 2.27 Å for the Pt(997) surface, and $\widetilde{d}$ corresponds to the width of the terrace illuminated by the He-beam. Fig.2.3 shows a typical diffraction pattern of a clean and well ordered Pt(997) surface.
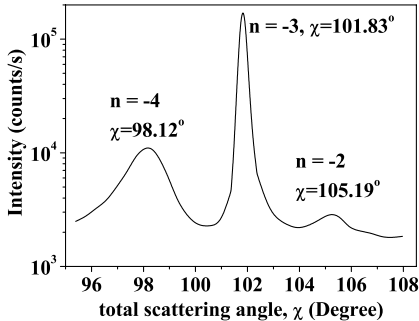
Figure 2.3 A typical TEAS diffraction pattern of the clean Pt(997) surface measured at $T = 500$ K with λ=0.85 Å, $\theta_i = 57.8°$. Several diffraction peaks with order $n = -2$, -3, and -4 appear which satisfy Eq.(2.2)

11

In situ characterization of the adsorbate growth

There are three typical growth modes[65, 66] of adsorbates on the solid surface: (a) Frank-van der Merwe or layer-by-layer mode, (b) Volmer-Weber or 3D island growth mode, and (c) Stranski-Krastanov or layer formation followed by 3-D island growth mode. These growth mode can be determined by investigating the diffraction intensity during the growth of adsorbates on the single crystal surface. The relationship between the growth modes and the change of the diffraction intensity with coverage is summarized in Fig.2.4. Because diffraction is the result of the constructive interference of the wave scattered from the periodic array of the objects, changes in the diffraction intensity during surface decoration allow to identify the growth mode: In the Frank-van der Merwe growth mode (Fig.2.4 (a)), there is an oscillation in the defect density as a function of the coverage. Therefore, the diffraction intensity *in situ* measured during the adsorbate growth on the surface also shows oscillation in its intensity as in Fig.2.4 (d), in which the minima and maxima of the intensity correspond to the maxima and minima of the defect density. The maximum of the diffraction intensity corresponds to monolayer completion when the oscillation occurs with a periodicity of 1 ML. For the Volmer-Weber growth mode, there is a continuous increase in the defect density at the surface during the growth. As a result, there occurs diffuse scattering of the beam leading to a continuous decrease in the diffraction intensity during the growth
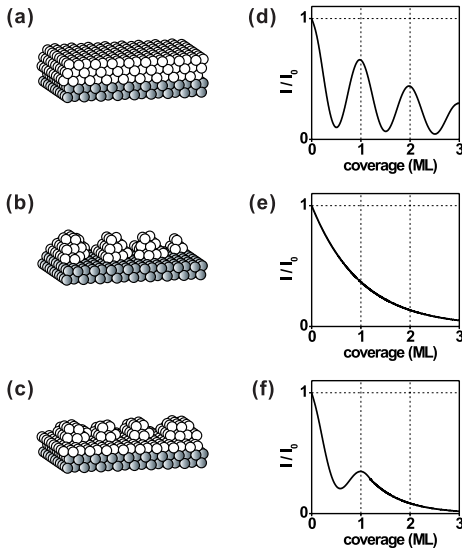
Figure 2.4 Three principal growth modes and the corresponding variation of diffraction intensity *in situ* measured during an adlayer (white circles) growth on the surface (gray circles): (a) and (d) for Frank-van der Merwe mode; (b) and (e) for Volmer-Weber mode; (c) and (f) for Stranski-Krastanov mode. Because of the finite amount of defects such as kinks, steps, *etc.*, the maxima of normalized intensity are not exactly 1.0 at 1, 2, 3, $\cdots$ ML for the case of the Frank-van der Merwe growth mode (d)

of the adsorbate (Fig.2.4 (b) and (e)). In the case of Stranski-Krastanov growth mode (Fig.2.4 (c)), the diffraction intensity as a function of coverage will show oscillation up to a critical thickness (1 ML for the case in Fig.2.4 (c) and (f)) and a continuous decrease when the growth mode has become three-dimensional.

A proper choice of the scattering conditions from the consideration of the surface geometry of Pt(997) in Fig.2.2 and the diffraction condition from Eq.(2.2) allows site selective studies of the growth mode[52,53,67] : In the case of grazing incidence geometry, for instance when $\theta_i = \theta_f = 85°$ and hence $n = 0$ in Eq.(2.2), the scattering happens exclusively at the step-edges. On the other hand, a more perpendicular incident scattering geometry, for instance when $\theta_i = 57.8°$, $\chi = 101.8°$, $n = -3$ for $\lambda = 1.01$ Å, provides information from the whole terrace. These two scattering geometries are used in the growth study of Fe on Pt(997) which follows in Sec.2.2.

Study of surface dynamics and reactions

In addition to studies of surface structure and growth, He scattering can also be used for other types of measurement. Because of the low thermal energy with small wavelength, TEAS can be used for the study of surface phonons[68–70] : From the inelastic scattering conditions, the phonon dispersion relations along high symmetry directions of the surface can be determined from energy and momentum transfer.

TEAS can also be used to probe various surface reactions[71] such as the chemisorption of H_2, O_2, CO, *etc.* at the step edges[72] , surface alloying[73–75] , *etc.*.

Such measurements are, however, not employed in this thesis with the exception of alloying kinetics in Sec.2.2.

2.1.2 Experimental setup

The TEAS instrument is shown in Fig.2.5. It consists of the three main modules: He-beam generation (***I-III*** in Fig.2.5), sample preparation and scattering chamber (***IV***), and detection (***V-VIII***). The detailed conception of the instrument is described elsewhere[76–79] .

The He beam is generated in chamber ***I*** by a nozzle[80,81] with an aperture of 10 μm diameter. Its temperature can be stabilized between 50 K and 350 K by resistive heating against the constant cooling power by a helium cold head coupled through a copper braid. Depending on the selected temperature the stagnation pressure in
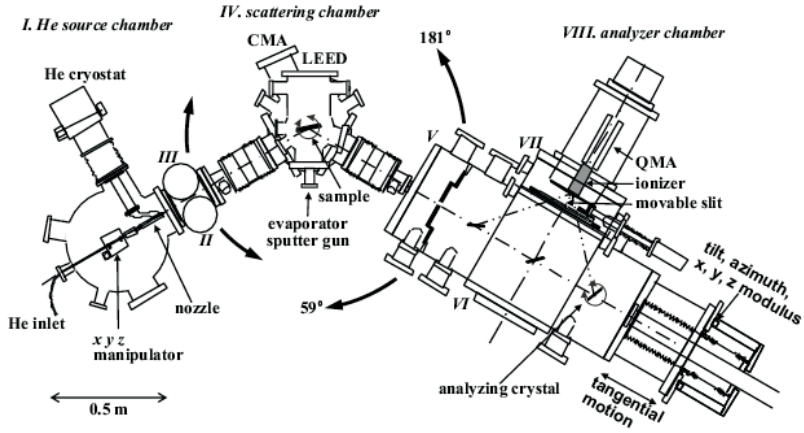
Figure 2.5 Top view of the TEAS experimental setup.

the tube which ends in the nozzle is chosen between 100 and 300 bars. The limiting parameter for the stagnation pressure is the pressure in the vacuum chamber where the nozzle is located and in which the vacuum is sustained by a 6000 l/s diffusion pump. The diffusion pump is boosted by a roots pump. In chamber I the pressure is about 10^{-5} mbar.

Two skimmers with diameters 0.28 and 0.20 mm are located between chamber I and II and between chamber II and III, respectively. The skimmers collimate the supersonic beam and serve as apertures for the differential pumping states. Each of the chambers II and III is pumped by a turbomolecular pump. A pinhole with diameter 0.23 mm is located between chamber III and the sample chamber. The divergence of the beam of 0.07 ° is determined by the size of the pinhole. The wavelength of the He beam, λ, can be set between 0.5 Å and 1.5 Å (80 to 10 meV in energy) by adjusting the nozzle temperature. The monochromaticity of the beam, $\Delta E/E$, is typically 1.5 %.

The scattering chamber is mounted on a motorized rotary table (supplier: Franke GmbH). The precision of angular positioning is better than 0.01 °. The axis of rotation defines the main axis of the instrument. The scattering chamber is connected to the nozzle chambers and to the detector chambers by flexible bellows. Those bellows allow to rotate the chamber by ± 30.5 ° with respect to a "neutral position" in which there is no lateral strain on the bellows.

The sample is mounted on a manipulator with six degrees of freedom (three for linear positioning on the axis of the chamber and three angles for the surface

orientation: tilt, polar angle, and azimuth). The sample can be cooled by a cooling finger through which a flow of liquid He or liquid nitrogen can pass. The sample is heated by electron bombardment from a tungsten filament close to its backside. To achieve temperatures up to 700 K radiative heating from the filament is sufficient; for higher temperatures an accelerating voltage of 600 V is applied between sample and filament. By use of liquid nitrogen cooling the accessible temperature range for the sample is 100 K to 1400 K. Temperatures below 30 K can be achieved using liquid He. The sample can be prepared by use of an ion sputter gun and several metal evaporators (Omicron single EFM and triple EFM3 evaporators). Four different elements can be deposited when the sample is in the He scattering position (*i.e. in situ*). In different positions the sample can be characterized by LEED and AES (Omicron CMA 100). A magnetic turbo-molecular pump is used for the vacuum of the sample chamber. It is backed by a small turbo-molecular pump necessary to achieve a sufficient compression ratio for He gas. The base pressure in the sample chamber is 2×10^{-10} mbar. Upon admitting the He beam into the chamber the ionization gauge indicates 1×10^{-9} mbar, which corresponds to an additional He pressure of approximately 6×10^{-9} mbar.

The differentially pumped chambers *V* to *VIII* contain the energy analysis and detection unit. The He background pressure must be reduced strongly in chamber *VIII* where the ionization detector is located. The detection unit is mounted on a frame which rests on air cushions and which slides over a polished granite plate. It moves on a circle centered on the main axis of the sample chamber. A robotic rotary motor (Megatorque motor) drives the rotation. The detection unit can be rotated by $\pm$ 30.5 ° with respect to the scattering chamber. A Pt(111) and a Pt(997) crystal are mounted on a manipulator with six degrees of freedom (x, y, z, tilt, polar, azimuth). The precision of the displacements in x, y and z direction is 0.1 mm, the precision of the polar angle is $\pm$ 0.001 °. The Pt(997) crystal can be employed as an energy analyzer[82] . In the measurements shown in this thesis, however, the Pt(111) surface is used for reflecting the He beam into the detector. To keep both surfaces clean over a long period of time the analyzer chamber *VI* is filled with an atmosphere of 5×10^{-9} mbar of oxygen and 5×10^{-7} mbar of hydrogen[78] . The electron beam ionizer situated in chamber *VIII* is based on a Stern-Pirani type manometer. It stores the incoming He flux for a short time and thus increases the ionization probability of the He atoms. This set-up is more favorable for the new analyzer setup than "open" ionizers whose detection efficiency depends in a complicated way on the angle between incoming beam and detector axis. The He ions created in the ionization chamber pass through a quadrupole mass spectrometer set to the mass m=4 (He) and are counted by a channeltron multiplier.

The background counting rate of the detector is about 30 counts/s. The contribution from the adjacent peak m=2 (H_2) is negligible. The counting rate of the He beam passing from the nozzle chambers directly into the analyzer-detection unit (without scattering from a sample) can reach 5 million counts/s.

A typical preparation procedure of the sample in TEAS is as follows: The clean and structurally ordered Pt(997) surface was prepared by repeated cycles of sputtering and annealing at $T = 900$ K. The cleanliness of the surface is checked by AES and the ordering of the substrate staircase structure is monitored by the absolute peak intensities and line shapes in the He diffraction pattern as in Fig.2.3. *In situ* characterization of the growth of adlayers was carried out by recording the intensity of a diffraction peak during deposition. A typical deposition rate of $R \simeq 0.1$ ML/min is employed at a background pressure during evaporation of 3×10^{-10} mbar. The deposition rate is calibrated from the He intensity oscillations observed at non-grazing scattering geometry (see Sec.2.2.3).

2.2   Growth of Fe on Pt(997)

The growth of ultra-thin layers of Fe on the vicinal Pt(997) surface is studied by TEAS between surface temperatures of 175 K and 800 K. Three temperature ranges with qualitatively different growth types are found: Below 450 K the formation of a smooth monolayer is observed. For temperature higher than 600 K, the onset of bulk alloy formation is found. At intermediate temperature 500 K $\sim$ 550 K the formation of a surface restricted alloy is identified. The decoration of the substrate steps by monatomic Fe rows is observed between 175 K and 500 K. The role of the steps in the growth and alloying processes and the kinetics of alloying will be discussed in this section.

2.2.1   What is expected for Fe growth on Pt(997) ?

The preparation of FePt alloy films is of substantial interest for the study of magnetism, both from the fundamental and applied point of view. Due to several fascinating magnetic properties such as high coercivity and saturation magnetization, strong perpendicular anisotropy, *etc.* FePt alloy thin films have attracted interest by their application in the storage device miniaturization such as perpendicular magnetization media. Alloys with alternatingly stacked Pt and Fe layers with L_{10} or L_{12} ordering have been the subject of intense research with respect to preparational methods[83] and their properties of morphology and magnetism[84] . Numerous studies on such systems with comparatively large thickness and for iron oxides[85,86] on Pt(111) have been reported. There are, however, only few studies[87,88] which address the Fe ultrathin film growth on Pt(111) surfaces and no studies exist for the growth on surfaces vicinal to Pt(111), for instance Pt(997), and its conditions for the surface alloy formation. It is essential to know the growth conditions of ultrathin Fe films on the vicinal Pt surface in order to understand the influence of structure and morphology on the magnetic properties of the ferromagnet[89,90] and coupling to the substrate atoms.

At room temperature, bulk Fe and Pt have bcc (α phase, the space group $Im\bar{3}m$) and fcc (the space group $Fm\bar{3}m$) crystal structures with lattice parameters 2.87 Å and 3.92 Å, respectively[91,93] . For the pressure of 1 atm (1013 mbar), three allotropic Fe phases exist depending on temperature as indicated in the Fe-Pt phase diagram of Fig.2.6[92] : bcc α-phase for 0 K$< T <$1185 K, fcc γ-phase for 1185 K$< T <$1667 K, and bcc δ-phase for 1667 K$< T <$1811 K. Fig.2.6 shows that there exist four equilibrium phases for $Fe_{1-x}Pt_x$ alloy depending on the chemical composition and temperature range. The crystal structures of those phases are summarized in Fig.2.7. At relatively high temperature ($T \sim$1000 °C in Fig.2.6), the equilibrium phase of the alloy is the
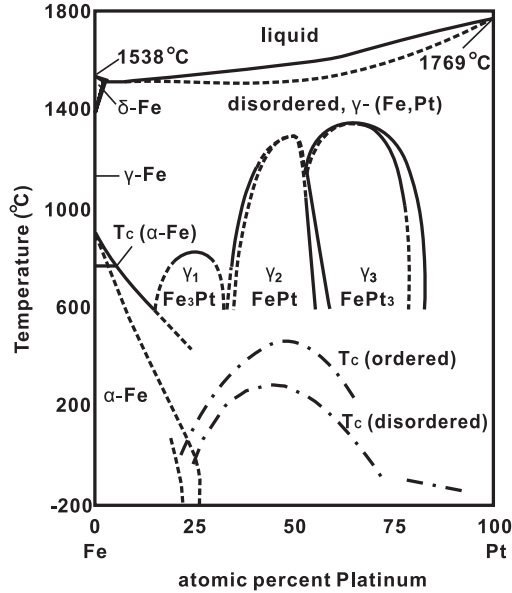
Figure 2.6 Fe-Pt bulk phase diagram[91, 92] . Fully determined structural phase transformations are indicated as solid line. Dotted lines indicate structural phase transformations whose understanding is not complete yet. Curie temperatures (T_c) are indicated as dash-dot lines.
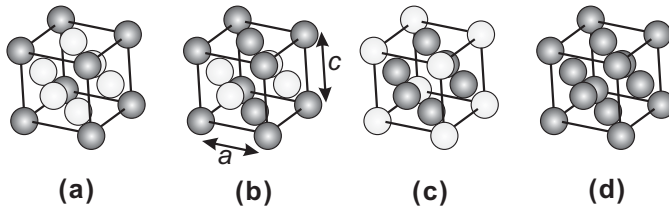
Figure 2.7 Crystal structure of the ordered $Fe_{1-x}Pt_x$ alloy and Pt at room temperature. (a) The simple cubic γ_1-Fe_3Pt phase with $x=0.25$ which has lattice parameter $a=3.73$ Å, (b) the tetragonal γ_2-FePt phase with $x=0.5$, $a=3.82$ Å and $c=3.71$ Å, (c) the simple cubic γ_3-$FePt_3$ phase with $x=0.75$ and $a=3.87$ Å, (d) the fcc Pt with $a=3.92$ Å. Black and white circles indicate preferred atomic sites for Pt and Fe occupation, respectively.

γ-phase for the whole composition range. The crystal structure is described by the space group $Fm\bar{3}m$: Fe and Pt atoms are randomly located at the fcc lattice (chemically disordered) . The lattice parameter increases linearly as Pt content increases[94] . At relatively low temperature (T <1000 °C in Fig.2.6), the alloy shows three ordered phases depending on the composition x as in Fig.2.7: the simple cubic γ_1-Fe$_3$Pt (space group $Pm\bar{3}m$) for $0.16 < x < 0.33$; the tetragonal γ_2-FePt (space group $P4/mmm$) for $0.35 < x < 0.55$; the simple cubic γ_3-FePt$_3$ (space group $Pm\bar{3}m$) for $0.57 < x < 0.79$. As shown in Fig.2.7 (a) and (c), the γ_1 and γ_3 phases have the same simple cubic crystal lattice symmetry with different lattice parameter[95] . For the γ_1-phase, 8-Pt atoms are located at each corner of the simple cubic lattice, and each face is occupied by an Fe atom. The crystal structure of the γ_3-phase can be described equivalently. Because of the same lattice symmetry, these two phases are usually referred to as $L1_2$ phase from their Strukturbericht designations[96] . The γ_1 phase is tetragonal with the lattice parameter $a > c$ and usually referred to as $L1_0$ phase[97] : Fe and Pt atoms are alternatingly stacked in the (001) basal planes.

From the bulk diagram in Fig.2.6 and calculations of the surface behavior[98] , it can be expected that Fe and Pt atoms favor mixing and form ordered alloys in the entire composition range. When the thermal energy is not high enough to overcome the activation barrier of mixing, pure Fe layers grow on the Pt surface. Several STM studies[88,99] show that Fe deposited in this temperature range exhibits 3D island growth on Pt(111).

However, this thermodynamic preference can be avoided kinetically for the growth of Fe layer on the vicinal Pt(997) surface with a regular array of steps and terraces; Under certain experimental conditions, the diffusion length of adatoms can be larger than the terrace length. In this case, adatoms continuously flow to the steps and adsorption starts preferentially from the lower step-edges. This growth is typically referred to as step-flow growth which results in a smooth adlayer structure.

The aim of this section is to find the conditions for step-flow growth of Fe layers on Pt(997) to form smooth 1D and 2D Fe nanostructures in the coverage range 0 ML $\sim$ 2 ML. TEAS was mainly used for the study because the information of TEAS is exclusive from the surface and thus well suited for the investigation of the adlayer growth at such low coverage on a single crystal surface. The investigation covers a wide temperature range from 200 K to 800 K. Within this range the transition from Fe epitaxial growth to surface alloying and further on to bulk alloying is observed. This section is organized as follows: The results at the low temperature and the medium/high temperature range will be presented in Sec.2.2.2 and Sec.2.2.3 respectively. Sec.2.2.3 involves different aspects of Pt-Fe alloying. The section is summarized in Sec. 2.2.4.

2.2.2 Epitaxial growth of Fe on Pt(997)

TEAS experiments are carried out with the experimental set-up shown in Sec.2.1.2. The grazing and non-grazing incident geometries as described in Sec.2.1.2 were used. Fe is evaporated from a 99.99% purity Fe-rod.

Fig.2.8(a) shows the reflected He diffraction intensity in grazing scattering geometry measured *in situ* during Fe deposition in the substrate temperature range 175 K $\leq T \leq$ 800 K. Because this scattering geometry is extremely sensitive to the step-edges, the maxima in the intensity at $\theta_{Fe} \sim 0.13$ ML can be attributed to the formation of complete monatomic rows at each step edge similarly as for other adsorbates[52] . These maxima are observed for low temperatures (175 K) and are still observable up to 500 K. The

(a)   (b)
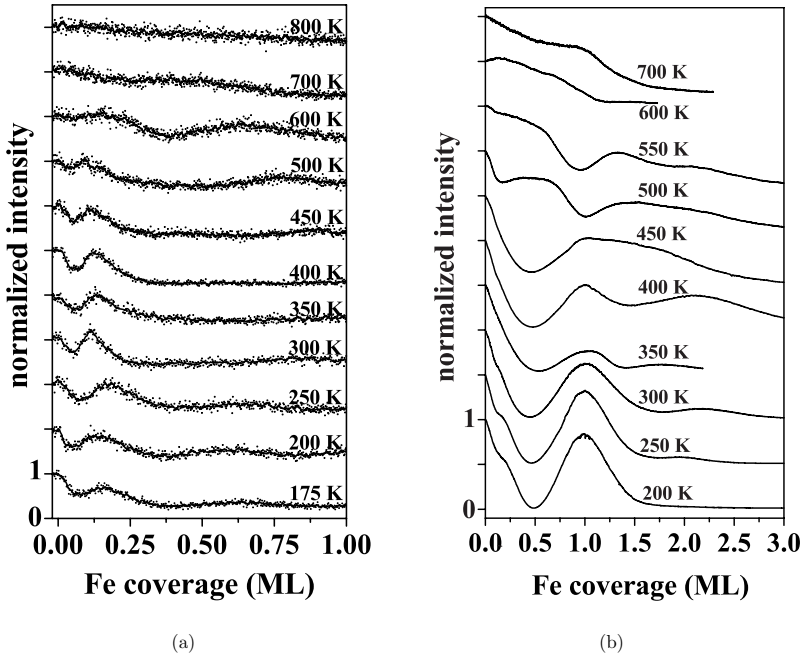
Figure 2.8 He reflected intensity normalized to the intensity of the clean surface measured *in situ* during Fe deposition. (a) grazing scattering geometry, $\theta_i = 85$ °, $\chi = 170$ °. (b) non-grazing geometry, $\theta_i = 57.8$ °, $\chi = 101.8$ °. The substrate temperatures are indicated at each curve. For clarity the curves above the lowest one are shifted upward by multiples of +1 unit in (a) and by multiples of 0.5 units in (b).

coverage at the maximum of the first peak deviates, however, from the nominal value of 0.13 ML at the lowest temperatures, which can be explained by the activation threshold for corner rounding as reported earlier for the cases of Co, Cu, and Ag on Pt(997)[53] . Below 250 K, the diffusion barrier between a Fe atom site in the second Fe row at the step edge and a site at the uncovered Pt step edge is higher than the thermal energy.

Fig.2.8(b) shows the He diffraction intensity in non-grazing scattering geometry. In this geometry information on the processes on the terraces is obtained. We first focus on the range between 200 K and 450 K: A very prominent intensity maximum appears which indicates the formation of a complete monolayer before adsorption in the next layers begins. We use this maximum occurring at low temperature for a consistent coverage and evaporation rate calibration of our study. The shoulder at $\theta_{Fe} \sim 0.2$ ML coverage is again a signature of the row formation discussed above. However, in contrast to the data from Fig.2.8(a) it can not be interpreted in a straightforward manner as this feature disappears between $T = 300$ K and $T = 450$ K while Fig.2.8(a) indicates that the formation of a monatomic row persists all the way to 500 K. At 400 K a second intensity maximum near 2 ML coverage is observed which suggests that the layer-by-layer growth continues beyond 1 ML coverage. Maxima for the completion of further layers were not observed, except under conditions when the residual gas pressure was unusually high (probably a surfactant induced behavior which was not studied in detail).

The growth mode derived from these results is corroborated by the measurements shown in Fig.2.9 and Fig.2.10. The diffraction patterns in Fig.2.9 are measured after deposition of the indicated Fe coverage on clean Pt(997) at 350 K. The broken lines indicate peak positions which correspond to the diffraction orders between $n = -4$ and $n = -2$. Up to a coverage of 0.71 ML the diffraction peaks of a clean Pt(997) surface are preserved although their intensity decreases with increasing coverage. At a coverage of 1.5 ML the diffraction pattern disappears almost completely and the remaining intensity of a small facetted sample region dominates the pattern. Thus, Fe deposition reduces the reflectivity substantially and after ML completion the original Pt(997) periodicity of the topmost layer to which He scattering is exclusively sensitive is lost. This indicates a substantial roughening of the surface on an atomic scale without any defined periodicity.

Fig.2.10 shows diffraction patterns after annealing of the 1.5 ML Fe layer whose diffraction pattern is shown in Fig.2.9 (d): After deposition of 1.5 ML of Fe at $T = 350$ K (Fig.2.10(a)), the sample was heated to the temperatures 400 K (Fig.2.10(b)) and 450 K (Fig.2.10(c)). It is shown that annealing above 400 K results in a re-appearance of the narrow $n = -3$ diffraction peak of the ordered Pt(997) morphology. The result
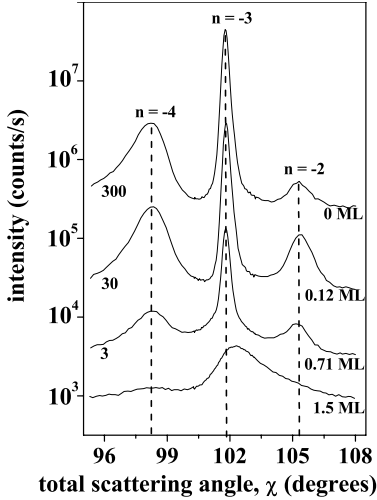
Figure 2.9 TEAS diffraction patterns with $\theta_i = 57.8$ ° after deposition of the indicated Fe coverage at $T = 350$ K. For clarity all curves but the lowest one have been shifted upward by multiplying with the factors indicated on the left hand side.
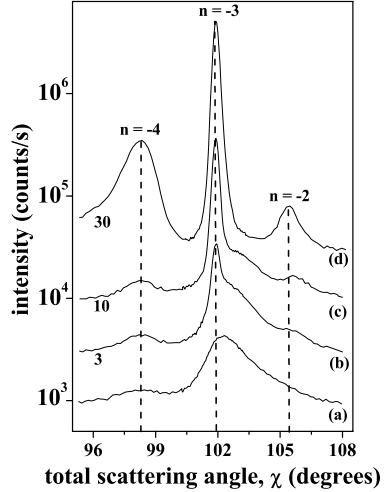
Figure 2.10 TEAS diffraction patterns for $\theta_i = 57.8°$ recorded (a) after deposition of 1.5 ML Fe at 350 K and during the following annealing at (b) 400 K, and (c) 450 K. For comparison (d) shows a spectrum of the clean Pt(997) surface. For clarity the curves are shifted upward by the indicated factors, as in Fig.2.9.

demonstrates that the defect-rich structure formed at a deposition temperature of 350 K orders at 400 K due to the on-set of mass transport. This corresponds exactly to the temperature where a reflectivity maximum at $\theta_{Fe} \sim 2.0$ ML is observed (see Fig.2.8(b)). The growth at low temperature can thus be identified with a Stranski- Krastanov (SK) like growth mode, which around 400 K tends towards a layer-by-layer growth mode. In the case of the vicinal Pt(997) surface this behavior is, however, induced rather by kinetics than by free surface and strain energies which are the important parameters in regular SK growth. A significant change in the terrace diffusion barrier of Fe between the clean Pt(997) surface and the surface covered by Fe might, for example, explain the observation. It would lead to a reduction of step decoration in the second Fe layer in favor of island nucleation on the terraces.

Above 450 K the He reflectivity curves in Fig.2.8(b) completely change their character. The maximum at monolayer coverage is replaced by a minimum. Above 600 K, finally, the amplitude of the oscillations is strongly reduced and a continuous He intensity decrease becomes dominant. These changes are due to surface-restricted alloying between 450 K and 550 K and due to bulk alloying above 600 K and will be discussed in Sec.2.2.3.

2.2.3 Surface alloying of Fe with Pt

Fe and Pt exhibit a strong tendency for alloy formation and Fe exhibits antisegregation on Pt surfaces (segregation energy Fe/Pt: +0.63 eV/atom; surface mixing energy +0.76 eV/atom[98]) . Fe deposited on Pt(997) diffuses into the bulk on a timescale of minutes at temperatures $T \geq 600$ K. This is demonstrated in Fig.2.11 in which the Fe concentration is plotted as a function of annealing temperature for 1 ML of Fe initially deposited at 200 K. The concentration is obtained from Auger spectra ranging from 20 eV to 770 eV recorded for a primary electron energy of 3 keV. After deposition of 1 ML Fe at $T = 200$ K, the temperature is increased in 50 K steps to $T = 850$ K. AES measurements are carried out after each temperature step. The total dwell time at each temperature is 15 minutes, the time to establish the next higher temperature before a measurement is started is > 5 minutes. The relative amount of Fe near the surface can be obtained by[100]

$$C_{Fe} = \frac{I_{Fe}}{S_{Fe}} / \left(\sum_{\alpha=Fe,Pt} \frac{I_\alpha}{S_\alpha} \right) \tag{2.6}$$

where I_α is the peak to peak intensity corresponding to a specific Auger line of the element α (α = Fe, Pt), and S_α is the relative sensitivity factor of the elements, namely $S_{Pt} = 0.025$ and $S_{Fe} = 0.20$[100] . For the data displayed in Fig.2.11 the MNN peak at $E = 64$ eV was used for Pt and the LMM peak at $E = 651$ eV for Fe. The relative amount
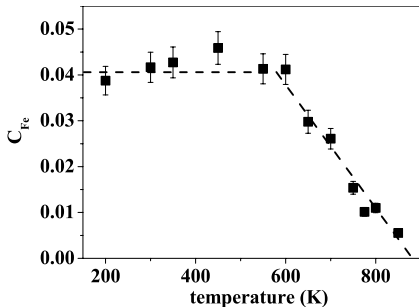

Figure 2.11 Relative amount of Fe monitored by AES and evaluated from Eq.(2.6) while ramping the sample temperature in steps of 50 K or 100 K. The dashed line is a guide to the eye.

of Fe within the information depth of AES is constant within experimental accuracy for $T \leq 600$ K, then starts to decrease and becomes undetectable above 850 K. We assign the onset of the decrease at 600 K to the beginning of Fe diffusion into the Pt bulk.

Bulk alloying thus explains the continuous decrease of the He intensity in Fig.2.8(b) above 600 K. But it does not account for the shape of the reflectivity curves at 500 K and 550 K. While diffusion into the Pt bulk is still kinetically hindered below 600 K there still is, however, the strong driving force for Fe to intermix with Pt[98] . This can drive an alloying process within the surface layer because the energy barrier to alloying at the surface is lower than for diffusion into the bulk. Alloying may *e.g.* proceed with a lowered activation barrier through Fe-Pt exchange at the step edges followed by diffusion within the terrace. Thus the initially slowly decreasing He intensity in the He reflectivity curves at 500 K and 550 K is ascribed to the observation of surface restricted alloying. Clearly, the alloying process is not accompanied by He intensity oscillations. The oscillations observed at 500 K and 550 K set in only at a coverage above 0.5 ML and we find a minimum at a total Fe coverage of 1 ML and a maximum around 1.5 ML which corresponds to a shift by $+ 0.5$ ML with respect to the oscillations observed below 500 K. This observation strongly suggests that the alloy formation is completed at a Fe coverage of 0.5 ML. When deposition continues beyond 0.5 ML a new Fe monolayer starts to grow on top of the alloy monolayer and leads to the observed oscillations. An alloy formed by a Fe coverage of 0.5 ML corresponds nominally to a $Fe_{50}Pt_{50}$ alloy. In fact, the alloy with this stoichiometry is known to be a reproducibly formed alloy on Pt(111) which orders in alternating rows of Pt and Fe[101] .

As a special case we want to discuss the Fe deposition at 500 K in Fig.2.10 in more detail. At that temperature we first find a steep decrease of He reflectivity then a minimum close to 0.13 ML followed by an increase until 0.5 ML. Obviously, the slope at coverages below 0.13 ML corresponds to the low temperature behavior, for which no significant surface alloying occurs. At completion of the first Fe row at the step edge (1 row = 1/8 ML) there is thus no indication of alloying yet. Only during continued deposition the data start to approach the 550 K curve. Although the peak at 0.13 ML in Fig.2.8(a) which indicates step decoration is primarily due to the step edge morphology it is thus likely that the first row which decorates the step edge is formed mostly by Fe (as indicated in Fig.2.12(a)) which during continued deposition dissolves into the Pt terrace (Fig.2.12(b)).

We now focus on the fact, that for evaporation at $T \leq 400$ K an extremely low He intensity is observed at 0.5 ML Fe coverage (Fig.2.8(b)). This minimum cannot be ascribed to a highly disordered layer which re-orders when ML coverage is approached.

(a)   (b)   (c)
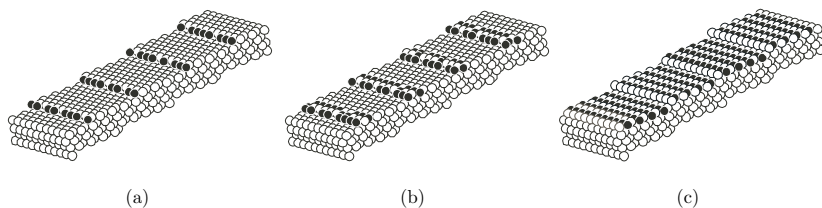
Figure 2.12 Schematic diagram illustrating diffusion of Fe to the upper terrace of Pt(997) surface to form $L1_0$ FePt surface alloy at the temperature between 450 and 550 K. White and black circles indicate Pt and Fe atoms respectively. (a) Formation of atomic row at each step edge at $\theta_{Fe} = 1/8$ ML, followed by sub-surface diffusion (b) at $\theta_{Fe} = 2/8$ ML. (c) Idealized $Fe_{50}Pt_{50}(111)$ surface alloy.

It is well known from similar cases that destructive interference between atoms scattered from regions covered by different elements plays an essential role[63] . The fact that this minimum disappears for $T \geq 550$ K confirms the presence of a transition from separated Pt and Fe regions to a homogenously mixed, *i.e.* alloyed, surface structure.

It is suggested that the surface alloy which we observe for Fe/Pt(997) exhibits a structure similar to the ideal (111) plane of the bulk $L1_0$ $Pt_{50}Fe_{50}$ alloy[101] as depicted in Fig.2.12(c). It is noticed that for the actual surface of a bulk alloy, namely $Pt_{80}Fe_{20}(111)$, substantial depletion of Fe in the top layers was found for temperatures above 700 K[102, 103] . In contrast, Fe deposited on Pt(111) at room temperature followed by annealing between 600 K and 850 K is known to form an ordered surface alloy within the top-most layer containing almost 50 % of Fe[87] . We could not obtain direct information on the chemical order of the surface alloy from the employed methods in the case of the vicinal surface. Neither He diffraction nor low energy electron diffraction (LEED) exhibit superstructure peaks corresponding to a doubled surface unit cell size. This can, however, be expected if there is only local chemical order which does not even extend to the nm range. In fact, already for the FePt alloy on Pt(111) annealed at much higher temperature no perfect nm-range ordering of the Fe rows was observed[101, 104].

As a next point we will discuss the alloying kinetics. The surface morphology observed in Fig.2.9 at temperatures below 500 K which we attribute to the growth of a mostly pure Fe monolayer does not correspond to equilibrium morphology. We demonstrate this by interrupting the deposition at various coverages below 0.2 ML, *i.e.* in the linearly decreasing part of the reflectivity curve (Fig.2.13): When deposition is stopped at the coverages (a) 0.06 ML, (b) 0.13 ML, and (c) 0.19 ML the curves switch from a negative to a positive slope, indicating recovery of He reflectivity. The solid lines in
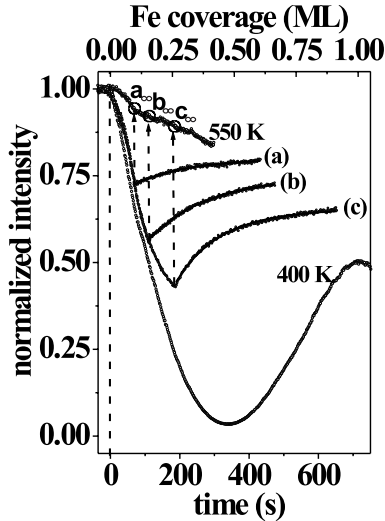
Figure 2.13 Deposition of Fe (coverage scale, above) and recovery of reflected He intensity (time scale, below). In the curves (a)-(c) Fe is deposited at 475 K at a deposition rate of 0.0014 ML/s. For comparison we show the continuous deposition curves at 400 K and at 550 K taken from Fig.2.8(b).

the curves (a) to (c) in Fig.2.13 are exponential fits. When we monitor the following increase of the He reflectivity signal as a function of time, we can study the alloying kinetics. We find a transition from long recovery times (> 300 s, *i.e.* much longer than deposition time of one atomic row) at 450 K to short recovery times (≤ 100 s *i.e.* shorter than deposition time for one row) at 500 K: Below 400 K the alloying is kinetically forbidden and at 550 K alloy formation occurs in equilibrium with evaporation. Within experimental precision the time constant is independent of Fe coverage. Fig.2.13 shows the decrease of He reflectivity for Fe deposition and the following He intensity recovery after deposition is stopped at (a) 0.06 ML, (b) 0.13 ML, and (c) 0.19 ML at an intermediate surface temperature of 475 K. The recovery time is determined by fitting a single exponential to the measured data. For the 475 K data in Fig.2.13 this yields a recovery time of 150 ± 20 s. The substantial change of recovery time constant between 450 and 500 K suggests a significant activation energy. Using an Arrhenius model we estimate an effective activation energy of 0.7 ± 0.3 eV. This barrier can reflect either the Pt-Fe exchange barrier or the diffusion barrier of Fe atoms (or the accompanying vacancies) inside the terraces.

Fig.2.13 contains also the continuous Fe deposition curves at 400 K and 550 K taken from Fig.2.8(b) for comparison with the deposition and recovery curves (a)-(c). The initial Fe deposition in the curves (a)-(c) closely follows the 400 K temperature behavior. Upon stopping Fe deposition the relaxation towards equilibrium morphology becomes

evident by the increase in intensity. The data show that the recovery will not lead to He intensities higher than the one observed on the 550 K curve at the same Fe coverage. The latter are marked as a_∞, b_∞, and c_∞ in Fig.2.13. This observation strongly suggests that at 550 K adsorption takes place close to equilibrium and the alloying process can be considered to be instantaneous on the time scale of Fe deposition. In contrast, the adsorption curves recorded between 400 and 550 K are determined by the interplay of Fe deposition rate and alloying kinetics which occur on the same time scale.

Finally, we want to compare the results presented in this paper to a study of Fe deposited on the low index Pt(111) by Jerdev *et al.*[87]. That study focusses on chemical surface composition for coverages between 1 ML and 2 ML analyzed by low energy ion scattering, X-ray electron spectroscopy, and LEED. Although both, the study by Jerdev *et al.* and ours, find a similar sequence of surface structures there are characteristic differences. Jerdev *et al.*[87] find surface alloying at a much higher temperature window (600 K - 850 K). Their temperature ramps are run on a much faster time scale (10 s dwell time) compared to our experiments (typical dwell times of > 5 minutes). In addition, they deposit a given coverage and then anneal the sample while in the He intensity data Fe is deposited at the observation temperature. Qualitatively, these differences explain why the onset temperatures we obtain may be somewhat lower. The major difference of the studies is, however, the regular step array in our study which may activate a different path for alloying than on the Pt(111) surface. As already discussed above, the uniform terrace width of 2 nm provides a high density of high coordination sites for adsorbing atoms already at low coverage. The residence time of atoms on the terraces is reduced and their attachment to substrate steps is forced. The lowering of the observed alloying temperature thus suggests a more efficient alloying process for Fe at the Pt step edge with respect to Fe on terrace sites or at the edges of Fe islands.

Jerdev *et al.* suggest that some exchange of Fe and Pt occurs already at 350 K. As He scattering is mostly sensitive to surface morphology and provides chemical sensitivity only through the surface corrugation amplitude we cannot exclude that a small percentage of the adsorbates exchange with the substrate. Our results suggest, however, that this does not reflect the behavior of a significant amount of the Fe coverage. In fact, in an earlier, unpublished STM study[99] Fe incorporation into Pt(111) on the percent level was found even below 140 K.

In their study Jerdev *et al.* find the formation of an $Fe_{45}Pt_{55}$ alloy and report that on top of the alloy an Fe layer forms, which does not incorporate significant amounts of Pt. This is in good agreement with our observation of growth oscillations in the corresponding temperature range for surface alloy formation.

2.2.4 Conclusions

The Fe growth on the vicinal Pt(997) surface was *in situ* investigated by TEAS. The results are summarized graphically in Fig.2.14. Step decoration and the formation of a Fe monolayer is found between 200 K and 450 K. A surface restricted alloy forms for deposition between 450 and 550 K and bulk alloying occurs for $T \geq 600$ K which is corroborated by Auger electron spectroscopy results. Comparison to the growth of Fe on Pt(111) demonstrates that a lower step density tends to favor a rough film morphology whereas on the vicinal surface employed in this study a flat monolayer can be formed and three-dimensional growth can be suppressed at least up to monolayer coverage. Surface alloy formation appears on both surfaces but sets in at significantly lower temperature on the vicinal surface.

This study allows to derive three specific recipes to prepare nanostructures: (1) Perfect decoration of the step edges of Pt(997) by monatomic Fe chains occurs between 250 and 500 K. (2) The best order of a Fe ML as judged from the He reflectivity is obtained around $T=350$ K. (3) The FePt alloy remains restricted to the surface layer if Fe is evaporated in the range 500 K to 550 K. The surface alloy is supposed to consist of a few atoms long Fe chains embedded in the Pt layer.
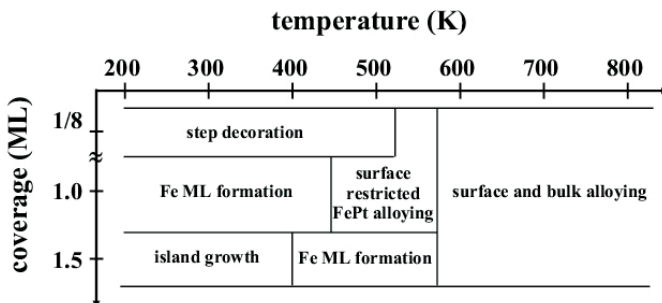

Figure 2.14 Parameter ranges for the different growth modes of Fe/Pt(997) for a deposition rate around 10^{-3} ML/s.

2.3   Growth of Fe on Pt(111)

For comparison with the growth of Fe on the vicinal Pt(997) surface in Sec.2.2 and a detailed discussion of the origin of magnetic properties of Fe on Pt(111) in Chap.3, it is important to discuss the growth of Fe on Pt(111). As it is found that no complete study of this system is available in the literature a separate study by LEED was carried out. It will be presented in this section. A clean and well ordered Pt(111) surface was prepared by repeated cycles of Ar^+ sputtering and annealing at $T = 900$ K. Under UHV conditions as used in Sec.2.2, Fe ultrathin films of less than 2 ML coverage were evaporated on Pt(111) at $T = 300$ K. The thickness was calibrated by a quartz crystal thickness monitor (Inficon XMT/2). Cleanliness, contamination, and the amount of Fe deposit on the surface were controlled by Auger electron spectroscopy (AES). Structural information of the films was obtained from LEED patterns. A sample temperature of 85 K was used in order to reduce the Debye-Waller effect. The results are compared with kinematic calculations using the code SARCH[105] .

2.3.1   3D island growth of bcc-Fe

Fig.2.15 shows the comparison of the LEED patterns of Pt(111) surfaces with and without an Fe layer measured with the primary electron energy E=152 eV. A clear 3-fold* (1×1) pattern from the clean and well ordered Pt(111) surface is shown in

<div align="center">(a)   (b)   (c)</div>
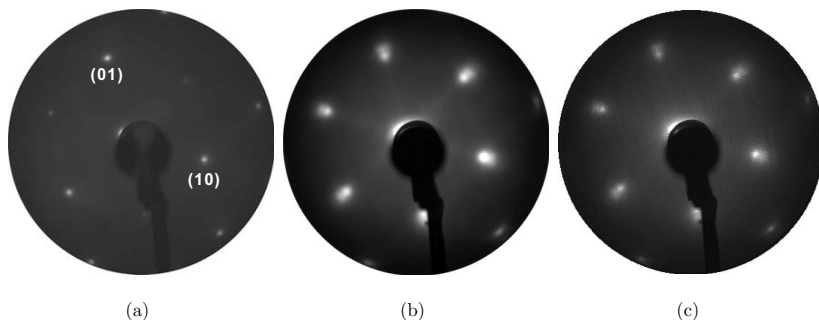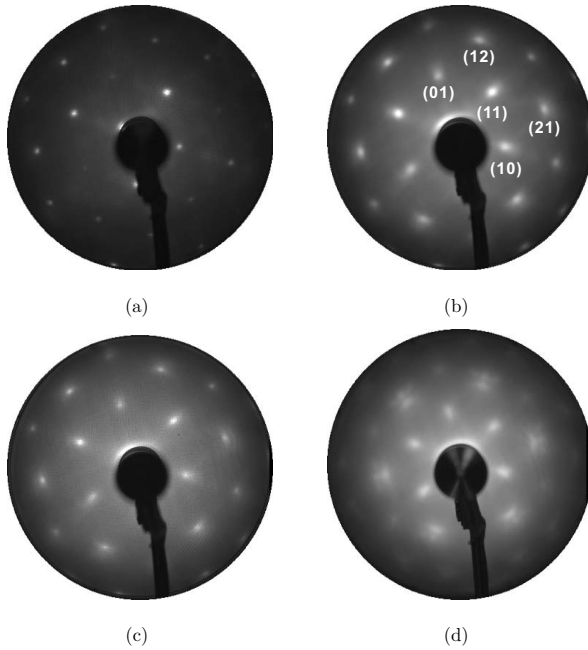
Figure 2.15 LEED patterns of (a) clean Pt(111), (b) 0.8 ML of Fe and (c) 1.5 ML of Fe on Pt(111) measured at E=152 eV. Fe was deposited at room temperature. The indices for the basis vectors of the reciprocal lattice of Pt(111) is given in (a).

---

*Note that the fcc(111) surface has 3-fold symmetry from the cubic symmetry, not 6-fold symmetry.

Fig.2.15 (a). In Fig.2.15 (b) and (c) satellite spots are visible which exhibit a radial displacement with respect to the substrate diffraction spots. If the Fe adlayer had the same lattice constant of the Pt substrate, no satellite spots would appear. Fe thus doesn't exhibit pseudomorphic growth on Pt(111) even at low coverage.

Fig.2.16 shows LEED patterns of the samples in Fig.2.15, however, obtained at different electron energy $E=323$ eV. In comparison to the (1×1) pattern of clean Pt(111) in Fig.2.16(a), patterns of 0.8 and 1.5 ML Fe on Pt(111) in Fig.2.16(b) and (c) clearly show that (21), $(1\bar{1})$, $(\bar{1}2)$, $(\bar{2}\bar{1})$, $(\bar{1}1)$, and (12) spots are tangentially elongated whereas (10), (01), (11), $(\bar{1}0)$, and $(\bar{1}\bar{1})$ spots are radially elongated. When the coverage is 2.0 ML, more complicated patterns are observed with satellite spots clearly separated from the (1×1) spots (Fig.2.16(d)).

Such complicated patterns cannot be explained by a trigonal lattice such as fcc(111) or hcp(0001). When the substrate is fcc(111) and the overlayer is bcc in its bulk state,

(a)   (b)

(c)   (d)

Figure 2.16 LEED patterns of (a) clean Pt(111), (b) 0.8 ML, (c) 1.5 ML and (d) 3.0 ML of Fe on Pt(111) measured at $E=323$ eV. Fe was deposited at room temperature. The indices of the Pt(111) diffraction spots are given in (b).

(a)   (b)
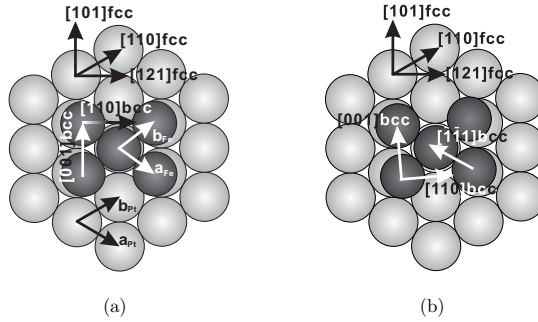
Figure 2.17 Model used for the kinematic calculation of the LEED patterns of an Fe layer on Pt(111) with (a) the Nishiyama-Wassermann[106, 107] and (b) the Kurdjumov-Sachs[108] orientations. Small black circles indicate Fe atoms in the overlayer. Large gray circles indicate Pt atoms in the substrate layer.

it is well known that the overlayer can have a bcc(110) symmetry with Nishiyama-Wassermann[106, 107] or Kurdjumov-Sachs[108] orientation. These orientations in the case of Fe-Pt(111) can be described by fcc Pt and Fe bulk lattice constants of c_{Pt} =3.92 Å and c_{Fe} =2.86 Å[91, 93] which correspond to nearest neighbor distances of 2.77 Å and 2.48 Å, respectively:

(1) bcc (110) Fe layer with Nishiyama-Wassermann orientation: the $\langle 110 \rangle^{\dagger}$ direction in the bcc overlayer is parallel to the the $\langle 121 \rangle$ direction in the fcc substrate-layer as in Fig.2.17(a). The relation of the lattice parameters between Fe overlayer and Pt substrate can be described as

$$\begin{pmatrix} a_{Fe} \\ b_{Fe} \end{pmatrix} = \begin{pmatrix} 0.94 & -0.09 \\ -0.09 & 0.94 \end{pmatrix} \begin{pmatrix} a_{Pt} \\ b_{Pt} \end{pmatrix} \tag{2.7}$$

where (a_{Fe}, b_{Fe}) and (a_{Pt}, b_{Pt}) indicate the basis of the unitcell of the Fe and Pt layer respectively.

(2) bcc (110) Fe layer with Kurdjumov-Sachs orientation: the $\langle 111 \rangle$ direction in the bcc overlayer is parallel to the $\langle 110 \rangle$ direction of the fcc substrate-layer as in Fig.2.17(b).

---

† Note that $\langle uvw \rangle$ indicates classes of crystallographic directions: For the cubic lattice, $\langle 110 \rangle$ denotes *e.g.* all equivalent directions [110], [1$\bar{1}$0], [$\bar{1}$10], [$\bar{1}\bar{1}$0], [101], [10$\bar{1}$], [$\bar{1}$01], [$\bar{1}$0$\bar{1}$], [011], [01$\bar{1}$], [0$\bar{1}$1], and [0$\bar{1}\bar{1}$]

The matrix description is given as

$$\begin{pmatrix} a_{Fe} \\ b_{Fe} \end{pmatrix} = \begin{pmatrix} 0.89 & 0 \\ -0.19 & 0.97 \end{pmatrix} \begin{pmatrix} a_{Pt} \\ b_{Pt} \end{pmatrix} \qquad (2.8)$$

Three equivalent crystallographic domains can exist for the case of Nishiyama-Wassermann orientation considering the relation Eq.(2.7) and Fig.2.17(a). For the case of Kurdjumov-Sachs orientation, there exist six equivalent crystallographic domains from the relation Eq.(2.8) and Fig.2.17(b). Three different domain orientations are due to the 3-fold substrate symmetry. This number is multiplied by two due to three mirror planes in the surface which are no mirror planes of the adlayer structure. These crystallographic domains are reflected in the appearance of six satellite spots around the substrate peaks.

Kinematic calculations of LEED patterns were carried out for these structures with the computer code SARCH[105] . It is assumed that covalent radii of Pt and Fe are $r_{Pt} = 1.39$ Å and $r_{Fe} = 1.24$ Å[109] , respectively. The mean free path of the incident electrons is assumed to be 8 Å. Fig.2.18 shows kinematically calculated LEED patterns of the two models in Fig.2.17, with normal incidence of electron beam with energy E = 87 eV.

The pattern of the Nishiyama-Wassermann orientation in Fig.2.18 (a) shows triple satellite spots around the (10), (01), (11), $etc.$ spots. Around the (21), (12), $etc.$ spots,

(a)   (b)
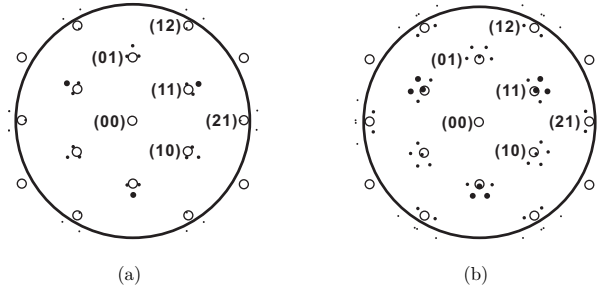
Figure 2.18 Kinematic calculation of the LEED patterns of Fe on Pt(111) for (a) the Nishiyama-Wassermann orientation, (b) the Kurdjumov-Sachs orientation. Open circles with indices represent the Pt(111) substrate spots. Filled circles or dots indicate peaks from the Fe overlayer. Note that the size of these circles indicates their multiplicity. The black circle surrounding each pattern indicates the diameter of the Ewald sphere for an electron beam energy of 87 eV.

however, no satellite spots appear in the Ewald sphere. For the case of the pattern of the Kurdjumov-Sachs orientation, Fig.2.18 (b) shows five satellite spots around the (10), (01), (11), *etc.* spots. Note, that one of the spots is close to the substrate spot. Six satellite spots appear around the (21), (12) *etc.* substrate peaks.

It is found that the pattern of the Kurdjumov-Sachs orientation in Fig.2.18 (b), rather than that of the Nishiyama-Wassermann orientation in Fig.2.18 (a), reflects the observed LEED patterns. It is difficult to confirm one of the structures in detail because the observed satellite spots are not sharp, probably due to small domain sizes or due to the occurrence of a wide variety of similar structures. However, the pattern allows to exclude the Nishiyama-Wassermann orientation as it cannot reproduce the tangential elongation of the (21), (12) etc. spots. In addition, the arrangement of exactly these satellites is, in fact, in good agreement with the pattern calculated for the Kurdjumov-Sachs orientation.

Therefore, it is suggested that the observed patterns in Fig.2.15 and 2.16 correspond to the bcc-Fe layer on Pt(111) with Kurdjumov-Sachs orientation. The six-fold satellite patterns indicate equal probability of the appearance of the six equivalent crystallographic domains. STM measurements show the 3D island growth of Fe layer on Pt(111)[88,99] . Fig.2.19[99] presents images from a detailed STM study by Rusponi *et al.*[99] which focusses on the surface morphology of Fe on Pt(111) as a function of coverage for room temperature Fe deposition. The island height assumes integer multiples of the Fe layer heights and no indication for the growth via double layer
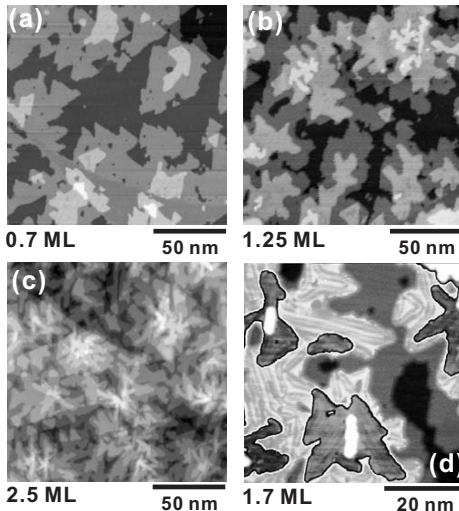

Figure 2.19 STM images of Fe/Pt(111) growth at 300 K, from Rusponi *et al.*[99] . Fe coverages: (a) 0.7 ML, (b) 1.3 ML, and (c) 2.5 ML. (d) shows a contrast enhanced image at 0.7 ML which evidences the dislocation lines in the Fe adlayer.

formation is found. By enhancing the contrast in the STM images (Fig.2.19 (d)) one obtains clear evidence for the existence of dislocation lines especially in the second Fe layer. This suggests that the Fe adlayer lattice is not commensurate with the substrate lattice and pseudomorphic growth does not occur, in agreement with the results from the discussion of the LEED patterns above.

2.3.2 Surface alloying of Fe on Pt(111)

To compare with the results of the surface alloy of Fe on Pt(997), the condition for the formation of an Fe-Pt surface alloy on Pt(111) is investigated by post annealing for approximately 10 **min.** after Fe deposition. Fig.2.20 shows LEED patterns before and after annealing of 0.8 ML Fe deposited at room temperature on Pt(111). In contrast to the pattern in Fig.2.20 (a) taken before annealing, annealing at T=500 and 600 K re-

(a)   (b)

(c)   (d)
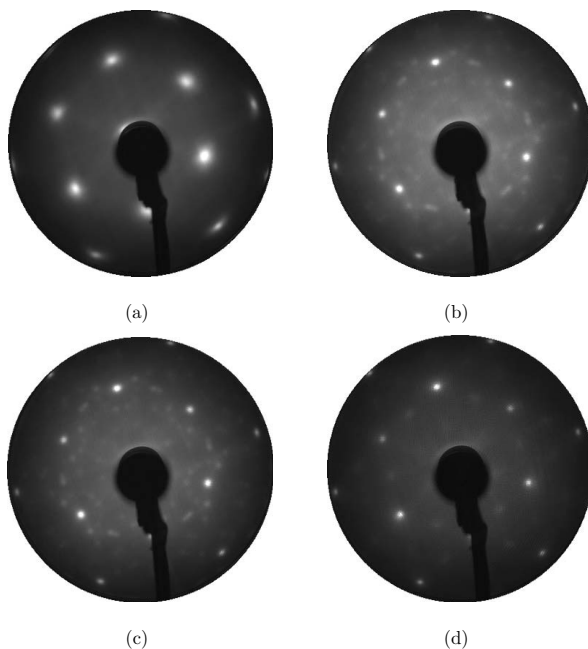
Figure 2.20 LEED patterns of 0.8 ML of Fe on Pt(111) (a) before annealing and after annealing to (b) T = 500 K, (c) T = 600 K, and (d) T = 700 K. The energy of the electron beam was E = 169 eV.

sults in complicated superstructure as can be seen in Fig.2.20 (b) and (c). Interestingly, this complicated pattern disappears after annealing at $T = 700$ K, and a weak (2×2) superstructure appears as shown in Fig.2.20 (d), in good agreement with the results by Jerdev *et al*[87] : It was reported that annealing of 0.8 ML Fe on Pt(111) above 750 K results in a (2×2) LEED pattern which indicates the formation of the ordered surface alloy. A STM measurement[104] shows in fact that this annealing condition results in the formation of a $Fe_{50}Pt_{50}$ surface alloy. Therefore, it is concluded that the (2×2) LEED pattern in Fig.2.20 (d) corresponds to the formation of the $Fe_{50}Pt_{50}$ surface alloy and that the complicated LEED patterns in Fig.2.20 (b) and (c) corresponds to the probably pure and unmixed Fe layer, which is however different from the bcc-Fe layer before annealing.

The incommensurate surface structures of Kurdjumov-Sachs domains, which occur before surface alloying, are relaxed to a higher order commensurate phase. A supercell which fits well with respect to the observed LEED pattern is the $(\sqrt{13} \times \sqrt{13})$ R13.9° structure which requires short-range short-range displacement of Fe atoms. The $(\sqrt{13} \times \sqrt{13})$ reconstructed Fe layer on Pt(111) can be described by a matrix equation as following:

$$\begin{pmatrix} a_{Fe} \\ b_{Fe} \end{pmatrix} = \begin{pmatrix} 3 & 1 \\ -1 & 4 \end{pmatrix} \begin{pmatrix} a_{Pt} \\ b_{Pt} \end{pmatrix} \tag{2.9}$$
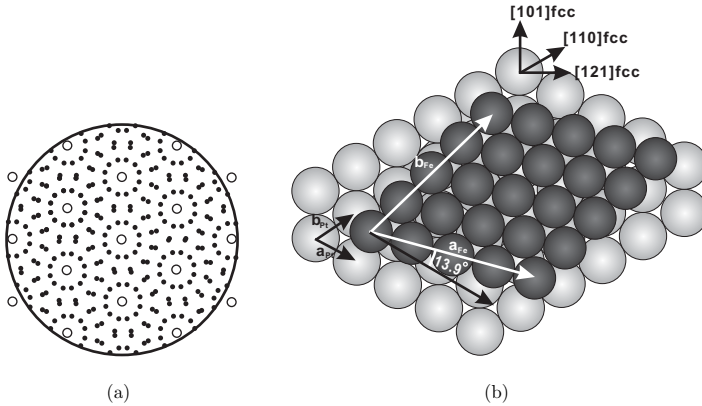
Figure 2.21 (a) Calculated kinematic LEED pattern of the $(\sqrt{13} \times \sqrt{13})$ R13.9° reconstructed layer on Pt(111). (b) A simple model for a $(\sqrt{13} \times \sqrt{13})$ R13.9° reconstructed Fe layer (black circles) on the Pt(111) surface (gray circles).

Fig.2.21 (a) shows the calculated diffraction pattern for this superstructure. It is in good agreement with the observed LEED pattern. Note the circular arrangement of superstructure peaks around the substrate spots and the double spots which form short lines between these circles. These features can also be found in Fig.2.20 (b) and (c). A possible atom arrangement within this large supercell is provided for illustration in Fig.2.21 (b).

2.3.3 Conclusions

Fe grows on Pt(111) in 3D island or Volmer-Weber growth mode. Deposition of Fe around monolayer coverage at room temperature leads to an uncommensurate adlayer which is attributed to a Kurdjumov-Sachs-like structure. Upon annealing of this phase a rotated higher order commensurate ($\sqrt{13} \times \sqrt{13}$) R13.9° superstructure is observed which exhibits its characteristic LEED pattern between 500 K and 600 K. This stability range may indicates a well defined although not perfectly ordered adlayer structure. At 700 K a transformation to a (2×2) structure is observed, which can be attributed to the formation of an ordered FePt alloy which is known from the literature.

2.4   Growth of Rh, Ru, and Mo on Pt(997)

The interest in magnetism of metallic nanostructures is not restricted to $3d$ elements. Several studies show that $4d$ and $5d$ elements can have a magnetic ordering due to the change in the electronic structures of the valence band, which can be modified through the broken symmetry and hybridization with other materials. Calculations from the density functional theory[57–59] , for instance, predict that monatomic chains and rectangular islands of Rh, Ru, Tc and Mo on Ag(001) can have a large permanent magnetic moment.

It appears most promising to create Rh, Ru, and Mo ‡ nanostructures on the vicinal Pt(997) surface, on which various metallic nanostructures have been obtained through step decoration. However, only few studies have been carried out on the growth of Rh, Ru, and Mo on a Pt surface. It is essential to know the growth conditions in order to control the formation of a desired adsorbate structure. Calculation[98] shows that Rh, Ru, and Mo exhibit a strong tendency to alloy with Pt atoms and to diffuse into the Pt bulk. Some information on growth of these elements on the low-index Pt(111) surface is available from the literature. A previous study with field ion microscopy (FIM) of Rh on Pt(111) shows epitaxial growth of the Rh adlayers[110] . Rh thin films prepared by UHV evaporation on Pt(111) were investigated in an earlier study by AES and LEED. The investigation[111] suggests that below 400 K a 'pseudo layer-by-layer' growth takes place in which the second and third layers grow before completion of the first layer. At increased temperature, formation of bulk-like poly-crystalline Rh is observed, and alloying between Rh and Pt occurs at $T > 873$ K. The STM[112] and AES[113] measurements of a Ru thin film evaporated at room temperature on the Pt(111) surface shows a 'hit and stick' growth mode, which results in a 3D-island growth mode. A Ru thin film on Pt(110)[114] also shows 3D cluster formation from the initial stage of growth, and surface alloying to set in at some temperature well above 400 K. The growth of Mo on Pt(111) is controversial. It is reported that Mo grows epitaxially on Pt(111) at room temperature[110] . On the other hand, a LEED and AES study[115] shows that Mo on Pt(111) does not exhibit a simple layer-by-layer growth and substantial alloy formation is found.

In this section, growth of Rh, Ru, and Mo ultrathin films on the vicinal Pt(997) surface will be studied by TEAS and AES. The aim is to find if growth conditions for smooth nanostructures such as monolayers or atomic chains are experimentally

---

‡A complete and systematic study of the 4d metals is not possible because Tc is radioactive with a lifetime of a few hours. It can thus not be used in adsorption experiments.

accessible. The Pt(997) surface was prepared with repeated cycles of sputtering and annealing as described in Sec.1.2. The cleanliness of the surface was verified with AES and reproducibility of preparation monitored by the absolute intensity of TEAS diffraction patterns. The base pressure in the chamber was 2×10^{-10} mbar. High purity Rh (99.9%), Ru (99.9%), and Mo (99.95%) were evaporated from an electron bombardment evaporator. Because of the higher cohesive energy of these elements, substantially higher heating power was required for evaporation in comparison to metals studied earlier, like Fe, Ag, or Cu. During the evaporation the pressure in the chamber rose to 4×10^{-10} mbar. The flux of Rh and Ru evaporation was typically 1×10^{-3} ML/s. It was calibrated through interpretation of the oscillation of the diffraction peak at n = -3 in non-grazing scattering geometry. To monitor alloying with the Pt substrate, relative surface concentrations of Mo and Rh were obtained from AES spectra (Eq.(2.6)) measured during slow temperature ramps.

2.4.1   Growth of Rh on Pt(997)

Rh deposition for the substrate temperature range 200 K$\leq T \leq$700 K monitored *in situ* by the reflected He diffraction intensity in non-grazing geometry is shown in Fig.2.22. Three growth regimes can be distinguished: First, the monotonous decrease
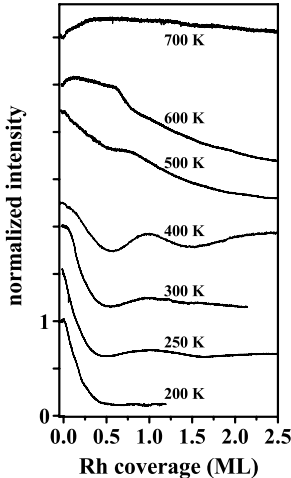
Figure 2.22 Rh deposition on Pt (997) monitored under grazing geometry ($n = -3$ peak) for the indicated temperatures. $\theta_i = 57.8$ °, $\chi = 101.8$ °, and $\lambda = 1.01$ Å. The curves were normalized with respect to the intensity before deposition. For clarity, the curves for $T \geq$200 K are vertically shifted by $+0.5$ unit for each temperature step; the curves for T=400 K and 500 K are vertically shifted by $+0.25$ and $+0.7$ unit, respectively.

of intensity at T=200 K indicates 3D island growth. Second, the decrease followed by a more or less distinct maximum for 250 K$\leq T \leq$500 K, which is assigned to Rh monolayer formation (θ_{Rh}=1.0 ML). The intensity at the maximum increases with increasing temperature due to the more efficient diffusion. At T=400 K, a second minimum at 1.5 ML followed by an increase indicate a continuing layer-by-layer growth almost to completion of the second layer. Finally, at and above 600 K, the curves are characterized by an initial increase of reflectivity, similar to the curve of Fe adsorption (Fig.2.8 (b)) at 600 K. In the case of Fe it indicated the on-set of bulk alloying. The same interpretation is likely to hold for Rh as demonstrated by the Auger spectroscopy result in Fig.2.23.

In the AES experiment 1.0 ML of Rh is deposited at 200 K. By heating the sample to the indicated temperatures and stabilizing the temperature, AES spectra are acquired for a series of increasing temperatures. For the evaluation of the Rh surface concentration the Rh 302.0 eV and the Pt 64.0 eV peak intensities were used. The relative amount of Rh is obtained from Eq.(2.6) with the relative sensitivity factor S_{Rh}=0.65. Fig.2.23 shows that the Rh concentration at the surface starts to decrease above 600 K. This result is also in good agreement with an earlier study of Rh films on Pt(111) for which it was found that bulk diffusion sets in between 623 K and 873 K[111] . Thus the initial increase in the adsorption curve indicates the diffusion of the adsorbate into the Pt bulk above 600 K. In addition, the comparison of the 600 K curve with the data from Fe adsorption (Fig.2.8 (b)) might suggest that at this intermediate temperature a surface alloy is formed, indicated by the appearance of a shallow local minimum at a Rh coverage where a maximum is observed at 500 K.

Fig.2.24 shows the diffraction patterns of 1∼4 ML Rh on Pt(997) at a series of temperatures. The film thickness is given in the figure caption. In comparison to the
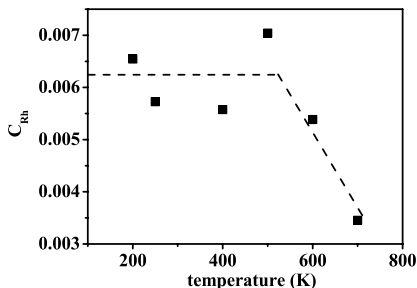
Figure 2.23 Relative amount of Rh obtained by AES and evaluated from Eq.(2.6) while ramping the temperature of 1 ML Rh on Pt(997) in steps of 50 K. Initially, Rh is evaporated at 200 K. The dashed line is a guide to the eye.

Figure 2.24 Diffraction pattern for Pt(997) after deposition of Rh at the indicated temperatures. The coverage is 3∼4 ML except for 200 K where the coverage is only 1.25 ML. Each curve is shifted by factor of 10 with respect to the curve below. $\theta_i = 57.8°$ and $\lambda = 1.01$Å.
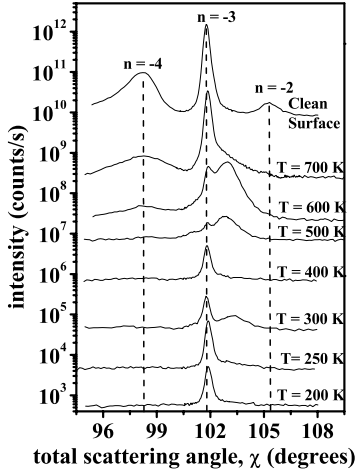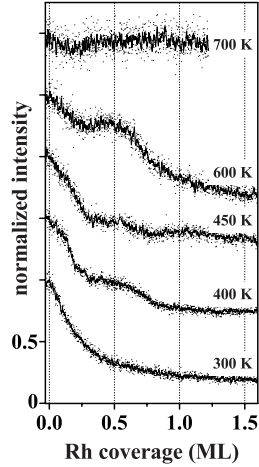
Figure 2.25 Rh deposition on Pt(997) monitored by the $n = 0$ peak for the indicated temperatures. $\theta_i = 85.0$ °, $\chi = 170.0$ °, and $\lambda = 1.01$ Å. The curves were normalized to the initial intensity and vertically offset by multiples of 0.5 unit.

pattern of the clean surface (Fig.2.24 top), the diffraction peaks are much weaker. The most striking feature is the appearance of a peak at $\chi = 103.0°$ which indicates the formation of (111) facets with a significant total surface area. The facet peak reaches its maximum at 600 K and disappears above 700 K. Its presence indicates that the periodicity of the step structure disappears and extended (111) terraces are formed. This requires a high mobility of the adsorbate atoms and suggests that maintaining the substrate step structure is energetically highly unfavorable for the adsorbate film. The re-appearance of the substrate step structure at 700 K coincides with the diffusion of the adsorbate into the bulk and a re-establishment of the Pt(997) surface morphology.

The reflected He diffraction intensity in grazing scattering geometry during Rh deposition in the temperature range 300 K≤ T ≤700 K is presented in Fig.2.25. Intensity maxima appear around θ_{Rh}=0.5 ML for temperatures between 400 K≤ T ≤600 K,

which indicates the formation of stripes with the width of several atomic rows[67,77] . This feature was observed in earlier studies always when monatomic row formation is observed. In fact, the corresponding reflectivity peak at 0.13 ML coverage appears as a shoulder in the measurements at $T = 400$ K and 450 K. This suggests that monatomic Rh chains at the steps of Pt(997) form in this temperature range, however, with a probably high defect (kink or vacancy) density.

In summary, for Rh on Pt(997) a growth behavior similar to the case of Fe on Pt(997) is observed although the defect density in the structures appears to be much higher as the reflectivities are lower and the features are less pronounced. The best condition for monatomic row formation and layer growth almost to the second layer is found around 400 K.

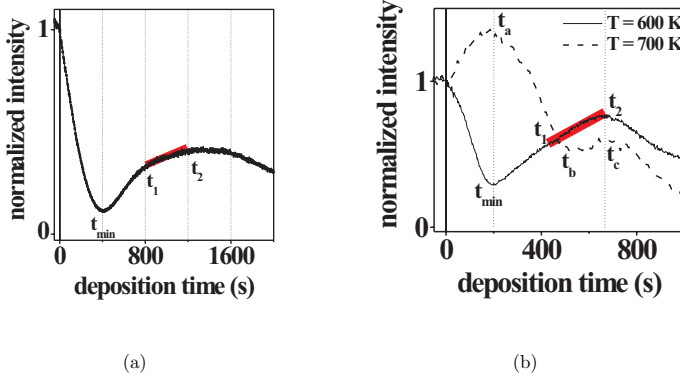## 2.4.2   Growth of Ru on Pt(997)

Fig.2.26 (a) shows the reflected He diffraction intensity in *non-grazing* scattering geometry measured during Ru deposition in the substrate temperature range 200 K$\leq$ T $\leq$700 K. These reflectivity curves exhibit maxima which are located at a coverage which increases with temperature. This observation does not allow the straight-forward calibration of the coverage scale which was possible for other adsorbates. However, a feature which is independent of temperature is found in the first extremum, which is a minimum for low temperature and a maximum for the highest temperature. This coverage may be assigned to 0.33 ML, 0.5 ML, or 1.0 ML coverage. The shape of the curves for the case of Ru deposition is parabola-like with the intensity minimum at t_{min} for $t \leq t_1$ followed by a linear increase for $t_1 < t < t_2$ (Fig.2.27(a)). The detailed analysis of the 500 K measurement in Fig.2.27(a) demonstrates that sudden changes of the slope in the curves occur at about equidistant time intervals (t_{min}, t_1, t_2): The maximum is observed at the deposition time t_2=1220 s. The ratio t_2/t_{min} would be close to 2.0 for layer-by-layer growth of metals, such as Fe and Rh on Pt(997). In the case of Ru, however, t_2/t_{min}=3.0 is found. Fig.2.27(b) shows the reflectivity dependence at T =600 K and 700 K. The curve at T =600 K is similar to that at T =500 K: The meaning of t_{min}, t_1, and t_2 in the curve for T =600 K is the same as in Fig.2.27(a). The reflectivity for T =700 K (Fig.2.27(b)) exhibits a maximum at t_a, a minimum at t_b, and a second maximum at t_c. It is found that $t_c = t_2$ and $t_a \simeq t_{min}$. This suggests that the true time period of growth is given by t_{min} and not by $2t_{min}$. Moreover, depending on temperature the first maximum shifts from $2t_{min}$ to $3t_{min}$ and no

(a)   (b)
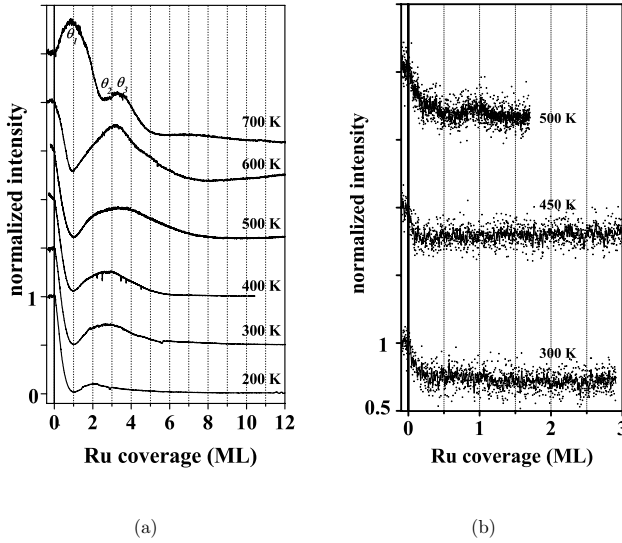
Figure 2.26 Ru deposition on Pt (997) monitored under (a) grazing geometry ($n = -3$ peak) with $\theta_i = 57.0$ °, $\chi = 99.65$ ° and (b) non-grazing geometry ($n = 0$ peak) with $\theta_i = 84.3$ °, $\chi = 168.6$ ° for the indicated temperatures. The wavelength of He-beam was 0.96 Å. The curves were normalized with respect to the intensity before deposition and vertically offset by multiples of (a) 0.5 unit and (b) 1.0 units. The characteristic coverage θ_1, θ_2, and θ_3 in (a) correspond to $t_{min}/2t_{min}$, $t_1/2t_{min}$, and $t_2/2t_{min}$ respectively. For detailed information, see text.

1/3 ML superstructures are expected for metallic adsorbates which exhibit exclusively attractive interactions. Thus an assignment of the minimum to the coverage 0.33 ML can be excluded.

The assignment of the minimum is made to 1 ML which is strongly supported by an earlier study: Hoster *et al.*[112] reported that growth of the Ru atoms on Pt(111) at room temperature exhibits 3D island growth with double layer formation. Then a nominal monolayer coverage would only fill half of the terrace leading to a reflectivity minimum. At low temperature 2 ML corresponds to a complete double layer with a reflectivity maximum (200 K data). At higher temperature (600 K) the reflectivity at this coverage is already increased and at this point a change of slope is observed in the adsorption curve. But a maximum is only reached at 3 ML which suggests that a

(a)

(b)

Figure 2.27 Ru deposition on Pt (997) monitored under non-grazing geometry ($n = -3$ peak) with $\theta_i = 57.0$ °, $\chi = 99.65$ °, and $\lambda = 0.96$ Å. for (a) T=500 K and (b) T=600 K and 700 K. A character of the linear increase followed by the parabola for $t_1 < t < t_2$ is indicated with thick bar. Typical deposition times are indicated as t_{min}, t_1, t_2, t_a, t_b, and t_c as explained in text.

low-defect morphology would require a coverage which increases with temperature.

Fig.2.26 (b) shows the reflected He diffraction intensity in grazing scattering geometry measured during Ru deposition in the substrate temperature range 300 K$\leq$ T $\leq$500 K. No indication of the formation of monatomic chains is observed in the studied range. This is a surprising result as the normal incidence measurement (Fig.2.26 (a)) indicates the formation of well ordered structures. However, the growth mode described by Hoster *et al.*[112] provides also the key to this behavior. They report that step decoration takes place, both, on the top and at the bottom of the step edge. The row which will form at the top of the step edge leads to a substantial diffuse scattering so that the weak intensity in grazing scattering geometry disappears into the background counting rate. This is exactly, what is observed in Fig.2.26 (b). An additional effect leading to a suppression of the step decoration peak is due to the fact that decoration will be accomplished only at a coverage of 2 rows. It has been shown[77,116] that peaks at grazing geometry become broadened with increasing coverage and are hardly detectable already at a coverage of 2 rows due to desynchronization of growth on different terraces.

The growth model by Hoster *et al.*[112] is ideally depicted in Fig.2.28: Ru decoration at the step starts on both, the lower and upper terrace (Fig.2.28 (a)). Assuming the row-by-row fashion of such Ru growth with double layer formation, nominal coverages

(a)   (b)   (c)
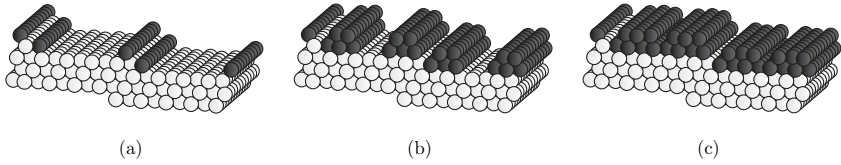
Figure 2.28 Schematic diagram of Ru growth on Pt(997) for coverages (a) 0.25 ML, (b) 1.25 ML, and (c) 1.75 ML.

of 1.25 ML and 1.75 ML Ru on Pt(997) correspond to Fig.2.28 (b) and (c). Thus, a terrace is fully covered by Ru atoms at a nominal Ru coverage of 2 ML, which would result in the maximum of the intensity curve in non-grazing indcidence at 2 ML. The assumed process of Ru decoration can be expected to depend on the thermal energy of Ru atoms. When Ru atoms are less mobile at low temperatures, Ru layers with high defect density of 1 terrace periodicity would form. Thus, the maximum of the intensity curve would appear at 2 ML coverage however with small intensity. This would correspond to the curve for $T = 200$ K in Fig.2.26 (a). When Ru atoms are mobile at increased temperatures, Ru atoms even after 2 ML coverage deposition would continue to increase the reflectivity. This may indicate that above 200 K at 2 ML nominal coverage still a significant number of surface defects or substantial surface inhomogenity exists which is continuously reduced between 2 ML and 3 ML.

The features in the intensity curve for $T = 700$ K in Fig.2.26 (a) are rather different from the curves at lower temperature. The differences might originate from alloying or a transition from double layer growth to initial single layer formation. Hoster *et al.*[112] reported that Ru does not diffuse into Pt at 400 K. Only on a sputtered Pt(111) surface they find bulk diffusion at $T = 820$ K. Their difficulty to observe intermixing as well as the fact that the reflectivity curve at 700 K exhibits distinct features which extend to long Rh deposition times indicate that no efficient bulk alloying occurs yet at 700 K.

In this section, it was shown that Ru growth on Pt(997) exhibits in its coverage and temperature behavior peculiar features that were not yet observed for any other adsorbate on Pt(997). The observed behavior is compatible with a step-decoration on both, upper and lower step edges and a double layer growth which were described in an earlier study[112] . We tentatively assigned the occurring first extremum in reflectivity to monolayer coverage. Still, a detailed picture of the growth morphology cannot be constructed, based on the He reflection data. However, the extremely high or extremely low reflectivities found in different temperature ranges as well as slope changes reproducibly found at specific deposition times suggests that these features may be attributed to well

defined surface structures.

2.4.3   Growth of Mo on Pt(997)

Fig.2.29(a) shows He reflection data during Mo growth on Pt(997) for temperatures 150 K$\leq T \leq$600 K monitored in non-grazing scattering geometry (n = -3 diffraction peak). For all temperatures the He reflectivity decreases monotonously and no temperature is found for which pronounced maxima of the diffraction intensity as a function of coverage occur. This is an indication of a 3D growth mode. Also in grazing incidence (Fig.2.29(b)) maxima which may give an indication for coverage calibration are absent and no monatomic row formation is observed. After deposition of Mo at different

(a)   (b)
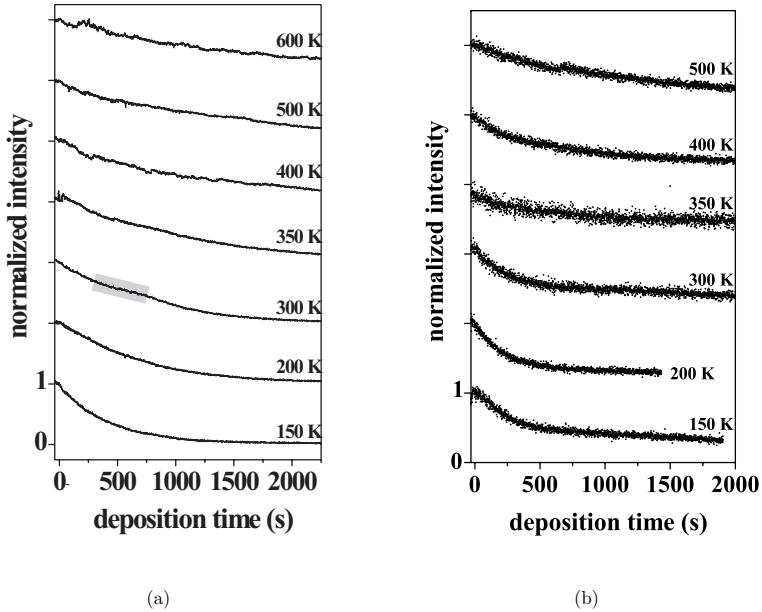
Figure 2.29 Mo deposition on Pt (997) monitored under (a) non-grazing geometry ($n = -3$ peak) with $\theta_i = 57.8$ °, $\chi = 101.8$ ° and (b) grazing geometry ($n = 0$ peak) with $\theta_i = 85.0$ °, $\chi = 170.0$ ° for the indicated temperatures. The wavelength of the He-beam was 1.01 Å. The curves were normalized with respect to the intensity before deposition and vertically offset by multiples of 1.0 units. A change in the slope observed at 300 K is indicated as gray box, which will be discussed in the text.
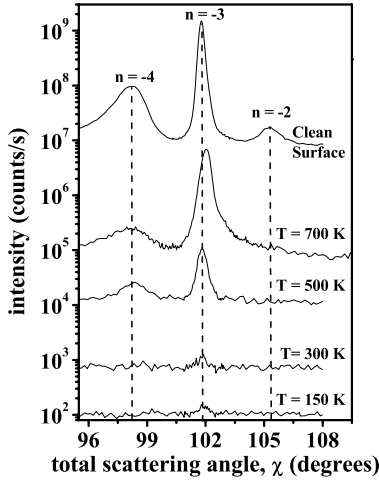
Figure 2.30 Diffraction pattern of Pt(997) after Mo deposition at the indicated temperatures. The total deposition time was between 2800 s and 3500 s. Each curve is shifted by a factor of 10 with respect to the curve below.

temperatures, diffraction patterns are measured (Fig.2.30). The temperatures at which the measurements are made are the same as those of deposition. Mo deposition time was between 2800 s (at 150 K) and 3500 s (at 500 K). It is found that the central diffraction peak in the scattering geometry, n = -3, is almost undetectable up to room temperature and becomes well observable at 500K and 700K. No facetting peak is observed. The results thus indicate a non-periodic and rough surface morphology.

The diffusion of Mo into the Pt bulk is studied by AES: After deposition of Mo on Pt(997) for 2400 s at T =120 K, the temperature is increased in 50 K steps to T =850 K. An AES spectrum is measured at each temperature at which the total dwell time is less than 20 minutes. Fig.2.31 shows the relative amount of Mo near the surface obtained from relation Eq.(2.6) with the Mo peak at 28.0 eV and Pt peak at 43.0 eV. The sensitivity factor of Mo is S_{Mo}=0.325. It is found that there is a decrease of C_{Mo} above 700 K although the surface coverage is not found to drop to zero in the observed temperature range. In a previous study by Bassett[115] it is reported that diffusion of Mo atoms into the Pt bulk starts at 700 K which is in agreement with the AES result in Fig.2.31.

As we pointed out, due to the growth of a rough morphology no clear indication of monolayer coverage is obtained. Thus an attempt is made to estimate the coverage which is actually investigated in this study. Mo is evaporated under the same conditions (electron emission 32 mA and high voltage 900 V for the Omicron triple evaporator)
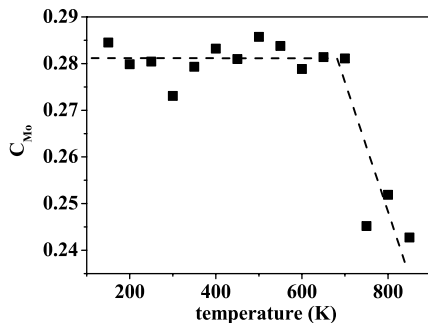
Figure 2.31 Relative amount of Mo obtained by AES and evaluated from Eq.(2.6) while ramping the sample temperature in steps of 50 K. The dashed line is a guide to the eye.

used for Rh evaporation. Because the cohesive energy of Mo is much larger than that of Rh (for instance, the melting points of Mo and Rh are 2895 K and 2236 K, respectively), a smaller amount of Mo would be evaporated than that of Rh for the same evaporator parameters. Thus, an upper coverage limit for Mo can be estimated from the total deposition time: During 2400 s one may deposit up to 5 ML of Mo. The AES evaluation in Fig.2.31, on the other hand, suggests a significant coverage: The values in Fig.2.11 (1 ML Fe on Pt(997)) and Fig.2.23 (1 ML Rh on Pt(997)) are in the range of $C = 0.01 \sim 0.04$ at low enough temperature. If the value of $C = 0.28$ in Fig.2.31 is compared with the value of 0.04, one obtains an amount of Mo corresponding to >7 ML. From these two pieces of information a deposition rate of approximately 1 ML per 500 s is estimated. With this indication, we can identify a shoulder with low intensity in the deposition curve at 300 K which is marked by a grey box in Fig.2.29 (a). Even though the curve for 300 K exhibits a monotonous decrease, at deposition time 600 s the slope shows a clear change which does not occur for other temperatures. The agreement of the estimated monolayer deposition time with the center of this shoulder suggests that there is a weak indication of monolayer formation in the reflectivity data.

To summarize, Mo on Pt(997) exhibits a basically rough growth morphology in the studied adsorption temperature range 150 K to 600 K. This suggests a prevalent 3D island growth mode with even no indication of step decoration. A weak feature assigned to monolayer formation can be identified at a deposition temperature of 300 K where the ordering tendency at the surface may be most pronounced. Diffusion of Mo atoms into the Pt substrate occurs above 700 K.

2.5 What facilitates monatomic row formation on Pt(997)?

In the previous sections, it is shown to which degree the vicinal Pt(997) surface can be used as a template for the formation of metallic nanostructures of Fe, Rh, and Ru. The comparison of the growth of Fe on Pt(997) and Pt(111), for example, shows that the existence of surface steps can force the formation of 2D Fe layer and 1D monatomic chains even when there is a thermodynamic tendency for island formation. However, it is also demonstrated that step decoration and step-flow growth cannot be obtained for Mo.

We may thus ask the following fundamental question: Which is the physical property that determine the occurrence of step decoration and the defect density during step-flow growth of metals on Pt(997)? To answer this question, theoretical calculations and complementary experiments would be necessary. However, with all the shortage of such deeper knowledge, a qualitative answer will be tried in this section.

One parameter determining the growth mode might be the matching of the bulk crystal structures of adsorbate and substrate. Fig.2.32 (a) shows a comparison of atomic radii of adsorbates and the value of Pt given by the dashed line. The elements were arranged along the x-axis in a sequence from "best" to "worst" step decoration observed in grazing geometry during growth near room temperature. The results of TEAS studies on Pt(997) in this work and earlier publications[51, 53, 67, 117] suggest the qualitative ordering as follows: Ag > Cu > Fe > Co > Rh > Ru > Mo. This order also represents the quality of step-flow-growth observed. Fig.2.32 (a) shows that there is no correlation of growth and lattice mismatch, neither absolute mismatch nor its sign. Fe and Ag *e.g.* exhibit a well resolved step decoration peak (for Fe see Sec.2.2.2) while they exhibit the largest mismatch in contrast to Mo which has the smallest misfit while no step decoration is observed (Sec.2.4.3). The same examples of Fe and Mo which are both bcc metals demonstrates that the crystallographic lattice type, bcc or fcc, also has no decisive influence on the observed growth mode. It is observed, however, that Mo which is the element with the "worst" growth behavior is also the element with the highest melting temperature. In fact, the correlation of growth quality and cohesive energy is obvious from Fig.2.32 (c). As the surface energy reflects also to some degree the binding energy per bond, a qualitatively similar correlation is found for the surface energy as in Fig.2.32 (b).

It is thus found that there is a positive correlation between the observation of step decoration and step-flow growth and cohesive energy. The physical reason behind this
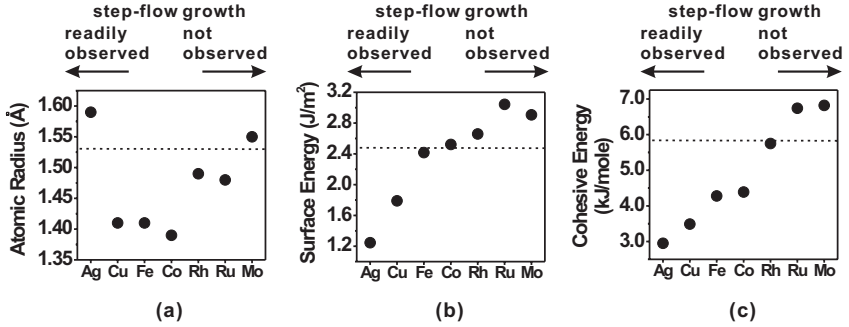
Figure 2.32 Physical properties in relation to the epitaxial growth on Pt(997) for various metals ever measured. (a) atomic radii calculated by MTO method[118] ; (b) measured surface energies[119] ; (c) measured bulk cohesive energies[120] . The metals (x-axis) are sorted according to intensity in the first row formation peak observed by TEAS in non-grazing scattering geometry at room temperature. Dotted lines in each panel correspond to the values of Pt.

correlation may be the strength of bonding to the substrate and to other adsorbates which can determine equilibrium morphology and the dynamics of surface processes. Presently, the correlation may provide a guideline for future experiment to decide which elements might be more promising than others for monatomic row formation on Pt(997).

Chapter 3

Magnetism of Fe nanostructures

In this chapter, studies on the magnetism of different low-dimensional Fe nanostructures will be presented. The magnetic properties of monatomic chains of Fe atoms, stripes of only a few atoms in width, islands, fcc monolayer and even FePt surface alloys is investigated by XMCD and by MOKE and correlated to the atomic structure. This chapter is organized as follows. Sec.3.1 summarizes the principles of XMCD and MOKE. While XMCD can successfully be used to investigate Fe structures formed of sub-monolayer coverage of Fe, both techniques can be used complementarily for ultrathin Fe films of only a few atoms in thickness. The magnetic properties of various Fe structures, investigated by XMCD, are presented in Sec.3.2. Magnetic measurements by magneto-optical Kerr effect are described in Sec.3.3. A comparison of different Fe nanostructures and their resulting magnetic properties, as well as a discussion of the observed results will be given in Sec.3.4.

3.1   Investigation of the magnetism of thin films and nanostructures by light

For the characterization of thin film magnetism several methods, such as Bitter patterns, transmission electron microscope (TEM)[121, 122], scanning electron microscopy with polarization analysis (SEMPA)[123], magnetic force microscope (MFM)[10], photoelectron emission microscopy (PEEM)[124] *etc.* have been used. To achieve the required sensitivity for the investigation of nanostructures of only a few atoms in size, efforts are made to push the detection limit towards atomic resolution by spin-polarized STM[125]. In the present study, `photons` are used as an integral method for magnetic inves-

tigation. On one hand, the X-ray magnetic circular dichroism (XMCD) of magnetic nanostructures is measured. Such experiments require monochromatic light from a synchrotron radiation source. On the other hand, magneto optical Kerr effect (MOKE) measurements are performed. The advantage of the XMCD is its element specificity, its sensitivity to even lowest coverage of magnetic material and its dependence on spin-orbit split electronic states of the material investigated. Thus, information on the spin and orbital moments of the sample can be obtained independently. In contrast, MOKE cannot distinguish between magnetic contributions of different elements. The advantage of MOKE is in its simplicity. Semiconductor laser diodes are required as light source, allowing for convenient use in any laboratory, independent of synchrotron facilities. Both methods can complementary be used for the study of the magnetism of ultrathin films grown on single crystal surfaces.

3.1.1   X-ray magnetic circular dichroism (XMCD)

Experiments

The X-ray magnetic circular dichroism is based on the dependence of absorption of circular polarized light on the magnetization of the sample[126, 127] . To probe the magnetization dependent resonant absorption of light, a light source providing polarized light with tunable energy is required. Thus, XMCD is typically measured using synchrotron light. Synchrotron light has two major advantages over laser light: (1) The white light radiated from the synchrotron radiation has a broad wavelength spectrum, from which the required wavelength can be selected by a monochromator. Magnetism can thus be investigated element-specifically by tuning to the absorption edges of the element investigated. (2) The intensity of the synchrotron radiation allows to detect even coverages as low as 1/100th of a monolayer. (3) The polarization of the beamline light can be accurately set by the beamline optics.

The XMCD experiments described here have been performed at different light sources: the elliptical-wiggler beamline BL 4.2 in ELETTRA (Trieste, Italy); the bending magnet beamline PM-3 at BESSY II (Berlin, Germany), and the helical undulator beamline ID08 at ESRF (Grenoble, France). The characteristics and the related beamline optics of the radiation of the bending magnet, wiggler, and undulator are well summarized elsewhere[128] .

Clean and well-ordered Pt(997) and Pt(111) surfaces were prepared by the procedures described in Sec.1.2 and 2.3. Low energy electron diffraction (LEED) experiments have been performed to check cleanliness and structural ordering of the substrate sur-
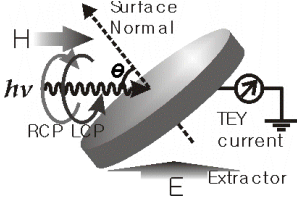
Figure 3.1 Geometry of XMCD measurements by detection of the TEY current and definition of the X-ray incidence angle θ. The magnetic field **H** is applied parallel to the direction of light.

faces by monitoring the respective diffraction pattern. Fe was evaporated at a substrate temperature of $T = 300$ K for pure Fe layer formation, and at $T = 520$ K for Fe-Pt surface alloy formation. In contrast, 3D island growth is found for Fe on Pt(111) without the presence of substrate steps. The samples with Fe adlayers were transferred *in situ* to the magnetism chamber for magnetic investigation directly after the preparation.

The X-ray absorption was measured my monitoring the total-electron-yield (TEY) current of the sample as a function of the energy of the light and the magnetization of the sample. The TEY current is a result of cascade Auger processes caused by photon absorption and is proportional to the absorption coefficient μ[129–131] , as explained thoroughly in Appendix.B. Fig.3.1 shows a schematic diagram of the XMCD experiment setup. From the synchrotron beamline, left or right circularly polarized (LCP or RCP) photons are incident on the sample surface at an angle θ with respect to the surface normal. The sample is electrically insulated with respect to ground. Thus, the TEY current can be measured as a sample current. The magnetic field was applied parallel to the propagation direction of the light. By varying the orientation of the sample with respect to the propagation direction of the light θ, the directional dependence of the magnetization, *i.e.* the magnetic anisotropy, can be investigated. To avoid artifacts from the Lorentz motion of the secondary electrons under the applied magnetic field, an electric field is applied to the sample from an electrode at high voltage close to the sample surface.

Fig.3.2 (a) shows typical X-ray absorption spectra (XAS) obtained on 2.0 ML Fe on Pt(997) at the Fe $L_{2,3}$ absorption edges for right and left circular polarized (`RCP` and `LCP`) light. The XMCD spectrum in Fig.3.2 (b) is obtained by calculating the difference of both spectra. The non-zero difference of the absorption of right and left circularly polarized light (μ_+ and μ_-) is characteristic for the Fe sample carrying a net magnetization. The areas A_2 and A_3 indicated in Fig.3.2 (b) are representative for the magnetism of the investigated sample. In particular, the orbital and spin magnetic moments (m_L and m_S) can be obtained from the sum-rule[132–134] :

$$\frac{m_L}{m_S + 7\langle T \rangle} = \frac{m_L}{m_{S,eff}} = \frac{2}{3}\frac{A_3 - A_2}{A_3 + 2A_2} \tag{3.1}$$
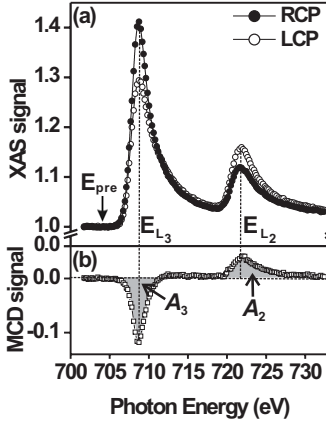
Figure 3.2 (a) XAS for light of opposite circular polarization (RCP and LCP) obtained on 2 ML Fe / Pt(997) under normal incidence. The two XAS spectra were normalized to the intensity at E_{pre}. The spectra show the $L_{2,3}$ absorption edges of Fe in remanence after magnetization of the sample by a magnetic field of 0.1 T. (b) The XMCD spectrum obtained as the difference between the two spectra in (a).

where $m_{S,eff} = m_S + 7\langle T \rangle$ and $\langle T \rangle$ is the intra-atomic dipole operator. The origin of the sum-rule will be discussed in the next section.

The angle of incidence of the light θ can be varied between 0° and 60°. Thus the measurement is sensitive to out-of-plane and in-plane components of the magnetization. The magnetic measurements on Pt(997) have typically performed along the directions shown in Fig.3.3: $\overrightarrow{\alpha}$ is perpendicular to the surface, thus 6.5° off the [111] direction; $\overrightarrow{\beta}$ is $\sim 70°$ away from $\overrightarrow{\alpha}$ and perpendicular to the steps ([11$\bar{2}$]); $\overrightarrow{\gamma}$ is $\sim 70°$ away from $\overrightarrow{\alpha}$ and along the steps ([1$\bar{1}$0]). A measurement of the angular dependence of the magnetization in the whole accessible range of θ was not performed due to the measurement time of approx. 1 hour per spectrum and the limited lifetime of the nanostructure samples until oxidation. It is noted that θ is kept smaller than $\theta = 70°$ because part of the projected beam, which has a typical diameter of 200 μm at normal incidence ($\theta = 0°$), can miss the 9 mm wide sample thus the signal can degrade. Measurements along the same directions were also made for the Fe on Pt(111).

The X-ray absorption can be used to obtain element specific hysteresis loops. This is done by monitoring the XAS is in resonance at the element's magnetically sensitive
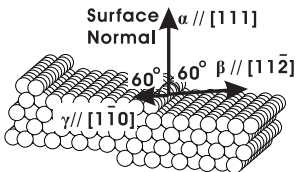

Figure 3.3 Definition of the three principal measurement directions, denoted as $\vec{\alpha}$, $\vec{\beta}$, and $\vec{\gamma}$, with respect to the crystallographic directions of Pt(997).
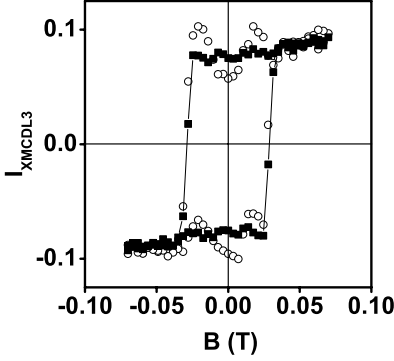
Figure 3.4 Hysteresis loop measured at the Fe L_3 edge for 3.0 ML Fe on Pt(997) measured in $\vec{\beta}$ direction at 100 K. The $I_{XMCDL3} = \mu_+(E_{L_3})/\mu_+(E_{pre}) - 1$ is proportional to the sample magnetization. The data (open circles) contain artifacts at $B \sim 0$, which are removed by a procedure described in Appendix.B. As a result, the hysteresis loop (filled square) is obtained.

absorption edges, such as the L_3-edge of Fe. During these measurements, the helicity is kept fixed and the XAS signal is measured as a function of the applied field, **B**. In this chapter, hysteresis loops of Fe are taken at the L_3 absorption edge from the ratio of $\mu_+(E_{L_3})/\mu_+(E_{pre})$. Fig.3.4 shows a characteristic hysteresis loop of 2.0 ML Fe on Pt(997) measured in $\vec{\beta}$ direction at $T=100$ K. An exceptionally large perturbation of the sample current is observed at **B** ~ 0 and found to be independent of the photon energy. This behavior of the TEY measurement is interpreted as an artifact due to the Lorentz motion of the secondary electrons under the magnetic field. A procedure to remove this effect is presented in Appendix.B.

In the limit of ultrathin films, the TEY signal is proportional to the volume of the probed adsorbate as well as $\mu^{130,135-137}$. In resonance, the intensity of the L_3 edge increases with the volume (or coverage in our case). This fact can be used to get an additional relative control of the film thickness from the spectra. Fig.3.5 shows the relationship between the nominal film thickness, as calibrated by a quartz balance, and the L_3 peak height. This L_3 peak height is defined as L_3 edge jump (`ejp`) as in the inset of Fig.3.5. A linear interpolation of the background between $\mu(E_{pre})$ and the minimum between the L_3 and L_2 edges (dotted line) is used as reference to determine the peak height at the L_3 edge. The `ejp` is defined here as peak height with respect to the dotted line minus 1. The solid curve in Fig.3.5 is a fit to the experimental data. This curve shows a linear increase of the `ejp` with the nominal film thickness in the thickness range investigated. Deviations from this linear behavior are observed for small coverage below 1 ML. The Fe thickness scale in Å is derived from the quartz balance reading with parameters set for growth of bcc(100) Fe layers. The monolayer scale is achieved
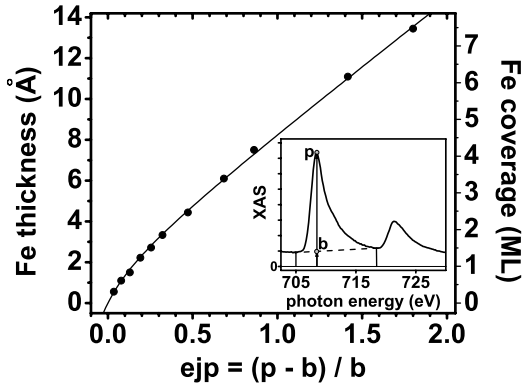
Figure 3.5 Correlation between the thickness of the Fe layer as calibrated by a quartz microbalance and the L_3 edge jump (`ejp`). The ejp is calculated from the intensities denoted **b** and **p** in the inset and the formula below the x-axis.

from the Å scale by a conversion factor of 1.8, characteristic for pseudomorphic ML's on Pt(111). The actual atomic density per layer depends on growth structure and may change with the thickness of the deposited film. Fig.3.5 allows to derive the Fe coverage directly from a given XAS spectrum and will be used for both substrates Pt(111) and Pt(997). It is verified experimentally that the same calibration curve is valid at incidence angles of $\theta = 0°$ and $\theta = 60°$.

Basics of the X-ray magnetic circular dichroism (XMCD)

The photons used in this work are X-rays of energy less than 1 keV, thus the photoelectric effect represents the dominant photon-solid interaction[61] . In the regime of the photoelectric effect, photoelectrons from the core level are excited into unoccupied states, or even leaving the sample as a result of the photon absorption. The measurements of the kinetic energy of the photoelectron leaving the sample is typically done during X-ray photoelectron spectroscopy (XPS). Of interest here is rather the energy dependent total electron yield generated by X-ray absorption (X-ray absorption spectroscopy, XAS), since this yield contains information of the electronic structure of the sample. A typical example for XAS was discussed for a 2 ML thin Fe film in Fig.3.2. Resonant transitions of the electrons from the $2p_{1/2}$, $2p_{3/2}$ levels of Fe to the unoccu-

pied states just above the Fermi level appear as the Fe $L_{2,3}$ absorption edges. Thus, the spectrum probes the $3d$ local density of states (LDOS) of Fe at the Fermi energy, which is directly related to the magnetization of the sample. The dependence of the XAS spectra on the polarization state of the light is commonly dubbed X-ray magnetic circular dichroism (XMCD), which is explained in more detail in the following.
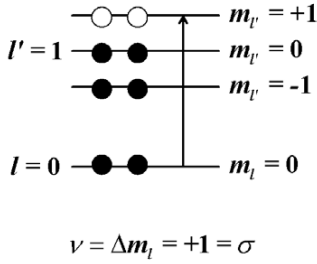
The term *dichroism* refers the polarization dependence of an optical property of a solid, *e.g.* the absorption coefficient μ of light[126, 138] . Such a dependence can originate in a particular chemical bonding, charge distribution, or local symmetry. The magnetic dichroism originates in the asymmetry of the local density of states near the Fermi energy, which is the $3d$ band in the case of Fe, Ni or Co. The asymmetry of the LDOS results in the existence of unpaired electrons, and hence a magnetic moment. The difference of the LDOS at E_F makes the resonant transition of electrons from a core state to E_F, and hence the absorption of circular polarized light, dependent on the sample magnetization and the light helicity. Depending on the polarization state of the used light, one distinguishes between linear and circular dichroism. The term 'magnetic linear dichroism' (MLD) refers to the difference in the absorption coefficient $\Delta\mu = \mu_\parallel - \mu_\perp$ of linearly polarized light when the incident light is parallel or perpendicular to the magnetic easy axis of a magnetic material, which could be a ferro- or antiferromagnet. Magnetic circular dichroism (MCD) on the other hand, $\Delta\mu = \mu_+ - \mu_-$, is caused by the relative orientation of the incident photon helicity with respect to the magnetic polarization of a ferro- or ferrimagnet. Because a ferromagnetic ordering of Fe on Pt(997) and Pt(111) is the main concern of this work, MCD was explicitly used in this work and is described in this section.

A photon incident on an atom is considered here. The photon posesses circular polarization and a normalized wave vector $\hat{\boldsymbol{q}} = \overrightarrow{\boldsymbol{q}}/|\overrightarrow{\boldsymbol{q}}|$, where $\overrightarrow{\boldsymbol{q}}$ is the total wave vector with magnitude $|\overrightarrow{\boldsymbol{q}}| = 2\pi/\lambda$ for the wavelength λ of the photon. The total angular momentum of the photon is given as $\boldsymbol{\sigma} = \sigma\hat{\boldsymbol{q}}$, where σ is the photon helicity; $\sigma = +1$ for right-circular polarization (RCP) and $\sigma = -1$ for left-circular polarization (LCP). Let's assume that $\boldsymbol{J}$ and $\boldsymbol{J'}$ are the total angular momenta of the atom before and after the absorption of photon energy, respectively. From the conservation of the total angular momentum, $\boldsymbol{J'}$ is given as

$$\boldsymbol{J'} = \boldsymbol{J} + \boldsymbol{\sigma} \tag{3.2}$$

For the unit vector of the preferred magnetic axis of the atom $\boldsymbol{m}$, the projection of $\boldsymbol{J}$ along $\boldsymbol{m}$ is defined as $M = \boldsymbol{J} \cdot \boldsymbol{m}$. Likewise, the projection of the angular momentum after absorption M' is defined as

$$M' = \boldsymbol{J'} \cdot \boldsymbol{m} = (\boldsymbol{J} + \boldsymbol{\sigma}) \cdot \boldsymbol{m} = M + \sigma(\hat{\boldsymbol{q}} \cdot \boldsymbol{m}) \tag{3.3}$$

$l' = 1$
$m_{l'} = +1$
$m_{l'} = 0$
$m_{l'} = -1$

$l = 0$
$m_l = 0$

$\nu = \Delta m_l = +1 = \sigma$

Figure 3.6 Schematic energy diagram of the hypothetical atom, which can absorb only the energy of right circularly polarized photons. Energy states with and without electrons are indicated as filled and hollow circles, respectively.

Let us define the difference in the angular momentum projection along m as ν, then

$$\nu \equiv \Delta M = M' - M = \sigma(\hat{q} \cdot m) \tag{3.4}$$

For given scattering geometry, $\hat{q} \cdot m$ is constant. When the photon propagates parallel to the magnetization axis, $\hat{q} \cdot m = +1$. It is assumed further that the hypothetical atom has six p-electrons which occupy single-particle orbitals without intrinsic spin according to the schematic energy diagram given in Fig.3.6. In this case, $\Delta M = M' - M = \Delta m_l$, where m_l is the magnetic quantum number. The dipole selection rule is $\Delta m_l = \pm 1$. Because the state of $m_{l'} = -1$ is already occupied, absorption of the photon energy occurs only when $\Delta m_l = +1$ which corresponds to $\nu = +1 = \sigma$. This means that only right circularly polarized light is absorbed[126] .

   This simple model already describes the basic mechanism of dichroism. However, electrons in a ferromagnetic solid respond in more complex ways, due to the spin-orbit splitting of the core-level and the exchange splitting of the density of states at the Fermi energy. The spin-orbit splitting is a relativistic phenomenon and arises from the interaction between the spin with its own magnetic field produced by its orbital motion around the positively charged nucleus. The resulting energy level splitting is determined by the nature of spin-orbit coupling $l \cdot s$ which results in different total angular quantum number $j = l + s$ with the same orbital quantum number l. For instance, the $2p$-level of Fe becomes spin-orbit split according to $l \cdot s$ as in Fig.3.7. Orbital and spin moments are aligned parallel in the $2p_{3/2}$ state with coupling $l \cdot s_{j=3/2} = +1/2$ and antiparallel in the $2p_{1/2}$ state with coupling $l \cdot s_{j=1/2} = -1$ since

$$l \cdot s = \frac{1}{2}\{j^2 - l^2 - s^2\} = \frac{1}{2}\{j(j+1) - l(l+1) - s(s+1)\} \tag{3.5}$$

From the selection rule $\Delta J = 0, \pm 1$, a spin dependent transition can occur even with the same orbital quantum number. This selection rule for the absorption of photons
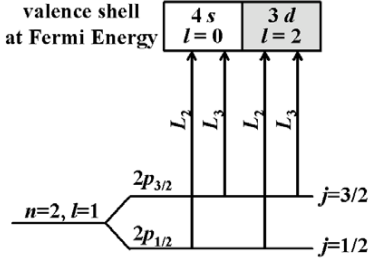
Figure 3.7 Dipole allowed transitions from the $2p_{1/2}$, $2p_{3/2}$ spin-orbit split core levels. In the $L_{2,3}$ transitions of a $3d$ metal, $p \rightarrow d$ channels are more favorable than $p \rightarrow s$ channels[139].

becomes $\Delta \boldsymbol{J} = \pm 1$ because of the three body process as in Eq.(3.2). Because spins are not strongly coupled to the orbital angular momentum, there is no change in the total spin, $\Delta \boldsymbol{S} = 0$. Therefore, the selection rule becomes $\Delta \boldsymbol{L} = \pm 1$.

Thus, for any element of interest, one can select the energy for a resonant photo-electron transition from a core shell to a valence sub-state from the consideration of the selection-rule with spin-orbit splitting. Such a transition is commonly called *absorption edge*. This idea is further discussed on the example of Pt. The electronic configuration of a single Pt atom is $[\text{Xe}]4f^{14}5d^{9}6s^{1}$. The $4f$-shell is fully occupied, the $5d$-shell misses one electron, and one electron occupies the $6s$-shell. From the selection-rule one finds that the $L_{2,3}$, $M_{2,3}$, $N_{2,3}$, $N_{6,7}$, and $O_{2,3}$ edges, as shown in Fig.3.8, correspond to transitions to the $5d$ state. Although Pt is paramagnetic in the bulk phase, it has been shown in several experiments mainly on multilayered systems[16,140] and bulk alloys[140–142] that Pt can carry an induced magnetic moment. In this case, the $5d$ state of Pt exhibits exchange splitting which can be detected by measuring resonant electronic transitions into this state at the described absorption edges.

Dichroism in the case of transitions from spin-orbit split core-shell to valence sub-states can be described well by a two-stage process: First, a circularly polarized photon excites an electron from a core level. In this process, the probability of RCP- and LCP-photons to excite the core electrons with up- and down- spin is different. Second, this electron settles into the unoccupied valence state. The transition rate depends on the number of empty final states with spin parallel to the photoelectron spin. In a ferro-magnet the differences in the density of states of spin-up and spin-down electrons leads to spin dependent transition probabilities. The transition rates thus becomes different for RCP- and LCP- photons.

Let us assume that the photon is propagating parallel to the magnetization axis, hence $\hat{\boldsymbol{q}} \cdot \boldsymbol{m} = +1$. For simplicity, only the spin-polarized density of states is considered and the orbital-polarization will be considered in the next section. The absorption coef-
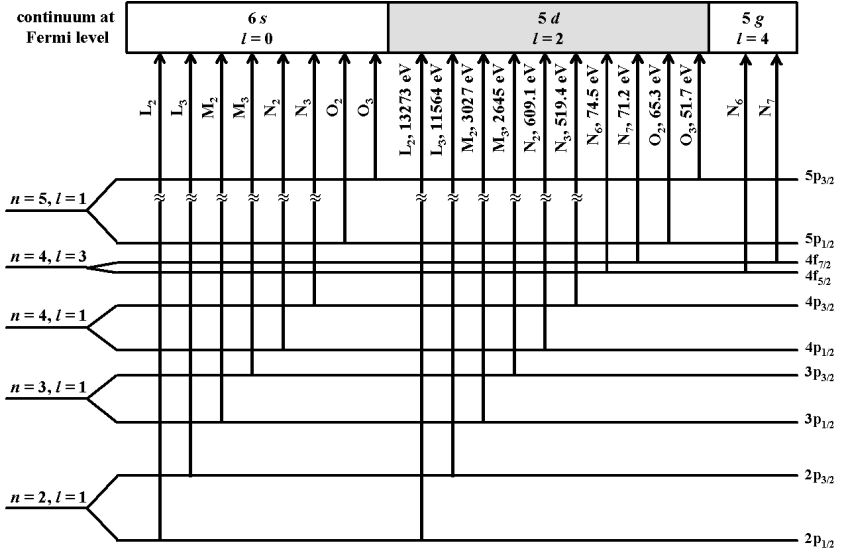
Figure 3.8 Dipole transitions of Pt from the spin-orbit split core shell to the $5d$ band at the Fermi level from the selection rule $\Delta l = \pm 1$[143] . Other channels of the transitions satisfying the selection rule from the equivalent core shells to $6s$ and $5g$ are indicated together.

ficient $\mu_{+,\ S}$ * for $\sigma = +1$ (right circularly polarization) can be written from the Fermi's Golden rule as

$$\mu_{+,\ S}(E) = C\{p_+(\uparrow)\rho_\uparrow(E) + p_+(\downarrow)\rho_\downarrow(E)\} \tag{3.6}$$

where C is a proportionality constant, $p_+(\uparrow, \downarrow)$ is the relative portion of spin-up/down polarization of the photoelectrons, and $\rho_{\uparrow,\downarrow}(E)$ is the unoccupied density of states for spin-up and spin-down electrons at the Fermi energy. The coefficient for the left circularly polarized photon ($\sigma = -1$) can be written equivalently as

$$\mu_{-,\ S}(E) = C\{p_-(\uparrow)\rho_\uparrow(E) + p_-(\downarrow)\rho_\downarrow(E)\} \tag{3.7}$$

Reversing the photon polarization changes the sign of the photoelectron polarization but leaves the magnitude unchanged. Thus,

$$p_+(\uparrow) = p_-(\downarrow) = p_\uparrow, \quad p_+(\downarrow) = p_-(\uparrow) = p_\downarrow \tag{3.8}$$

The fractional change of the absorption coefficient is thus given as

---

*The subscript "S" indicate only the contributions from the spin-polarized density of states.

$$\frac{\Delta\mu_S(E)}{\mu_S(E)} = \frac{\mu_{+,\,s}(E) - \mu_{-,\,s}(E)}{\mu_{+,\,s}(E) + \mu_{-,\,s}(E)} = \left(\frac{p_\uparrow - p_\downarrow}{p_\uparrow + p_\downarrow}\right)\left(\frac{\rho_\uparrow(E) - \rho_\downarrow(E)}{\rho_\uparrow(E) + \rho_\downarrow(E)}\right) = 2P_e\frac{\rho_S(E)}{\rho(E)} \quad (3.9)$$

where the charge density $\rho(E)$ is the sum of the spin-dependent contributions, $\rho_\uparrow(E) + \rho_\downarrow(E)$, and the spin-polarization is introduced as

$$\rho_S(E) = \frac{1}{2}\{\rho_\uparrow(E) - \rho_\downarrow(E)\} \quad (3.10)$$

The photoelectron polarization P_e is defined as

$$P_e = \frac{p_\uparrow - p_\downarrow}{p_\uparrow + p_\downarrow}. \quad (3.11)$$

Eq.(3.9) indicates that circular dichroism is providing information on $\rho_S(E)$ for $P_e \neq 0$.

From the Erskine and Stern model[144] , P_e can be treated as independent of the
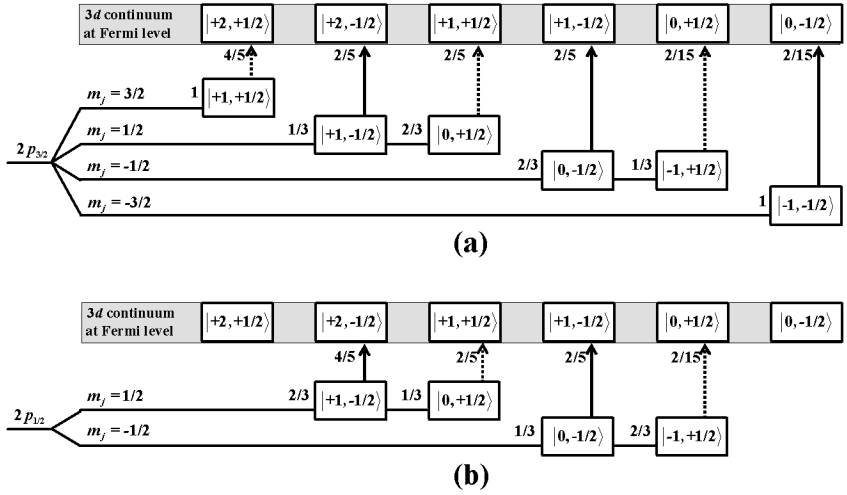
Figure 3.9 Construction of the excitation map of (a) $2p_{3/2}$ and (b) $2p_{1/2}$ core electrons of a $3d$ metal with the selection rule $\Delta m_l = +1$. Initial and final states are indicated in boxes as $|m_l, m_s\rangle$. Allowed transitions are indicated as solid and dashed lines which correspond to the case of $\nu = +1$ and $\nu = -1$, respectively. To the left of each box for an initial state, a squared Clebsch-Gordan coefficient is given for the weighting of the transition. Below each box for a final state, the relative probability of the transition from the initial to the final state is given from the Erskine-Stern model of MCD[144, 145] .

photon energy E and the spin-orbit coupling of the final state. Therefore, P_e can be estimated if the final states are known. The dipole selection rule allows $p \to d$ transitions as well as $p \to s$ transitions for $L_{2,3}$ (or $p_{1/2,3/2}$) transitions. Calculations[139] show that the transition to the $l' = l + 1$ state is several orders of magnitude stronger than to the $l' = l - 1$. Analysis of the core-level $|m_l, m_s\rangle$ with Clebsch-Gordan coefficient results in the transition map in Fig.3.9. From the map, P_e can be calculated for the transition indicated by arrows. For instance, $p_\uparrow$ and $p_\downarrow$ for the $p_{1/2}$ edge can be calculated from Fig.3.9 as following:

$$p_\uparrow \propto \frac{1}{3} \times \frac{2}{5} + \frac{2}{3} \times \frac{2}{15} = \frac{2}{9} \quad \text{and} \quad p_\downarrow \propto \frac{2}{3} \times \frac{4}{5} + \frac{1}{3} \times \frac{2}{5} = \frac{2}{3} \tag{3.12}$$

Therefore, $P_e(p_{1/2})$ is calculated as $-1/2$. With the same procedure, $P_e(p_{3/2})$ can be calculated as $1/4$. For completeness, the case of no spin-orbit splitting is considered. In this case, the generation of the photoelectron is averaged over $p_{3/2}$ and $p_{1/2}$ states, hence P_e is given as

$$P_e = \frac{2 \times (-1/2) + 4 \times (1/4)}{2 + 4} = 0 \tag{3.13}$$

which will result in no dichroism.

Derivation of the sum rules

In the evaluation of Eq.(3.9) only the spin-polarized DOS is treated: Thus Eq.(3.9) describes the spin-MCD. In comparison to other magnetometry, one of the merits of XMCD is the probing of the orbital magnetization.[7, 127, 146] In this section, an approach of probing orbital momentum by MCD will be described.

Let us consider the total and orbital densities of unpaired electrons which can be expressed as following:

$$\rho(E) = \sum_{m'_l = -l'}^{l'} \rho_{m'_l}(E) \quad \text{and} \quad \rho_L(E) = \sum_{m'_l = -l'}^{l'} m'_l \rho_{m'_l}(E) \tag{3.14}$$

where $\rho_{m'_l}(E)$ is the m'_l-projected state. In analogy to the derivation of the spin-MCD in the previous section, the absorption coefficients $\mu_{\pm, L}$ can be written as

$$\mu_{+, L}(E) = C \sum_{m'_l = -l'}^{l'} p_+(m'_l)\rho_{m'_l}(E) \quad \text{and} \quad \mu_{-, L}(E) = C \sum_{m'_l = -l'}^{l'} p_-(m'_l)\rho_{m'_l}(E) \tag{3.15}$$

where $p_\pm(m'_l)$ refers to the excitation probability to the substate m'_l. The difference between the two coefficients is

$$\Delta\mu_L = \mu_{+, L}(E) - \mu_{-, L}(E) = C \sum_{m'_l = -l'}^{l'} \{p_+(m'_l) - p_-(m'_l)\}\rho_{m'_l}(E) \tag{3.16}$$

The normalized orbital-MCD is obtained as:

$$\frac{\Delta\mu_L}{\mu_L} = \frac{3\langle m_l'\rangle\rho_L(E)}{l'(l'+1)\rho(E)} \tag{3.17}$$

The total dichroism is given as a sum of the spin-MCD and orbital-MCD, from Eq.(3.9) and (3.17) as

$$\frac{\Delta\mu}{\mu} = 2P_e\frac{\rho_S(E)}{\rho(E)} + \frac{3\langle m_l'\rangle\rho_L(E)}{l'(l'+1)\rho(E)} \tag{3.18}$$

Let us evaluate Eq.(3.18) at the $L_{2,3}$ edges. From the map in Fig.3.9, it is obtained that

$$L_2(l=1, j=1/2, l'=2): \quad P_e = -\frac{1}{2}, \quad \langle m_l'\rangle = +\frac{3}{2}$$
$$L_3(l=1, j=3/2, l'=2): \quad P_e = +\frac{1}{4}, \quad \langle m_l'\rangle = +\frac{3}{2}$$

Therefore,

$$\left(\frac{\Delta\mu}{\mu}\right)_{L_2} = -\frac{\rho_S(E)}{\rho(E)} + \frac{3}{4}\frac{\rho_L(E)}{\rho(E)} \tag{3.19}$$

$$\left(\frac{\Delta\mu}{\mu}\right)_{L_3} = \frac{1}{2}\frac{\rho_S(E)}{\rho(E)} + \frac{3}{4}\frac{\rho_L(E)}{\rho(E)} \tag{3.20}$$

From these two equations, we obtain

$$\frac{\rho_S(E)}{\rho(E)} = \frac{2}{3}\left[\left(\frac{\Delta\mu}{\mu}\right)_{L_3} - \left(\frac{\Delta\mu}{\mu}\right)_{L_2}\right] \tag{3.21}$$

$$\frac{\rho_L(E)}{\rho(E)} = \frac{4}{9}\left[2\left(\frac{\Delta\mu}{\mu}\right)_{L_3} + \left(\frac{\Delta\mu}{\mu}\right)_{L_2}\right] \tag{3.22}$$

Eq.(3.21) and (3.22) demonstrate that information about spin- and orbital- magnetism are contained in the absorption signal of a circular dichroism measurement. The spin- and orbital- magnetic moments can be extracted

$$m_S = 2\mu_B\int\rho_S(E)\mathrm{d}E \tag{3.23}$$

$$m_L = \mu_B\int\rho_L(E)\mathrm{d}E \tag{3.24}$$

Eq.(3.21) and (3.22) are, however, derived under the assumption of a single electron model and other simplification. A more rigorous treatment (such as a relativistic treatment in the final states) is required for a more realistic description. Such calculations

have been given by several authors.[132–134] The results are summarized in the following.

The expectation value of the orbital angular momentum is obtained as[132, 133]

$$\frac{1}{2n_h}\langle L \rangle = \left(\frac{\Delta\mu}{\mu}\right)_{L_3} + \left(\frac{\Delta\mu}{\mu}\right)_{L_2} \tag{3.25}$$

and the spin operator $\langle S \rangle$ together with the intra-atomic dipole operator $\langle T \rangle$ is obtained as[134]

$$\frac{2}{3n_h}\left(\langle S \rangle + \frac{7}{2}\langle T \rangle\right) = \left(\frac{\Delta\mu}{\mu}\right)_{L_3} - 2\left(\frac{\Delta\mu}{\mu}\right)_{L_2} \tag{3.26}$$

From Eq.(3.23) to (3.26), one derives the following `sum-rule` which was already applied in the previous section in Eq.(3.1):

$$\begin{aligned}\frac{m_L}{m_S + 7\langle T \rangle} &= \frac{2}{3}\frac{(\Delta\mu/\mu)_{L_3} + (\Delta\mu/\mu)_{L_2}}{(\Delta\mu/\mu)_{L_3} - 2(\Delta\mu/\mu)_{L_2}} \\ &= \frac{2}{3}\frac{A_3 - A_2}{A_3 + 2A_2}\end{aligned} \tag{3.27}$$

In summary, this section showed that the magnetism of any element can be probed by measuring the absorption probability of polarized light as a function of helicity and magnetization. The signal obtained at a resonant absorption edge which incorporates final states at the Fermi energy is yields information about the detailed electronic structure, in particular the spin polarization of the sample. The advantage of this technique is thus that spin and orbital moments can be determined separately and element specifically by application of the sum rules. These benefits will be exploited in the following to investigate the magnetism of Fe nanostructures on Pt substrates.

3.1.2 Magneto optical Kerr effect (MOKE)

It was pointed out in the previous section that synchrotron light of tunable energy and polarization can be used to obtain information about the magnetization state of ultrathin films and nanostructures. The virtues of this technique are, however, opposed by enormous experimental requirements. In many cases, it is sufficient to analyze the magnetization of ultrathin films by in-situ magneto-optical Kerr effect measurements.

The Kerr effect can be exploited to study magnetism of ultrathin films at metal surfaces[147] . In MOKE experiments, the dependence of the polarization state of light reflected at the sample surface is measured as a function of the sample magnetization. Upon reflection, the light experiences a rotation of its polarization on the one hand, and a change of the ellipticity on the other hand. Kerr rotation and ellipticity depend on the total magnetization of the probed sample volume. Fig.3.10 shows the geometry of a typical MOKE measurement. Linearly polarized light with its electric field vector $\mathcal{E}_i$ is incident on the ferromagnet. The electric field vector $\mathcal{E}_r$ of the reflected light has a different direction from $\mathcal{E}_i$ and may exhibit some ellipticity. Different MOKE geometries, determined by the alignment of the film magnetization with respect to the plane-of-incidence, are distinguished. Using the definitions given in Fig.3.10, one refers to polar MOKE geometry for $m_x = m_y = 0$, and $m_z = 1$. In analogy, longitudinal MOKE geometry is achieved for $m_z = m_x = 0$, and $m_y = 1$, and transverse MOKE geometry for $m_y = m_z = 0$, and $m_x = 1$. The details of the MOKE experiment are described in the following section.

Experiments

The MOKE measurement were done with the experimental setup shown in Fig.3.11. The apparatus is comprised of two UHV chambers for sample preparation and magneto-
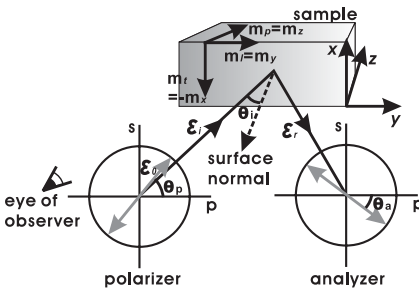
Figure 3.10 Schematic diagram of the light path in a MOKE experiment. The gray arrows indicate the direction of the linear polarization viewed from the polarizer. The optical path is shown as a solid black line. See the text for explanations.
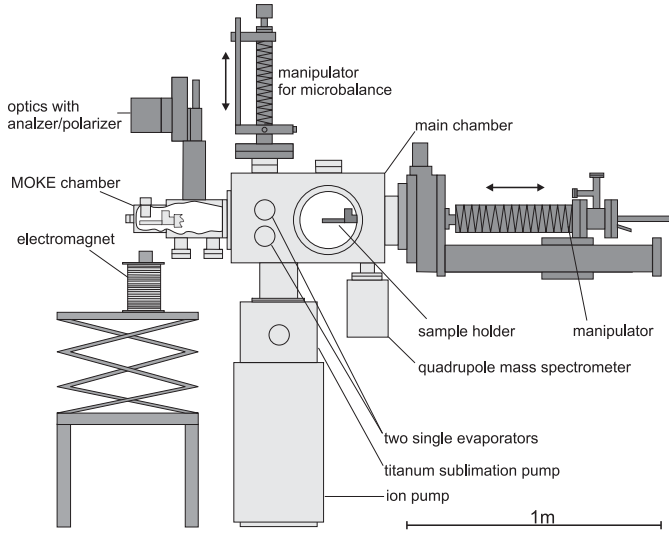
Figure 3.11 Side view of the setup of MOKE experiment[148] .

optic characterization.[148] The preparation chamber is equipped with a sputter gun, MBE single-evaporators, and quadrupole mass spectrometer. The Fe thickness was calibrated by a quartz microbalance. Fe layers were grown on the Pt substrate according to the procedure described in Sec.2.2 and 2.3. The sample was transferred *in-situ* to the MOKE chamber directly after preparation by a linear manipulator with 600 mm travel range. In the MOKE chamber, magneto-optical measurements as well as Kerr microscopy can be performed while a magnetic field is applied from outside of the chamber. The MOKE optics includes laser, polarizers, and detector and is mounted on an optical bench outside the UHV chamber. The access of the light to the sample is through a strain-free quartz glass.

The components and the alignment of the MOKE optics is sketched in Fig.3.12. All components are mounted on an optical table. Light from the laser diode is focussed by a lens onto the sample surface. The light is furthermore linearly polarized by a Glan-Thomson prism with an extinction ratio of $< 10^{-6}$. The polarization plane can be chosen between *s*- and *p*- polarization, *i.e.* with respect to the plane of incidence. According to the definition in Fig.3.10, *s*- and *p*- polarization corresponds to $\theta_p = 90°$ and $0°$, respectively. After passing the polarizer, the light is incident on the sample surface with an angle of $\theta_i \sim 10°$ with respect to the surface normal. The reflected light

passes through a second polarizer, which acts as an analyzer to probe changes of the light polarization. When both polarizers are crossed by 90°, light passes the analyzer only when the polarization of the reflected light deviates from the polarization of the incident light. The light passing the analyzer is focused by second lens on the detector.

A laser diode is used as light source (λ= 670 nm, P = 5 mW; Newport model 700c) with temperature stabilization by a Peltier element and stabilization of the optical output power. The operating temperature is stable within 0.1% and the power of the laser diode deviates maximal by 0.02% from its set-point. A photodiode converts the intensity of the reflected light into a photocurrent. This photocurrent is measured as a voltage provided by on IV-converter with an amplification of 10^5.

The longitudinal and polar Kerr geometries were realized by aligning the external magnetic field with respect to the light path. With the used magnet a maximum field within the sample plane of 160 mT is achieved. In vertical direction, a maximum field of 44 mT is provided by a set of two coils in Helmholz-like geometry, sitting on top and bottom of the chamber (Fig.3.12). The magnetic field is measured by a Hall probe, located directly at the magnet coils. The field at the sample position with respect to the one measured outside the chamber was calibrated prior to the experiments.

The MOKE hysteresis loops were measured by the following procedure: First, both angles of the polarizer and analyzer, θ_a and θ_p, are adjusted to find the *global* minimum of the detected light intensity. In this alignment of the light polarization with respect to the sample, the ellipticity of the reflected light is reduced to a minimum. Then, θ_a is rotated a few degrees off this position of global minimum. In this configuration, mainly the Kerr-rotation is measured. In contrast, the ellipticity can be determined by adjusting the angles of polarizer and analyzer to find a *local* minimum of intensity. Ellipticity measurements are performed in this configuration without rotating the analyzer away
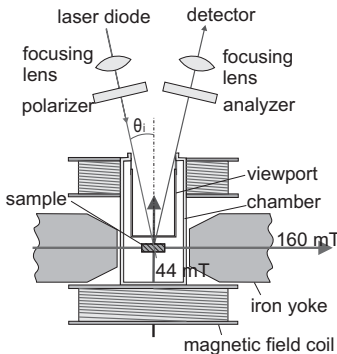
Figure 3.12 Front view of the setup of MOKE chamber in Fig.3.11 with schematic diagram of the optics[148] .

from this minimum.

Computer controlled hysteresis loops are now taken by setting the coil current step-wise and subsequently reading the respective field and the MOKE signal for a given field. To improve the signal to noise ratio, several hysteresis curves were averaged. The MOKE measurements are superimposed by Kerr rotation due to the Faraday effect of the chamber windows. This effect occurs when light travels through the glass viewport which is placed in the stray field of the magnet coils. The intensity change due to the Faraday effect is a linear function of the magnetic field. It can easily be recognized in the hysteresis loops as a linear contribution and is subtracted during data processing. The Faraday effect is also found when a non-magnetic sample is investigated by MOKE.

Principles of MOKE

On a ferromagnetic metal surface of cubic crystallographic symmetry, a permittivity tensor ϵ has three diagonal and six non-diagonal components:

$$\epsilon = \epsilon_q \begin{pmatrix} 1 & -im_zQ & im_yQ \\ im_zQ & 1 & -im_xQ \\ -im_yQ & im_xQ & 1 \end{pmatrix} \tag{3.28}$$

where ϵ_q is independent of magnetization $\mathbf{M}$, Q is a magneto-optical constant usually called Voigt constant, and $m_i = \mathbf{M}/\mathbf{M_s}$ is the component of the magnetization in direction i ($i = x,y,z$). Q is proportional to the saturation magnetization, $\mathbf{M_s}$.The non-diagonal components arise from the exchange in the ferromagnetic medium.[149, 150] The total reflectance can be obtained from Maxwell's equations from the assumption of plane-waves and conservation of the tangential components of electric and magnetic fields at the interface[128, 138, 151] . The existence of the non-diagonal components in ϵ only results in mixing of s- and p- components in the Fresnel matrix which describes the polarization state of the reflected/refracted light.

For a single boundary between the media 1 and 2, one can assume the refractive indices N_1 and N_2, and the permeability μ_1 and μ_2, all of which are usually complex. The optical system given in Fig.3.10 is assumed, in which linearly polarized light with the amplitude of electric field $\mathcal{E}_0$ has p- and s- components. The amplitude of the electric field $\mathcal{E}_i$ of a beam incident from the air (medium 1) on the surface of a ferromagnet (medium 2) *via* a polarizer at the angle θ_p is given as

$$\boldsymbol{\mathcal{E}}_i = \mathcal{E}_0 \cos\theta_p \hat{\mathbf{p}} + \mathcal{E}_0 \sin\theta_p \hat{\mathbf{s}} \tag{3.29}$$

where $\hat{\mathbf{p}}$ and $\hat{\mathbf{s}}$ are unit vectors.

The magnitude of the reflected light can be expressed by the Fresnel matrix $\mathcal{R}$ as

$$\mathcal{E}_T = \begin{pmatrix} \mathcal{E}_p \\ \mathcal{E}_s \end{pmatrix}^r = \mathcal{R} \begin{pmatrix} \mathcal{E}_p \\ \mathcal{E}_s \end{pmatrix}^i = \begin{pmatrix} \tilde{r}_{pp} & \tilde{r}_{ps} \\ \tilde{r}_{sp} & \tilde{r}_{ss} \end{pmatrix} \begin{pmatrix} \mathcal{E}_0 \cos\theta_p \\ \mathcal{E}_0 \sin\theta_p \end{pmatrix} \tag{3.30}$$

where the superscripts r and i indicate reflected and incident light, respectively. The component $\tilde{r}_{ps}$ in $\mathcal{R}$ couples the s-polarized electric field component of the incident light to the p-polarized electric-field component of the reflected light. In analogy, all $\tilde{r}_{ij}$ with i,j = p,s are defined. The full expressions for each component of $\mathcal{R}$ are[152, 153] :

$$\tilde{r}_{pp} = \frac{\mu_1 N_2 \cos\theta_1 - \mu_2 N_1 \cos\theta_2}{\mu_1 N_2 \cos\theta_1 + \mu_2 N_1 \cos\theta_2} + 2i\frac{\mu_1\mu_2 N_1 N_2 \cos\theta_1 \sin\theta_2 m_x Q}{\mu_1 N_2 \cos\theta_1 + \mu_2 N_1 \cos\theta_2},$$

$$\tilde{r}_{ps} = -i\frac{\mu_1\mu_2 N_1 N_2 \cos\theta_1 (m_y \sin\theta_2 + m_z \cos\theta_2)Q}{(\mu_1 N_2 \cos\theta_1 + \mu_2 N_1 \cos\theta_2)(\mu_2 N_1 \cos\theta_1 + \mu_1 N_2 \cos\theta_2)\cos\theta_2},$$

$$\tilde{r}_{ss} = \frac{\mu_2 N_1 \cos\theta_1 - \mu_1 N_2 \cos\theta_2}{\mu_2 N_1 \cos\theta_1 + \mu_1 N_2 \cos\theta_2},$$

$$\tilde{r}_{sp} = i\frac{\mu_1\mu_2 N_1 N_2 \cos\theta_1 (m_y \sin\theta_2 - m_z \cos\theta_2)Q}{(\mu_1 N_2 \cos\theta_1 + \mu_2 N_1 \cos\theta_2)(\mu_2 N_1 \cos\theta_1 + \mu_1 N_2 \cos\theta_2)\cos\theta_2} \tag{3.31}$$

The signal received by the detector can be expressed as a function of the analyzer angle, θ_a,

$$|\mathcal{E}_T|^2 = |\mathcal{E}_p^r \cos\theta_a \hat{\mathbf{p}} + \mathcal{E}_s^r \sin\theta_a \hat{\mathbf{s}}|^2 \tag{3.32}$$

$$= |\mathcal{E}_0|^2 |\cos\theta_a(\tilde{r}_{pp}\cos\theta_p + \tilde{r}_{ps}\sin\theta_p)\hat{\mathbf{p}} + \sin\theta_a(\tilde{r}_{sp}\cos\theta_p + \tilde{r}_{ss}\sin\theta_p)\hat{\mathbf{s}}|^2$$

The Kerr rotation θ_K and the ellipticity η_K are defined as:

$$\theta_{Ks} = -\mathbf{Re}(\tilde{r}_{ps}/\tilde{r}_{ss}),$$

$$\theta_{Kp} = \mathbf{Re}(\tilde{r}_{sp}/\tilde{r}_{pp}),$$

$$\eta_{Ks} = \mathbf{Im}(\tilde{r}_{ps}/\tilde{r}_{ss})\mathbf{Re}(\tilde{r}_{ps}/\tilde{r}_{ss}),$$

$$\eta_{Kp} = \mathbf{Im}(\tilde{r}_{sp}/\tilde{r}_{pp})\mathbf{Re}(\tilde{r}_{sp}/\tilde{r}_{pp}) \tag{3.33}$$

The magnetic information contained in the Kerr signal $|\mathcal{E}_T|^2$, as well as Kerr rotation and ellipticity θ_K and η_K arises from the dependence of $\mathbf{R}$ on m_x, m_y, and m_z. One can see that there is no Kerr rotation ($\Theta_K = \theta_K + i\eta_K = 0$) for the case of transverse geometry ($m_y = m_z = 0$, and $m_x = 1$).
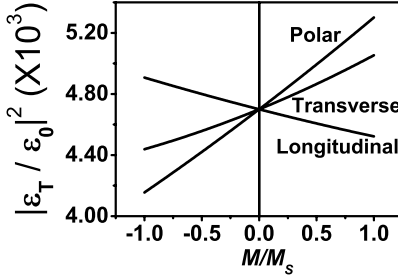
Figure 3.13 Dependence of $|\mathcal{E}_T/\mathcal{E}_0|^2$ on the sample magnetization in three characteristic MOKE geometries for the parameters given in the text.

For discussion, the dependence of $|\mathcal{E}_T|^2$ on the sample magnetization is calculated now. Here, s-polarized light with wavelength $\lambda = 670$ nm incident from the air ($N_1 = 1$) to the Fe surface is considered. The optical constant for bulk bcc Fe is $N_{2,Fe} = 2.92 - 3.39i$[154] , $Q = 0.0376 + 0.0066i$.[155] The optics are set to $\theta_p = 90 - \alpha$, $\theta_a = \alpha$, $\theta_1 = 15°$, $\alpha = 5°$. To obtain the standard equation characterizing magneto-optical phenomena, $\mu_{(1,2)}$ is set to 1 *. The dependence of $|\mathcal{E}_T|^2$ on $\mathbf{M}/\mathbf{M_s}$ in the three characteristic geometries are calculated from Eq.(3.31) and (3.33) and are plotted in Fig.3.13. It is clearly seen that there is a linear relationship between $|\mathcal{E}_T|^2$ and $\mathbf{M}/\mathbf{M_s}$ for the three geometries, making MOKE to a suitable tool for qualitative magnetization measurements. For the given parameters, polar and longitudinal geometries have the largest and the smallest amplitudes for the same magnetic moment, respectively. It is noted that polar and transverse geometries result in a positive correlation, longitudinal geometries show negative correlation with M/M_S: This correlation depends on experimental and material parameters, and have to be taken into account for the quantitative analysis of the MOKE results.

For the case of thin ferromagnetic films on a single crystal metal substrate, $\mathcal{R}$ has to be replaced by $\mathcal{R}_{tot}$ which contains effects such as the phase difference and the Faraday effect along the optical path, multiple reflection/refraction at the boundaries, and other minor effects that do not significantly contribute. A fully analytical expression of $\mathcal{R}_{tot}$ for multilayer systems using the 4×4 medium boundary matrix $\mathcal{A}$ and medium propagation matrix $\mathcal{D}$ was developed by S. Bader *et al.*[156–159] . $\mathcal{R}_{tot}$ of single layered system is given as a sub-matrix of the matrix $\mathcal{A}_0^{-1}\mathcal{A}_1\mathcal{D}_1\mathcal{A}_1^{-1}\mathcal{A}_s$. A direct derivation of $\mathcal{R}_{tot}$ for such system goes beyond the scope of this thesis.

---

*This is equivalent to replacing Q with $Q + P$ where P is the magneto-optical constant involved in the tensor of permeability. See References[152, 153] .

3.2 XMCD measurements on Fe nanostructures

3.2.1 Magnetism of ultrathin Fe layers on Pt(997) and Pt(111)

In this section, the influence of periodic Pt substrate steps on the magnetic properties of Fe adlayers at coverages between 0.5 ML and 6 ML will be studied. The results of XMCD experiments on Fe layers grown on flat Pt(111) and stepped Pt(997) will be compared. The structural analysis was described in detail in Sec.2.2 and 2.3. Its main result is summarized in Fig.3.14. Fe grown at 300 K preferentially decorates the step edges of Pt(997). The resulting Fe stripes are elongated along the step direction with virtually infinite aspect ratio. The Fe lattice can adapt the substrate lattice constant, possibly forming a a pseudomorphic layers (Fig.3.14 (a)). In contrast, Fe islands on a close-packed terrace of Pt(111) (Fig.3.14 (b)) remain compact. The LEED results suggest that these islands more easily compensate the Fe-Pt lattice mismatch by strain relaxation at the island edges.

Samples were prepared at room temperature as described in Sec.2.2 and 2.3. Wedge-shaped films with a Fe thickness linearly increasing from 0 ML to 6 ML were made by the controlled movement of a shutter in front of the sample during the evaporation. The wedges were typically 5 mm long, thus having a gradient of 1~2 Å/mm. The relative precision of the film thickness at a given measuring position is determined by the X-ray spot size of 200 μm. This, together with the accuracy of the quartz balance calibration results in an error of the thickness calibration of less than 20 % .

For Fe on Pt(997) and Pt(111), Fig.3.15 shows the remanent magnetization ($\mathbf{M_r}$) at T=100 K obtained from hysteresis loops measured at the Fe L_3 edge. The XMCD signal is divided by the total X-ray absorption (XAS) signal measured at the same edge. This corresponds to a normalization of the total magnetization to the coverage. Thus, the
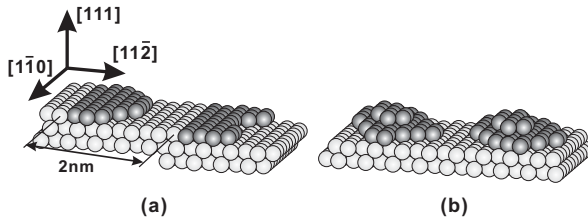
Figure 3.14 Sub-monolayer morphology of Fe (a) on Pt(997) and (b) on Pt(111) for θ_{Fe}= 0.5 ML. While on the vicinal surface an array of Fe stripes forms by step flow growth, on the flat surface 3D islands formation dominates the growth.
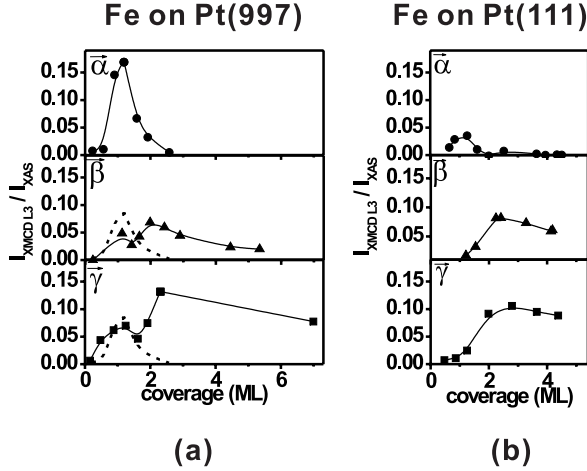
Figure 3.15 Remanent XMCD signal as a function of Fe coverage for Fe on Pt(997) (a) and Fe on Pt(111) (b) measured at 100 K in the three directions $\vec{\alpha}$ (along the surface normal), $\vec{\beta}$ (close to the in-plane, perpendicular to step direction for the case of Pt(997)), and $\vec{\gamma}$ (close to the in-plane, parallel to the step direction for the case of Pt(997)) which are defined in Fig.3.3. Dotted lines in $\vec{\beta}$ and $\vec{\gamma}$ directions in (a) corresponds to the projection of the perpendicular component onto the direction $\vec{\beta}$ and $\vec{\gamma}$.

value plotted in Fig.3.15 is proportional to the remanent magnetic moment per atom. The normalization allows a quantitative comparison of the magnetization of Fe along different directions and on different substrates. The assignment to the coverage is made using the calibration curve in Fig.3.5.

Fig.3.15 (a) shows the remanence of Fe on Pt(997) as a function of thickness measured along the three crystallographic directions perpendicular to the surface plane ($\overrightarrow{\alpha}$), in-plane along the steps ($\overrightarrow{\beta}$), and in-plane perpendicular to the steps ($\overrightarrow{\gamma}$). Below a coverage of 1.5 ML, a remanent magnetization perpendicular to the surface is found. With increasing thickness the magnetization reorients into the surface plane, as is concluded from a decreases of the polar signal and an increase of the in plane signal. Since the measurements along $\overrightarrow{\beta}$ and $\overrightarrow{\gamma}$ are made at an angle of 60° with respect to the surface normal, the magnetization observed in $\overrightarrow{\beta}$ and $\overrightarrow{\gamma}$ below 1.5 ML contains the projected signal from the perpendicular sample magnetization, $\mathbf{M_r} \cdot \cos 60°$. The reorientation from perpendicular to horizontal magnetization does not occur in a sharp transition but extends over a coverage range of 0.5 ML. This finite width cannot be ascribed to

the thickness resolution inherent in the measurements. It can thus be concluded that the magnetization gradually passes through a canted magnetic state. Above a coverage of 2 ML, no perpendicular remanent magnetization is observed. In this range the remanent magnetization is almost aligned with the step edge direction $\overrightarrow{\gamma}$. However, a component of $\mathbf{M_r}$ perpendicular to the step edges ($\overrightarrow{\beta}$ direction) which decreases with increasing coverage from 50 % to 25 % is found. Assuming a single-domain state, the magnetization direction thus adapts an angle changing from 27° to 13° with respect to the step edge direction.

Fig.3.15 (b) shows that the observed perpendicular remanent magnetization of Fe on Pt(111) is small in the studied coverage range in comparison to Fe on Pt(997). However, a remanent in-plane component develops at around 1.5 ML coverage and becomes comparable in magnitude to Fe on Pt(997). The observed remanence is slightly larger in $\overrightarrow{\gamma}$ direction than in $\overrightarrow{\beta}$ direction. The difference between these directions on Pt(111) corresponds only to a different high symmetry direction of the hexagonal surface layer and cannot be related to a step-induced anisotropy as in the case of Pt(997). As the azimuth of the sample cannot be rotated in the vacuum chamber, the measurements in $\overrightarrow{\beta}$ and $\overrightarrow{\gamma}$ directions were made on separately prepared Fe wedges, which may explain part of the observed small difference on Pt(111).

In summary a major difference between Fe on Pt(997) and Fe on Pt(111) is found in the magnitude of the remanent perpendicular magnetization. The remanent magnetization at its maximum slightly above 1 ML coverage is almost 5 times larger on Pt(997) than on Pt(111).

Fig.3.16 shows hysteresis loops measured by XMCD on the Fe L_3 edge along the three directions $\overrightarrow{\alpha}$, $\overrightarrow{\beta}$ and $\overrightarrow{\gamma}$. Typical loops are shown for the two regimes, *i.e.* below and above the spin reorientation transition. The Fe coverage is indicated for each magnetization curve. For 1 ML Fe on Pt(997) (Fig.3.16 (a)), the above conclusion is confirmed that the measurements in $\overrightarrow{\beta}$ and $\overrightarrow{\gamma}$ directions display the projections of the magnetization in direction $\overrightarrow{\alpha}$. As the magnetization at the highest available magnetic field is substantially lower for the in-plane directions, it is concluded that the available external field of 0.1 T is only sufficient to fully saturate the magnetization along the easy axis, $\overrightarrow{\alpha}$. The same argumentation applies equivalently for 2.5 ML on Pt(997) in Fig.3.16 (b): At higher coverage, saturation of the hysteresis loops in the surface plane is found. The significant difference in the shape of the magnetization curves in direction $\overrightarrow{\beta}$ and $\overrightarrow{\gamma}$ confirm the existence of an in-plane anisotropy on the vicinal surface. Maximum coercive fields on the Pt(997) substrate of 0.02 T to 0.03 T are found along the easy directions, with a slightly higher value for the low coverage regime.
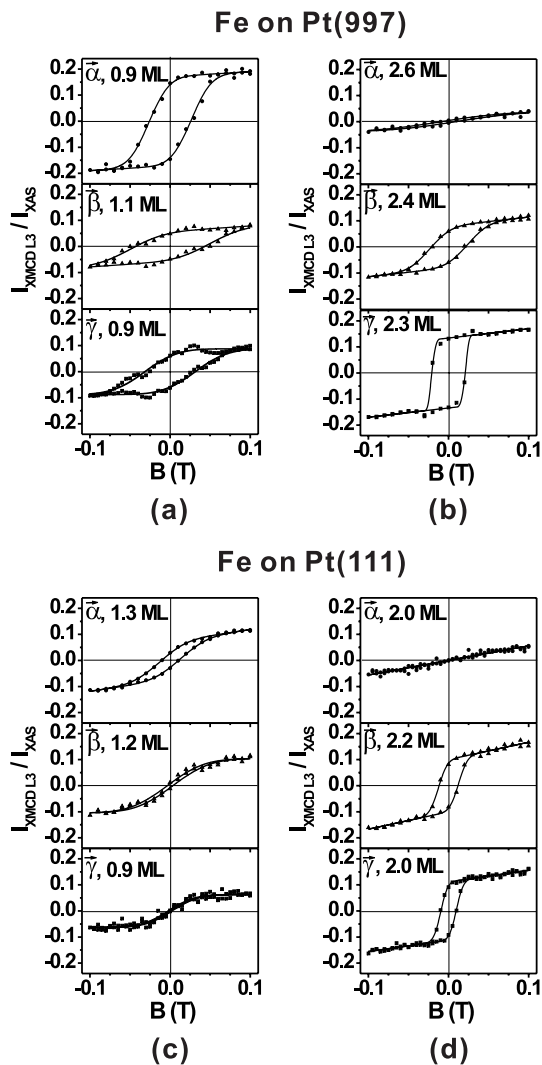
Figure 3.16 Hysteresis loops measured along the three directions $\vec{\alpha}$, $\vec{\beta}$, and $\vec{\gamma}$ at T=100 K in the two magnetization regimes (*i.e.* below and above the spin reorientation transition) for Fe on Pt(997) at the coverages (a) 1.0 ML and (b) 2.4 ML, and for Fe on Pt(111) at (c) 1.0 ML and (d) 2.0 ML. Solid lines are guides to the eye.

By comparing the data for the cases where the magnetization becomes saturated it is found that the observed magnetic moment per Fe atom is of similar size in both systems. However, for 1 ML Fe on Pt(111) a comparatively small polar remanence is found. Around 2 ML the maximum applied magnetic field is insufficient to obtain saturation of magnetization in perpendicular direction but the magnetization in the surface plane can be saturated by the available field. Again, due to the 30° angle between the directions $\overrightarrow{\beta}$ and $\overrightarrow{\gamma}$ and the surface plane, the slope at maximum magnetic field originates from the out-of-plane component and not from the in-plane magnetization loop. In contrast to the data for the vicinal surface almost identical magnetization curves in the $\overrightarrow{\beta}$ and $\overrightarrow{\gamma}$ directions are found and it is thus confirmed that there is no significant magnetic anisotropy within the surface plane.

It is known that the magnetic coupling in a thin Fe film can change fundamentally depending on its structure and atomic volume. For Fe on Cu(100) $e.g.$ it was found that an fcc phase with low atomic density exhibits ferromagnetic coupling between its layers while a high volume fcc phase becomes antiferromagnetic[160] . The results of the monolayer structure of Fe on Pt(111) and the vicinal surface suggest a qualitatively similar transition although at lower coverage. Pseudomorphic growth on the vicinal surface dilates the Fe lattice with respect to its bulk nearest neighbor distance. In contrast, on the flat Pt(111) surface the layer can more easily adapt a higher area density through the formation of dislocations. This change of lattice, nearest neighbor distance, and coordination may directly reduce the magnetic coupling between Fe atoms in the Fe islands. It may even be weakened further by an increased coverage in higher layers which would strongly reduce the magnetic moment for a possibly antiferromagnetic inter-layer coupling. Although only a small central area of each island exhibits double layer height (Fig.2.19) an antiferromagnetic coupling in these regions would significantly reduce the magnetic ordering within the film. Even though the detailed coupling in the Fe adislands is not known, the combination of lattice relaxation with 3D growth on Pt(111) may well explain the small remanence which is in contrast to the property of Fe/Pt(997) with pseudomorphic step-flow growth.

The experimental results show that the change of magnetization from the perpendicular direction to the in-plane direction occurs on the two different substrates almost at the same Fe coverage of about 1.8 ML. The morphology of the Fe adlayers on the two substrates is clearly different at the coverage when this transition occurs. The transition is thus affected mostly by the total coverage and less by the detailed island morphology and local coordination. If the reorientation would, for example, depend on the local island height we would expect the reorientation on Pt(111) to occur at lower coverage

than on Pt(997).

The observed change of magnetic properties with film thickness can be compared to the cases of Fe on Cu(100) and Cu(111). While the transition to antiferromagnetic coupling on Cu(100) due to a change between two fcc phases of different atomic volume is found at 2.5 ML Fe coverage for 110 K[161] the reorientation from perpendicular to in-plane magnetization which accompanies an fcc(111) to bcc(110) structural transition of Fe on Cu(111) is observed between 2.3 ML and 3 ML at 160 K[162] . It is worth noting that with respect to structure and lattice mismatch those systems are rather different from the ones discussed here. While bulk Cu has a nearest neighbor distance (**nnd**) of 2.55 Å and is thus similar to Fe with a **nnd** of 2.49 Å (mismatch -2 %), Pt has a **nnd** of 2.77 Å and is thus 11 % expanded with respect to Fe. A similarity of the systems is, however, that the bcc metal Fe is grown on fcc substrates.

As already pointed out above, the hysteresis curves in $\overrightarrow{\beta}$ and $\overrightarrow{\gamma}$ direction on Pt(111) are almost identical (Fig.3.16). In contrast, on Pt(997) there is a qualitative difference between the $\overrightarrow{\beta}$ direction and the more easily polarizable $\overrightarrow{\gamma}$ direction, parallel to the step edges. In this direction an almost square hysteresis loop is found. The regular step-terrace structure on Pt(997) breaks the terrace symmetry and makes the substrate highly anisotropic. As discussed earlier, this anisotropy is directly reflected in the anisotropy of the growing Fe adislands and an alignment of the growth fronts on the entire sample. After monolayer completion an island will begin to overgrow the substrate step edge. The height mismatch of the advancing Fe island and its substrate which is now formed by the first Fe layer covering the Pt terrace will introduce defects. This process leads to the eventual degradation of the layer-by-layer growth as observed in the He reflectivity data in Sec.2.2 when bulk defects in the film originate at the lines of the former substrate step-edges. However, the substrate anisotropy will be conserved during the continuing growth of the Fe film and it will still be reflected in the morphology even of thicker films. It is thus clear why only upon magnetic reorientation into the surface plane at 2 ML a strong in-plane anisotropy for thicker layers of Fe on Pt(997) is found: On Pt(111) such a step-induced anisotropic morphology does not exist and below 1.8 ML coverage the missing contribution from in-plane magnetism prohibits its observation.

In this section the structural and magnetic properties of atomically-thin Fe films grown at 300 K on Pt(111) and on Pt(997) were compared. Both systems show at 100 K a reorientation transition at 1.8 ML Fe coverage from a perpendicular easy magnetization axis to an easy axis in the surface plane. However, significant differences in the magnetic properties are observed: Fe on Pt(997) shows a substantially larger spontaneous magnetization at coverages around one monolayer with an easy axis perpendicular

to the surface. At Fe coverages above 2 ML a strong magnetic in-plane anisotropy is observed in contrast to the film deposited on Pt(111). The results indicate that the magnetic properties of the Fe adlayer are modified substantially by introducing a homogeneous and high step density. We suggest that the observed differences between the substrates are essentially due to the Fe adlayer structure and morphology: The increase of interatomic distance and the delayed on-set of growth in the second and third layers on the vicinal surface enhances spin blocking and increases the remanent magnetization.

3.2.2 Magnetism of atomic Fe chains

Results

As shown in section 2.2, the presence of substrate steps of the Pt(997) induces step-flow growth of Fe at substrate temperatures between 300 K and 350 K. Hence, during the initial growth impinging Fe atoms decorate the substrate steps, thus forming linear stripes of Fe atoms of a width depending on the Fe coverage. In this section, investigations of the magnetism of Fe stripes of varying width, from monatomic chains to a full pseudomorphic monolayer, by XMCD are presented.

Quasi-one-dimensional stripes of Fe were grown on the Pt(997) surface by depositing $\theta_{Fe} = 0.1 \cdots 1$ atomic layers of Fe. XAS and XMCD spectra were measured at $T =10$ K at the Fe $L_{2,3}$ absorption edge in the energy range of 695 eV $< E <$ 740 eV by RCP light. The external field **B** was provided by a superconducting magnet and was ramped between ± 3 T. Fig.3.17 (a) shows XAS spectra for 0.5 ML Fe on Pt(997) measured perpendicular to the surface at $T=10$ K for opposite orientation of the magnetic field. The corresponding XMCD spectrum is shown in Fig.3.17 (b). The presence of a dichroic signal at the Fe $L_{2,3}$ edges is the result of ferromagnetic ordering in the Fe chains.

The evolution of the magnetic anisotropy as a function of Fe stripe width was explored by recording hysteresis loops for stripes of one, three, and seven atoms in width. To record the loops the magnetic field was changed continuously at a rate of $d\mathbf{B}/dt \sim 12$ mT/s between $+3$ T and -3 T. The total acquisition time per loop was less than 17 minutes.
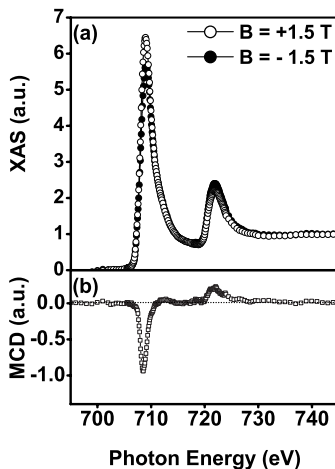
Figure 3.17 (a) XAS spectra measured in opposite magnetic fields $+1.5$ T and -1.5 T, and (b) XMCD spectrum for 4 atoms wide Fe stripes on Pt(997) taken at the Fe $L_{2,3}$ absorption edges by RCP light at $T =10$ K.

The hysteresis loops measured along three different directions $\overrightarrow{\alpha}$, $\overrightarrow{\beta}$, and $\overrightarrow{\gamma}$ as a function of Fe coverage are summarized in Fig.3.18. Fig.3.18 (a) shows characteristic magnetization loops for the monatomic chains ($\theta_{Fe} = 0.13$ ML), (b) for stripes of three atoms in width ($\theta_{Fe} = 0.38$ ML) and (c) for stripes of 7 atoms in width ($\theta_{Fe} = 0.88$ ML). For the monatomic chains in (a) one can see that the shape of the hysteresis loops along $\overrightarrow{\alpha}$ and $\overrightarrow{\beta}$ are similar, but different from the loop observed along $\overrightarrow{\gamma}$. The S-shape of these loops is more pronounced along $\overrightarrow{\alpha}$ and $\overrightarrow{\beta}$, in comparison to the loop obtained along $\overrightarrow{\gamma}$. In other words, for every value of $\mathbf{B}$ the observed magnetic signal is larger along $\overrightarrow{\alpha}$ and $\overrightarrow{\beta}$, than along $\overrightarrow{\gamma}$. It is concluded that the directions $\overrightarrow{\alpha}$ and $\overrightarrow{\beta}$ span a plane of preferred magnetization direction. Remanent magnetization is not observed in any direction for this coverage. The magnetic anisotropy of triatomic chains in Fig.3.18 (b) is found to be different from the monatomic chains. Here, the loop measured along the direction $\overrightarrow{\beta}$ exhibits the largest magnetization for any applied magnetic field, mak-
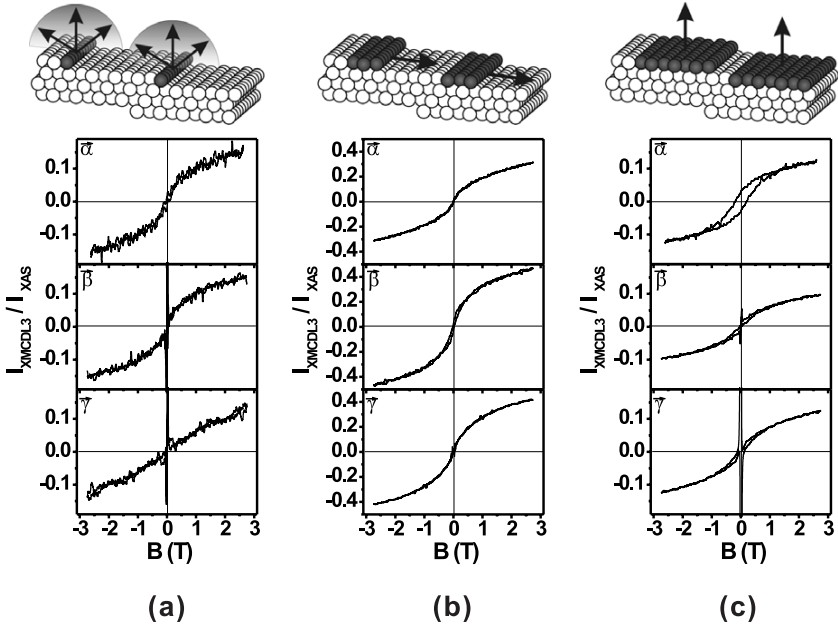

Figure 3.18 Hysteresis loops of Fe on Pt(997) with coverage (a) 1 row, (b) 3 rows, and (c) 7 rows measured at T = 10 K in three different directions defined in Fig.3.3. The observed easy axes are indicated by arrows in the schematic diagrams at the top of the figures.

ing it the easy magnetization axis. Interestingly, for the stripes of 7 atoms in width (Fig.3.18 (c)) the easy axis is again along the surface normal.

The experimental results can thus be summarized as follows: (i) the magnetic anisotropy oscillates between perpendicular and in-plane direction with increasing width of the Fe stripes, from monatomic chains to stripes of 7 atoms in width. (ii) The differences between easy and hard axis loops, which represents the magnetic anisotropy, is small. A more pronounced anisotropy was found for Co chains on Pt(997)[72], for instance.

The advantage of the measurements by circular dichroism is that the dichroic signal obtained during experiments contains information about the spin and the orbital momentum per atom, m_S and m_L, of the sample. To extract these information from the spectra, the application of the sum rules is necessary[146]. The absolute determination of m_S and m_L, however, requires the value of the dipole-operator, T_z. While the calculation show that T_z is negligible for nanostructures of Co, in the case of Fe the consideration of T_z is a significant correction. The T_z is a priori not known and has to be provided by theory. To circumvent this difficulty and to obtain first information about general trends of the magnetic moments, the ratio of $m_L/m_{S,eff}$ was deduced as a function of θ_{Fe} from the experimental data. This dependence is shown in Fig.3.19. The plotted values of $m_L/m_{S,eff}$ are obtained from measurements along the easy axes of the samples. With increasing Fe coverage the value $m_L/m_{S,eff}$ decreases until $\theta_{Fe} = 1.5$ ML. For higher coverage, the ratio increases again. In the observed coverage range $m_L/m_{S,eff}$ is always larger than 0.04 which is the value of bcc bulk Fe. Clearly, for ultralow coverage a strongly increased ratio $m_L/m_{S,eff}$ is observed. The $m_L/m_{S,eff}$ observed for monatomic chains is around 0.2, which is five times as large as that of one monolayer.

Calculation of the spin and orbital magnetic moments by the FLAPW method[163]
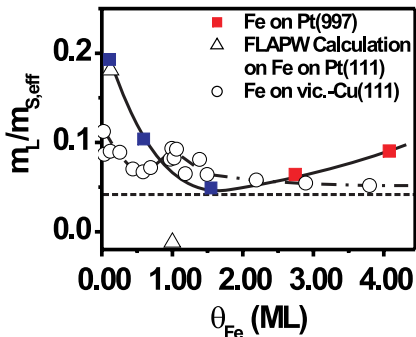

Figure 3.19 The ratio m_L/m_S of Fe on Pt(997) as function of thickness (filled squares). Results from the FLAPW calculation[163] and for Fe on the vicinal Cu(111) surface[164] are indicated by open circles and triangles, respectively. Solid and dash-dotted lines are guide to the eye. The value of m_L/m_S of bulk bcc Fe, 0.04, is indicated by the dashed line.

demonstrate that the spin moment remains almost constant for decreasing coverage, while the orbital moment increases due to a reduced local atomic coordination, thus gradually eliminating the effect of orbital moment quenching. Thus, the dependence of m_L/m_S is attributed to a pure thickness dependence of m_L alone. In other words, all features of Fig.3.19 can be interpreted as a dependence of the orbital magnetic moments on dimensionality. The found dependence of m_L/m_S is qualitatively reproduced by FLAPW calculations[163] : The value of the monatomic chains of 0.2 is in splendid agreement with theoretical predictions by FLAPW calculations. On the other hand, the calculated value for θ_{Fe}=1.0 ML is lower than the experimental value at this thickness, but the experimental data reproduce the predicted minimum of the moment-ratio at this thickness. When $m_{S,eff}$ for the monatomic chain and monolayer of Fe on Pt(111) is taken from the FLAPW calculation[163] , m_L for monatomic chain and monolayer is evaluated as 0.61 μ_B and 0.16 μ_B, respectively. This further supports the assumption of enhanced orbital magnetic moments of the 1D Fe monatomic chains in comparison to structures with higher dimensionality.

When experimental values of $m_L/m_{S,eff}$ for Fe on vicinal Cu(111)[164] is compared to the data of Fe on Pt(997) as in Fig.3.19, a difference between the two cases is found: for θ_{Fe} corresponding to single rows, $m_L/m_{S,eff}$ of Fe on vicinal Cu(111) shows a maximum value of around 0.11, which is around half of the maximum value of Fe on Pt(997). Furthermore, the dependence of $m_L/m_{S,eff}$ on θ_{Fe} does not show a pronounced minimum. The authors correlate the thickness dependence of $m_L/m_{S,eff}$ of Fe on vicinal Cu(111) with the structural transformation from pseudormorphic Fe to the incommensurate γ fcc Fe at $\theta_{Fe} \simeq$0.8 ML and to 1D to 2D percolation at $\theta_{Fe} \simeq$1.5 ML.[162, 164, 165] This structural change is not observed during the growth of Fe on Pt(997) at room temperature below $\theta_{Fe} \simeq$ 2 ML, which may explain qualitative differences between the two systems shown in Fig.3.19.

Discussion

The variation of the local coordination due to dimensionality change is expected to induce an anisotropy in the local crystal field. It has been shown in the ligand field model[166, 167] that even in the case of itinerant metallic system, the symmetry breaking can cause asymmetric charge distribution, and thus results in the enhanced MCA and m_L. This is particularly true for sub-monolayer structures, because the localization of the electrons becomes significant. The row-by-row wise change of the local coordination, as shown in Fig.3.20, can be linked to the observed MCA oscillation shown in Fig.3.18 and the strong enhancement of m_L for Fe atomic chains. The connection between local
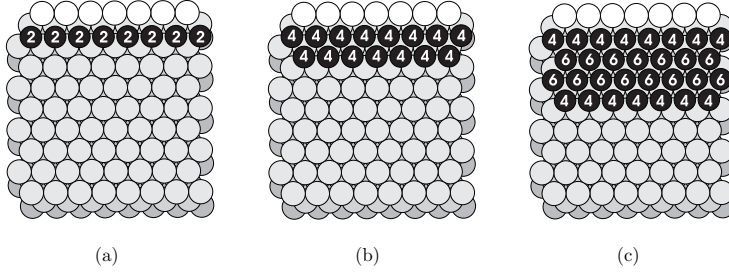
Figure 3.20 Change in the local coordinations when the coverage of Fe is (a) 1 row, (b) 2 rows, and (c) 4 rows on Pt(997). The numbers of nearest Fe neighbors in the Fe layer are indicated on the Fe atoms (black).

coordination and the MCA have been treated intensively in ligand-field model[166, 167] or Nèel's pair bonding model[168, 169] . Thus, an attempt will be made here to describe the experimental observation of oscillating anisotropy by employing both models. The pair bonding model is used here as an approximation, because of its simplicity and direct connection with N_{first}. Better results could be obtained by using the ligand-field model directly since it is based on first-principles calculation, but its application is time consuming and complex and beyond the scope of this thesis.

Since Néel's description of the relationship between crystal symmetry and magnetic anisotropy[168] , the pair-bonding model has successfully explained the dependence of magnetic anisotropy on the sample symmetry for several systems, such as ferromagnetic thin films on stepped surfaces[170, 171] . The local coordination at different atomic sites is incorporated in the anisotropy energy density E_{MCA}[172] . Recently, a complete formalism for cubic symmetry was developed by Skomski *et al.*[169, 173] with spherical harmonic expansion of the crystal field[174, 175] . By the use of the formalism in the calculation of E_{MCA}[169, 173] , changes of the local atomic coordination, as shown in Fig.3.20 can be taken into account for the description of the magnetic anisotropy.

The details of the calculation of E_{MCA} for an Fe overlayer on Pt(997) by the pair bonding model are described in Appendix.A. Pair-bonding is considered only in the Fe layer, hence the results presented here corresponds to the case of a free standing Fe layer whose crystal symmetry corresponds to the Pt(997) surface. It was shown that E_{MCA} can be expressed as[169] :

$$E_{MCA} = \frac{1}{2} \sum_{i \neq j} \sum_{l} a_l(r_{ij}) \cdot P_l(\cos \alpha_{ij}) \tag{3.34}$$

where the coefficient $a_l(r_{ij})$ originates from many body Coulomb interactions[174, 176] , $P_l(\cos \alpha_{ij})$ is the Legendre function, $\boldsymbol{r}_{ij}$ is the bond vector between atoms i and j, α_{ij} is the angle between $\boldsymbol{r}_{ij}$ and the direction of the magnetic moment. Eq.(3.34) can be transformed to

$$
\begin{aligned}
E_{MCA} =& \sum_l a_l \cdot \acute{\kappa}_l \cdot P_l(\cos \Theta) \\
&+ \sum_l \sum_{m=1}^l a_l \cdot \acute{\kappa}_{lm}^{(c)} \cdot P_m^l(\cos \Theta) \cdot \cos m\Phi \\
&+ \sum_l \sum_{m=1}^l a_l \cdot \acute{\kappa}_{lm}^{(s)} \cdot P_m^l(\cos \Theta) \cdot \sin m\Phi
\end{aligned}
\tag{3.35}
$$

where $\acute{\kappa}$ is the macroscopic anisotropy coefficient, Θ and Φ are the angles describing local symmetry (See Fig.A.1 in Appendix.A for the definition of Θ and Φ). Table.3.1 summarizes the variation of $\acute{\kappa}$ as a function of the width of Fe atomic chains and for atoms at the surface and at bulk sites for comparison. It is found that $\acute{\kappa}_{lm}$ of atoms in higher symmetry sites, such as bulk atoms, is close to zero. On the other hand,

Table 3.1 Macroscopic anisotropy coefficients $\acute{\kappa}$ from the first nearest neighbors at distance. Other terms not provided, such as $\acute{\kappa}_{62}^{\,s}$, are zero. Terms with order $l = 6$ are also given for completeness.

$\acute{\kappa}$	1 row	2 rows	4 rows	8 rows	surface	bulk
$\acute{\kappa}_2$	-1/2	-1	-5/4	-11/8	-3/4	0
$\acute{\kappa}_4$	3/8	3/4	15/16	33/3	41/48	7/12
$\acute{\kappa}_6$	-5/16	-5/8	-25/32	-55/64	-149/96	-13/6
$\acute{\kappa}_{22}^{\,c}$	1/4	1/8	1/16	1/32	0	0
$\acute{\kappa}_{42}^{\,c}$	-1/24	-1/48	-1/96	-1/192	0	0
$\acute{\kappa}_{43}^{\,s}$	0	0	0	0	$-\sqrt{2}/144$	$-\sqrt{2}/72$
$\acute{\kappa}_{44}^{\,c}$	1/192	1/384	1/768	1/1536	0	0
$\acute{\kappa}_{62}^{\,c}$	1/128	1/128	1/256	1/512	0	0
$\acute{\kappa}_{63}^{\,s}$	0	0	0	0	0	0
$\acute{\kappa}_{64}^{\,c}$	-1/1920	-1/3840	-1/7680	-1/15360	$-13\sqrt{2}/3456$	$-13\sqrt{2}/1728$
$\acute{\kappa}_{66}^{\,c}$	1/23040	1/11520	1/9216	11/92160	53/414720	13/103680

for atoms in sub-ML stripes, large values of $\acute{\kappa}_{lm}$ are found as a result of the reduced symmetry. Therefore, the E_{MCA} becomes increasingly dependent on the azimuthal angle Φ as the symmetry is broken by decreasing the coverage.

The parameters a_2 and a_4 can now be chosen such that best possible agreement between the experimental data and the model is achieved. With the choice of $a_2 = 1$ and $a_4 = -0.5$, and the values of $\acute{\kappa}$ from Table.3.1, the directional dependence of E_{MCA} can be estimated (Fig. 3.21). It is pointed out that this choice of a_2 and a_4 is not universal for all thicknesses, but each thickness both values are adjusted to get agreement with the experimental observation. Magnetic easy and hard directions correspond to the minima and maxima of E_{MCA}, respectively. It is clearly seen that E_{MCA} changes with the sample dimensionality. The degeneracy of the anisotropy in the $(1\bar{1}0)$ plane, as found in Fig.3.18(a), is reproduced by the result in Fig.3.21(a). For the double rows (Fig.3.21(b)), the global energy minimum becomes distinctive for magnetization along the [111] direction, with a local minimum perpendicular to the step edges *i.e.* in $[11\bar{2}]$ direction as a "leftover" from the degeneracy. With increasing coverage, the local minimum disappears, and only the global minimum remains in [111] direction as in Fig.3.21(c). The shape of Fig.3.21(c) remains the same for the coverage of 6 rows. For coverages higher than 7 rows, a degeneracy of local minima within the $(1\bar{1}0)$ plane appears with a global minimum in [111] direction (Fig.3.21(d)). This finding is in agreement with the measurements at $T = 100$ K of Fig.3.15 (Sec.3.2.1). Hence, with increasing coverage the symmetry axis of the anisotropy surface changes gradually from the wire axis to the film normal.

The results in Fig.3.21 show that the MCA of Fe stripes on Pt(997) are dependent on the local coordination. The estimate based on the Néel model reproduces the transition of the easy magnetization axis, from an easy plane for the monatomic chains to the polar direction for the monolayer. The oscillatory behavior of the anisotropy can
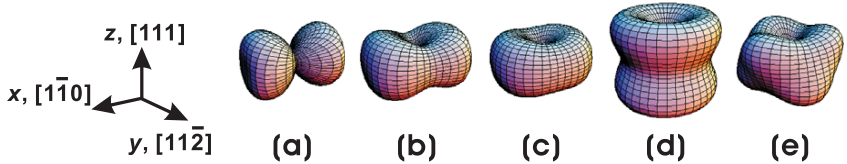
Figure 3.21 Change of the anisotropy energy E_{MCA} of Fe on Pt(997) calculated from Néel's pair bonding model for Fe coverage of (a) 1 row, (b) 2 rows, (c) 4 rows, (d) 8 rows (1 ML). For comparison, E_{MCA} of the surface atom is shown in (e).

not be reproduced. This disagreement between experiment and calculation points out, that important contributions to the anisotropy are not taken into consideration. The disregard of the underlying Pt substrate is most likely to be a too strong simplification. Calculations[163] , and also our measurements on Fe-Pt surface alloys presented in the next chapter show that Fe induces a magnetic moment also in the Pt. Even if the magnitude of the Pt magnetic moment is small, its role in determining the anisotropy of the system can be significant. This could be, for instance, the result of the coupling of the magnetic moments of Fe with those of Pt, thus influencing the Fe anisotropy with the large spin-orbit coupling of Pt.

Besides the magnetic anisotropy, also the m_L of the Fe stripes is sensitive to the variation of the local atomic coordination. It is important to note that the enhancement of m_L with decreasing coverage and the coverage-dependent anisotropy oscillation were also observed for Co chains on Pt(997)[11] . The symmetry considerations, as done for Fe in Fig. 3.21, also apply to the system Co on Pt(997) and again do not reproduce the experimentally found anisotropy oscillations. This disagreement underlines that besides the local atomic coordination also the electronic interaction with the substrate, such as the hybridization of the overlayer's $3d$ states with the $5d$ states of the Pt, may significantly contribute to the magnetic properties.

In summary, we measured the dependence of the magnetic anisotropy and the magnetic moment of Fe stripes of one atom in height and of varying width. The most striking results are (1) the oscillatory behavior of the magnetic anisotropy oscillates as a function of stripe width, and (2) the increase of the orbital moment with decreasing stripe width. The increase of m_L is ascribed to a decrease of the coordination of each individual Fe atom in the stripes with decreasing coverage. The correct description of the anisotropy by a Nèel model also based on the coordination fails, suggesting that the electronic interaction with the substrate provides a significant contribution to the anisotropy. This effect is discussed in more detail on the example of Fe-Pt surface alloys in the following section.

3.2.3   Magnetism of an Fe-Pt monolayer alloy on Pt(997)

An intriguing way to study the interaction of Fe atoms of monatomic chains with the Pt step atoms in more detail is to embed such chains into a 'sea' of Pt atoms. Such a model structure is achieved by forming a linear FePt surface alloy, described in Sec.2.2. An ordered Fe-Pt alloy confined at the top-most layer can be formed on Pt(997) during growth of Fe on Pt in a narrow substrate temperature range between 450 K and 550 K. Fig.3.22 shows schematically the idealized $Fe_{50}Pt_{50}$ surface alloy structure composed of Fe monatomic chains separated by Pt monatomic chains. In comparison to stripes of 0.5 ML Fe on Pt(997), the symmetry of the Fe atoms within the alloy is reduced. Within the top-most layer, the number of the first nearest Fe neighbors (N_{first}) in the Fe sublattice is 2 which is much less than the coordination of 6 for atoms in the stripes (See Fig.3.20). A significant modification in the electronic structures of both Fe and Pt atoms are expected as a result of alloying between Fe and Pt. It will be shown in this chapter that the alloying produces a strongly ordered perpendicular magnetization in the surface alloy with an enhanced total magnetic moment per atom.

The Fe-Pt surface alloy was prepared as described in Sec.2.2. The magnetism of the alloy layer was again measured by XMCD. Information on the magnetism of Fe and Pt were obtained independently by using the appropriate Fe and Pt absorption edges. The dichroism of Fe was measured at the Fe $L_{2,3}$ edges. The magnetic moment of Pt is a result of the exchange splitting of the $5d$ band[179,180] . Hence, for XMCD measurements the $N_{6,7}$ absorption edges probing the transition $4f \rightarrow 5d$ have been chosen. Other absorption edges, such as $L_{2,3}$, $M_{2,3}$, $N_{2,3}$ were not accessible with the monochromator or energetically overlap with absorption edges of deposits on the beamline optics. The mass absorption coefficients for Fe and Pt in the energy range between 60 eV and
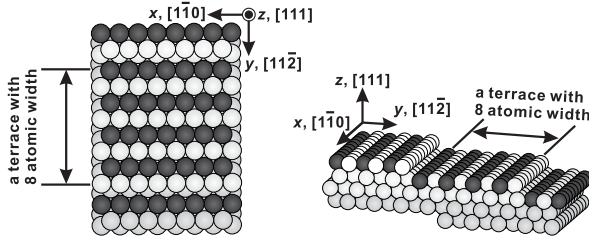
Figure 3.22 Top and perspective view of the anticipated $Fe_{50}Pt_{50}$ surface confined alloy formed on Pt(997) surface. Fe and Pt atoms are indicated as yellow and blue circles respectively. For detail information of the structure, see Sec.2.2
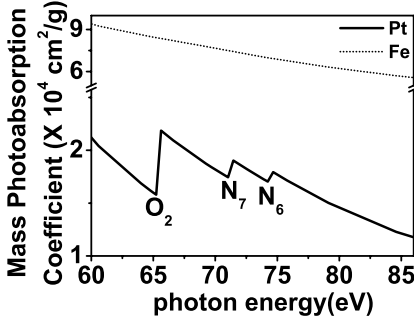
Figure 3.23 Mass photoabsorption coefficients of bulk Pt (solid line) and Fe (dotted line) in the energy range between 60 eV and 86 eV[177,178].

86 eV are shown in Fig.3.23[177,178]. In this energy range the Pt O_2 and $N_{6,7}$ absorption edges are located, while Fe does not show any absorption edges here. The $N_{6,7}$ edges correspond to electronic transitions from the $4f_{5/2,7/2}$ spin-orbit split core shell to the $5d$ band at the Fermi level and thus are sensitive to exchange splitting at the Fermi energy. For the investigation of the magnetic moment of Pt the magnetization dependence of the absorption at the $N_{6,7}$ edges has been probed by varying the photon energy within the energy range 60 eV < E < 86 eV. All measurements were done at T=10 K with a maximum magnetic field of ±2.7 T and RCP light. Hysteresis loops of Fe were measured at the L_3 edge with E_{pre} =704.5 eV, E_{L_3} =708.25 eV. Hysteresis loops of Pt were measured at the N_7 edge with E_{pre} =68.0 eV, E_{N_7} =72.0 eV.

In Fig.3.24 the XAS and XMCD spectra recorded on 1 ML $Fe_{50}Pt_{50}$ surface alloy with magnetic fields of ±1.0 T are shown in comparison to the spectra of 0.5 ML Fe stripes. Most strikingly, resonance peaks of the XMCD spectrum of the surface alloy are 4.6 times larger than those of the pure Fe layer. This means that at the applied magnetic field the Fe magnetization of the alloy is substantially larger than that of the stripes. The enhanced magnetization is interpreted in detail in the next paragraph as the result of an increased magnetic ordering in the alloy, provided by indirect exchange interaction through the Pt.

For Fe in the Fe-Pt alloy and the stripes, Fig. 3.25(a) compares the XAS obtained by averaging of spectra for opposite magnetic fields, which corresponds to the XAS from the unmagnetized sample: It becomes clear that the absorption probability is identical for both systems. Minor differences in the absorption characteristics are found in the energy ranges marked by A and B, which might be the result of changes in the electronic structure of Fe in the alloy with respect to pure Fe. The corresponding XMCD spectra for both systems are shown in Fig. 3.25(b). Here, the XMCD spectra of the Fe stripes have been multiplied by a factor of 4.6. Except for the different
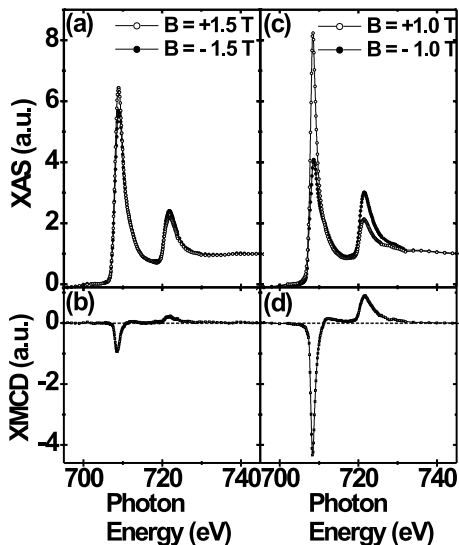
Figure 3.24 XAS (top) and XMCD (bottom) spectra at the Fe $L_{2,3}$ absorption edges: Comparison between 0.5 ML pure Fe layer ((a) and (b)) and FePt surface alloy ((c) and (d)) measured perpendicular to the surface at T=10 K.
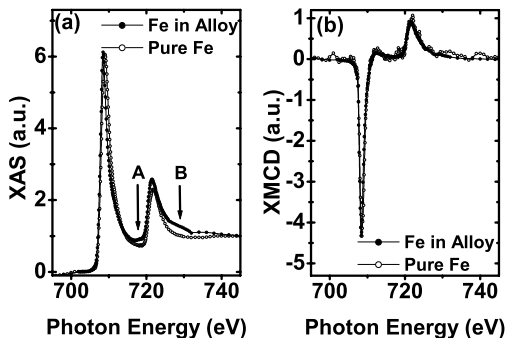

Figure 3.25 (a) Averaged XAS of the pure Fe stripes and the Fe-Pt surface alloy, and (b) XMCD of the two cases. For comparison, the XMCD spectrum (b) of the Fe stripes is multiplied by 4.6.

magnitude, the line shape of both XMCD spectra are identical. The comparison thus shows that the increased XMCD of Fe in the alloy is not the result of an enhanced absorption probability but related to an enhanced net magnetization of Fe.

Fig.3.26 shows hysteresis loops for Fe-Pt surface alloys with 0.5 ML (a) and 0.35 ML Fe (b) and a 0.5 ML pure Fe stripes (c) on Pt(997). All curves are measured perpendicular to the surface (approximately in [111] direction) at 10 K. For the alloy containing 0.5 ML Fe (Fig.3.26 (a)) the magnetization at maximum applied field of ±2.5 T is 4.6 times larger than that of the Fe stripes (Fig.3.26 (c)), as the result of the larger XMCD at the L_3 absorption edge shown in Fig.3.24. On the other hand, the hysteresis loop of the Fe-Pt surface alloy containing 0.35 ML Fe (Fig.3.26 (b)) shows a magnetization comparable to the pure 0.5 ML Fe stripes.

The shapes of the hysteresis loops reveal information of the magnetization reversal process. The loop of a 0.5 ML surface alloy in Fig.3.26 (a) shows saturated magnetization at a field of 0.8 T. The shape of the loop is almost square and the coercive field is found to be $\mathbf{B}_c = 0.58$ T. In contrast, the samples studied in (b) and (c) show 'S'-shaped magnetization loops.

The found magnitude of $\mathbf{B}_c =0.58$ T of 0.5 ML Fe in the surface alloy appears to be large in comparison to many monolayer thin film systems. Fig.3.27 plots the values
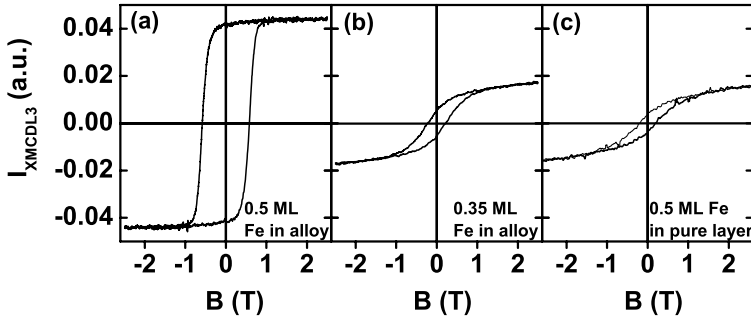
Figure 3.26 Hysteresis loops measured at the Fe L_3 edge for the Fe-Pt surface alloy on Pt(997) at T=10 K in [111] direction for (a) 0.5 ML and (b) 0.35 ML Fe coverage. The hysteresis loop for the 0.5 ML pure Fe stripes on Pt(997) at the same conditions is shown in (c).
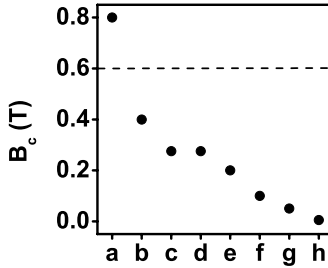
Figure 3.27 Comparison of the coercive field $\mathbf{B}_c$ for various FePt alloy thin films. **a** is the value for the 5000 Å FePt film on Si(001)[181] ; **b** for the chemically self-assembled 315 Å thick FePt nanoparticles[36] ; **c** for the 30 Å FePt film on MgO prepared at 375 °C[182] ; **d** and **e** for the 830 Å FePt (011) film and 1000 Å FePt (100) film on MgO[183, 184] ; **f** for the 30 Å FePt film on MgO prepared at 300 °C[182] ; **g** for the 2000 Å FePt film on the oxide Si wafer[185] ; **h** for the 3 Å Fe/Pt bilayer on MgO(001)[186] . All the data points were obtained at room temperature. Dashed line indicates $\mathbf{B}_c$ of FePt surface alloy in this thesis, which was measure at 10 K.

for various FePt thin films. If is found that only the 5000 Å FePt film on Si(001) (data point of **a**) has larger coercivity than that of this thesis. A magnetization reversal by domain wall propagation via a multidomain state usually requires much smaller coercive fields. Hence, rather a magnetization reversal by coherent rotation, as typically found for small Stoner-Wohlfarth particles exhibiting a single domain state[55, 122] , can be assumed also for the surface alloy. Under this assumption of coherent rotation of the magnetization during reversal, the activation barrier for magnetization reversal is proportional to the coercive field. Thus the comparison in Fig.3.27 shows that the FePt surface alloy prepared in this thesis exhibits enhanced activation barrier for magnetization reversal in comparison to the other cases.

The element specificity of the XMCD allows not only to investigate the magnetism of Fe, but also to analyze induced magnetic moments in the underlying Pt substrate. The magnetism of the Pt will hence be discussed in the following. Fig.3.28 shows (a) XAS and (b) XMCD spectra taken at the Pt $N_{6,7}$ edges. Clearly, dichroism is observed also for the Pt, with a maximum at $E = 72.0$ eV. This dichroic signal can only be understood by assumption of an induced magnetic moment in Pt as a result of the interaction with Fe atoms.

Several interesting features of the XAS and XMCD spectra are noticed: The overall

(a)   (b)
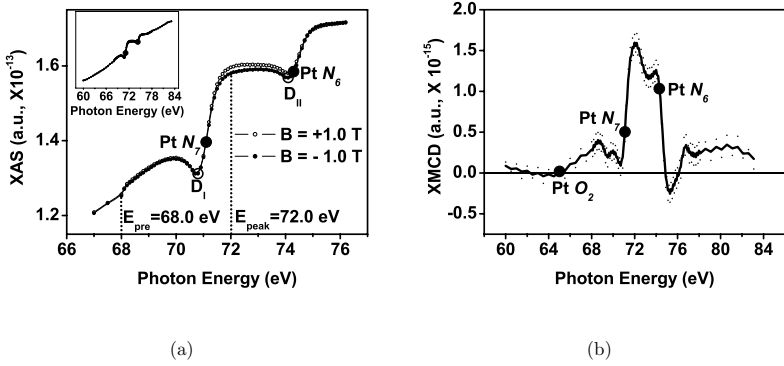
Figure 3.28 (a) XAS spectra for magnetic fields of $+1$ T and -1 T and (b) XMCD spectrum at the Pt $N_{6,7}$ edges for the Fe-Pt surface alloy layer measured at $T=10$ K. The inset in (a) shows the XAS spectra over an extended photon energy range. Filled circles indicate the Pt $N_{6,7}$ absorption edges reported for bulk Pt[177,178] . Open circles ($\mathbf{D_I}$ and $\mathbf{D_{II}}$) indicate characteristic points discussed in the text. The photon energies chosen to measure XMCD signal and pre-edge intensity for the hysteresis loops are indicated as E_{pre} and E_{peak}, respectively.

peak shape around the Pt $N_{6,7}$ edges does not correspond to the peak shape of an absorption spectrum of $e.g.$ Fe $L_{2,3}$ edges. Rather, two dips indicated as $\mathbf{D_I}$ and $\mathbf{D_{II}}$ are shown in Fig.3.28 (a). As a result, also the dichroic signal of the Pt N_7 and N_6 edges are not well separated. This peculiar peak shape was discussed in the literature as the result of a Fano resonance[142,187,188] . The Pt $N_{6,7}$ edges originate from the transitions from the initial $4f_{5/2,7/2}$ (l=3) state to the final $5d$ (l=2) or $5g$ (l=4) states. But because the Pt $5p$ core level lies between the $4f$ level and the $5d$ continuum at the Fermi level, $5p$ photo emission takes place in the photon energy range of the Pt $N_{6,7}$ edges (Fano effect). Theoretical calculations[142] show that the strong coupling between absorption and photo-emission results in asymmetric Fano line shapes, as seen in Fig.3.28 ($\mathbf{D_I}$ and $\mathbf{D_{II}}$).

Such an interference with photo-emission is not taken into consideration in the derivation of the sum-rule and the two step model of dichroism (see Sec.3.1.1) cannot be applied to obtain the induced magnetic moments of Pt. Hence, the magnetic moments and the alignment of the Pt moment with respect to the Fe moment can not $ad\ hoc$ be determined. A more detailed analysis[142] is required. However, the coupling between the magnetic moments of Fe and Pt can be determined from the comparison

with previous measurements on the bulk Co-Pt and Fe-Pt alloys. The dichroic signal $\mu_+ - \mu_-$ between the point "**Pt** N_7" and "**Pt** N_6" in Fig.3.28 (b) is positive, while the dichroic signal at the Fe L_3 edge in Fig.3.25 is also positive for the same photon helicity RCP. Exactly the same relation was found for bulk Co-Pt and Fe-Pt alloys[140, 142, 187, 188] which are known to exhibit parallel spin alignment between Fe/Co and the Pt. Based on this comparison between the FePt alloy investigated here and the XMCD published for the bulk samples, it is concluded that the magnetic moments of Fe and Pt are aligned parallel in the monolayer alloy.

The magnetic anisotropy of the FePt alloy layer was investigated by recording magnetization loops as a function of crystallographic direction. Fig.3.29 summarizes hysteresis loops measured at the Fe L_3 edge and at the Pt edge at E =72.0 eV in the directions $\overrightarrow{\alpha}$, $\overrightarrow{\beta}$, and $\overrightarrow{\gamma}$ as defined in Fig.3.3. Again, artifacts at around $\mathbf{B} = 0$ have been removed from the plots. From the directional dependence of the hysteresis loops of Fe (top row in Fig.3.29), it is clear that the direction along the surface normal corresponds to the easy magnetization direction. In contrast, no significant anisotropy between both in-plane directions β and γ is found. The latter result is quite surprising since the symmetry of the atomic structure of the alloy is expected to be clearly influenced by the substrate steps.
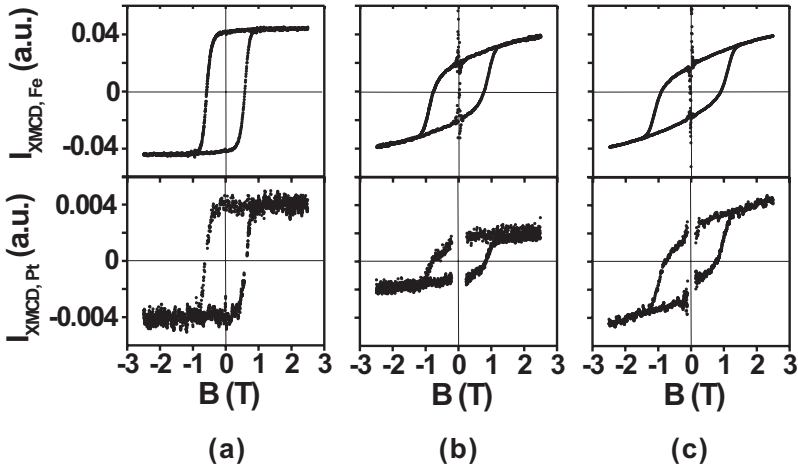
Figure 3.29 Hysteresis loops measured at the Fe L_3 (top row) edge and on the Pt edge at 72 eV (bottom row) in (a) $\vec{\alpha}$, (b) $\vec{\beta}$, and (c) $\vec{\gamma}$ directions at T=10 K.

The hysteresis loops of Pt (bottom row in Fig.3.29), can easily be scaled to match the shape of the Fe loops. Thus, these loops are in agreement with the assumption of collinear alignment of Fe and Pt magnetic moments. The induced magnetic moment in Pt (Fig.3.28) and its the collinear coupling to the magnetization of Fe (Fig.3.29) can be interpreted as the result of hybridization between Fe and Pt. Such a hybridization and the formation of common electronic bands may result also in deviations of the absorption spectra from those of pure Fe, as evident from in Fig. 3.25 (a). It is found that (1) There are differences of the positions of the L_3 and L_2 resonances by 0.5 eV and 0.3 eV, respectively. (2) At the energies marked as A and B, the XAS of the surface alloy exhibits a larger signal than the pure Fe layer. The hybridization between Fe $3d$ and Pt $5d$ bands can cause a strong modification in the wave-function of the $3d$ sub-band. Because XAS at the $L_{2,3}$ edges strongly depends on the final state wave-function, which are the $3d$ states for the case of Fe, both the positions of the $L_{2,3}$ resonance peaks and the shape of the XAS spectrum can be different for the Fe-Pt surface alloy and the pure Fe layer. For a better understanding, a theoretical study of XMCD spectra taking the *ab initio* calculated band structure of FePt surface alloy into account, is required and might be stimulated by these experimental findings.

It is pointed out here that the hysteresis loop of 0.5 ML stripes of pure Fe on Pt(997) is not saturated at an external field of 2.7 T (Fig.3.26 (b)). Thus, a comparison of deduced magnetic moments for Fe stripes and the alloy is not possible. Preliminary result show that even magnetic field higher than 6 T are not sufficient to magnetically saturate 0.5 ML Fe stripes on Pt(997). However, at such high field the observed XMCD signal becomes comparable to the spectra measured for FePt surface alloy. Under the assumption that spin magnetic moment does not change significantly with respect to the different chemical environment, one can conclude that total magnetic moments of 0.5 ML Fe in the Fe-Pt alloy and pure Fe layer on Pt(997) are similar to each other. The difference of the increased magnetization observed in Fig.3.24 (d) is rather understood as the result of a partly disordered spin alignment within the Fe stripes. Based on the high saturation fields required for the Fe stripes, an antiferromagnetic spin alignment between neighboring Fe stripes due to dipolar interaction is excluded. Rather, the magnetization within each stripe is not ordered, maybe as the result of superparamagnetism at the measurement temperature of 10 K with a spin block size smaller than the size of the stripes. The magnetization of the stripes is diminished by thermal agitation of the spin blocks. In such a picture, the large magnetization in the FePt surface alloy is interpreted as ordered magnetization in this layer provided by the indirect exchange interaction between the Fe rows through the Pt atoms. Here, the

surface alloy rather acts as a complete entity that is ferromagnetic at 10 K.

In summary, the magnetization of a monolayer of FePt surface alloy is found significantly larger than of the same amount of Fe deposited as non-alloyed stripes. This large magnetization is tentatively ascribed to an ordered magnetization in the FePt alloy due to indirect exchange coupling through the Pt versus the small magnetic moment in the Fe stripes reduced by thermal agitation. As a result of the alloying and the indirect exchange the Pt is found to exhibit a magnetic moment which is collinearly coupled to the magnetic moment of Fe. The Fe-Pt surface alloy shows a pronounced magnetic anisotropy with the easy axis perpendicular to the surface. To obtain exact magnetic moments of Fe and Pt atoms in the surface alloy, a more detailed analysis is required including first principles determination of the number of holes, the transition matrix of Fe, and fitting of the MCD spectrum at the Pt $N_{6,7}$ edges under consideration of Fano resonance effects.

3.3 MOKE Study on the magnetism of Fe on Pt(111)

In the previous sections, investigations of the magnetization of Fe on Pt by XMCD have been introduced. Despite the advantages of XMCD the experiments require synchrotron radiation which is only available if experiments are performed at the respective synchrotron facility. However, the results of the XMCD experiments can be supported by complementary measurements of the magneto-optical Kerr effect. This technique is comparatively easy to use and requires laser diodes as light source. Due to its sensitivity, magnetic measurements can be done for Fe coverage $\theta_{Fe} \geq 1$ ML. The sensitivity to in-plane and polar magnetization can be adjusted by varying the angle of incidence of the laser light.

MOKE magnetization loops have been recorded on Fe/Pt(111) as a function of Fe thickness on Fe wedges, in analogy to the XMCD experiments in Chap. 3.2. The remanent magnetization determined from these loops at T =100 K in polar and longitudinal geometry is shown in Fig.3.30. For θ_{Fe} <2.0 ML, we find perpendicular magnetization. Above θ_{Fe} >2.0 ML, in-plane magnetization is found. The critical coverage θ_{Fe} =2.0 ML shown in Fig.3.30 is in very good agreement with the spin reorientation transition found by XMCD study of Fig.3.15 (b) (see Sec.3.2.1). This result is particularly satisfying since it shows that the found magnetic phases can be reproduced independently on different substrates prepared in different UHV chambers.
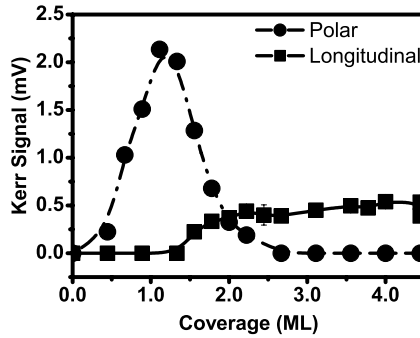
Figure 3.30 Remanent magnetization of Fe on Pt(111) as a function of coverage determined from the hysteresis loops measured at T=100 K in polar and longitudinal MOKE geometry. Plane of incidence of the light and H was parallel to the step edges in longitudinal geometry.

A comparison of the polar MOKE signal with the XMCD data in Fig.3.15 (b) suggests a more pronounced polar magnetization when measured with MOKE signal. It is noted that the MOKE signal does not allow to determine magnetic moments quantitatively. The Kerr intensity depends sensitively on the angle of incidence, the wavelength of the laser light and on the direction of the magnetization, making a quantitative evaluation very complex. In particular, for a given magnetic moment of the sample the magnitude of the Kerr signal is found to be more than an order of magnitude larger for polar MOKE compared to longitudinal MOKE[121,189] .

Fig.3.31 shows the hysteresis loops measured by the (a) polar and (b) longitudinal MOKE geometry for different coverage of Fe on Pt(111). All loops have been measured at $T = 100$ K. One can see that below 2 ML only perpendicular magnetization can be found. With the magnetic field available the sample could not be magnetically saturated. The loop shown for 1.3 ML Fe represents a minor magnetization loop.

(a)   (b)
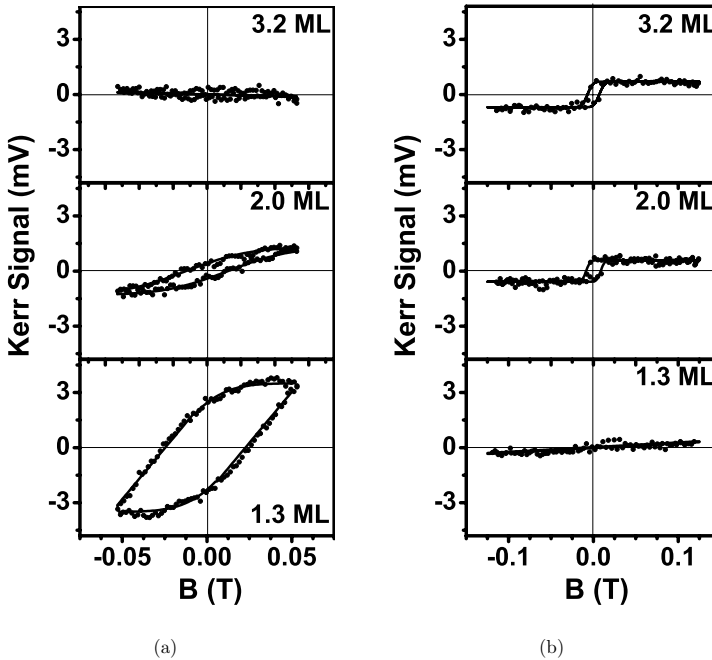
Figure 3.31 Hysteresis loops for 1.3, 2.0, and 3.2 ML of Fe on Pt(111) measured at T = 100 K for (a) polar and (b) longitudinal MOKE geometry. Plane of incidence of the light and **B** was parallel to [111] direction in longitudinal geometry.

In contrary, for higher coverage of 3.2 ML Fe, only in-plane magnetization loops are found by longitudinal MOKE. In this geometry a much stronger field is available and saturation of the magnetization loops was possible. For a critical Fe coverage around 2 ML, both polar and in-plane loops could be detected, in agreement with the assumption of a spin reorientation via canted state.

The results of this MOKE investigation clearly are in agreement of the results found by XMCD. Polar magnetization has been found for Fe on Pt(111) below the critical Fe coverage of 2.0 ML. Above 2.0 ML in-plane magnetization with only little directional dependence is found. The pronounced polar Kerr signal is due to the particular sensitivity of MOKE to polar magnetization. The measurements can not separate between contributions from the Fe and the Pt. Thus, any magnetic moment that might arise from the Pt is incorporated in the integral MOKE signal. However, this induced moment is predicted to be small if there is no alloying[163] .

3.4   In a nutshell: magnetism of Fe on Pt(997) from monatomic chains to monolayers

In this thesis the dependence of the magnetism on the atomic configuration of Fe structures has been investigated. The focus of the work was to explore the influence of atomic coordination on one hand and electronic interaction with the substrate on the other hand on the magnetism of the Fe structures. The evolution of the magnetic anisotropy and the magnetic moment of the structures were studied in detail since those properties are expected to be particularly sensitive to the sample dimensionality.

Different Fe nanostructures have been fabricated under ultrahigh vacuum condition by slight variation of the substrate orientation, the growth temperature and the Fe coverage. The resulting structures studied here are summarized in Fig. 3.32. With decreasing Fe coverage the local atomic coordination was diminished. At the same time, the increased Fe-Pt coordination of the Fe atoms at the Pt substrate steps becomes more influential on the Fe stripes. Hence, a particularly intriguing way to study the influence of the Pt on Fe is to form an FePt surface alloy which, metaphorically speaking, represents monatomic Fe chains embedded into the Pt surface with increased coordination of Fe atoms to Pt.

The presented results show that the magnetism of Fe nanostructures sensitively depends on the local atomic arrangement and its electronic interaction with the underlying substrate. These findings are results of the balance between the complex nature of the
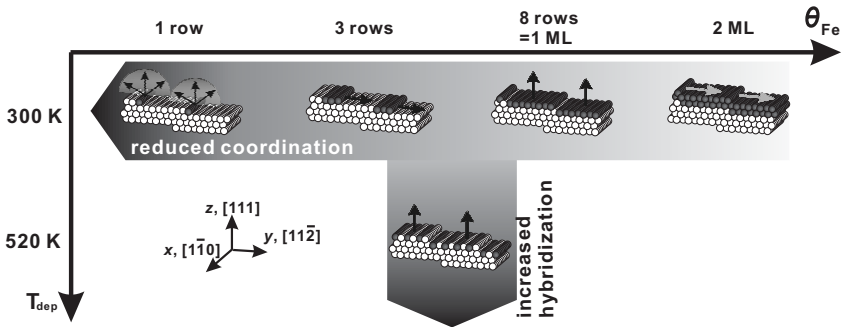

Figure 3.32 Magnetic phase diagram of Fe on Pt(997) as a function of Fe configuration, achieved by varying coverage (θ_{Fe}) and preparation temperature (T_{dep}). The observed easy axes in each case are indicated by arrows.

exchange interaction of the Fe, the influence of the ligand field on local magnetic moments and the dependence of magnetic moments on the local density of states at the Fermi energy. The results of the magnetic investigation can be summarized as follows: (1) The magnetic anisotropy of Fe stripes on Pt(997) is small, but the easy direction changes with increasing coverage row by row. (2) The remanent magnetization of the Fe stripes and one Fe monolayer on Pt(997) is small in comparison to the saturation value. To obtain magnetic saturation, external fields of more than 6 T are required. (3) In contrast, for FePt surface alloys saturation can be achieved at 0.6 T. For these samples induced magnetism in the Pt substrate is found. (4) Fe on Pt(111) forms compact islands. Here, a comparatively simple dependence of the magnetism on the Fe coverage is found with a spin reorientation from perpendicular to in-plane at the critical thickness of 2 ML. (5) The orbital magnetic moment per Fe atom increases with decreasing coordination.

The dependence of the orbital magnetic moment on the atomic configuration becomes obvious by comparing the intensity of the XMCD spectra of different samples, as shown in Fig. 3.33. The spectra are normalized to the L_2 edge. Thus, the height of the L_3 edge can, as was discussed previously, be taken as a measure for the orbital moment of the sample, provided that the number of d-holes is identical for each sample. If the 4 ML thin film is taken as bulk reference, one can see that in all sub-monolayer structures the orbital moment is enhanced with respect to bulk. Largest m_L is found for the monatomic Fe chains. The m_L found for the FePt alloy is similar to the m_L of the 0.5 ML Fe stripes only if the stripes are magnetically saturated by fields larger than 6 T.

The interesting result is that without external field the net magnetization for 0.5 ML Fe stripes along the surface normal is small compared to bulk, but applying a strong magnetic field significantly increases the observed moments. Such a behavior can be understood as the result of disordered magnetization at $\mathbf{B} = 0$ at the measurement temperature of 10 K. The possibility of opposite magnetization between adjacent stripes due to dipolar interaction is excluded based on the high field strength required to provide magnetic ordering. Rather, the magnetic disorder could be the result of superparamagnetism of stripes which are subdivided in spin blocks. In this case, the external field has to counteract the destructive effect of thermal agitation of the moments. In such a picture, the role of the Pt in the surface alloy could be to provide magnetic ordering by allowing indirect exchange between adjacent Fe rows. Here, the FePt surface layer acts as a whole entity versus the uncoupled action of the Fe stripes. The increase of the orbital moment and the coverage dependence of the magnetic anisotropy are, on the
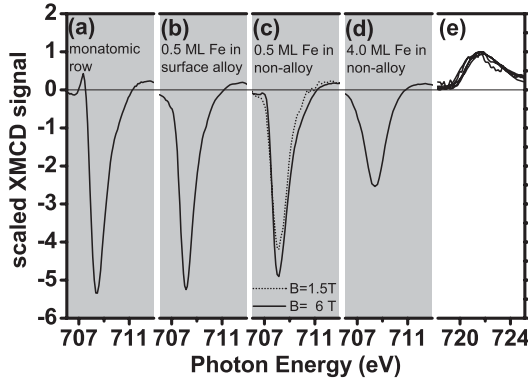
Figure 3.33 XMCD spectra at the Fe L_3 edge, normalized to the L_2 edge, of (a) 0.13 ML or monatomic row, (b) 1 ML $Fe_{50}Pt_{50}$ surface alloy, (c) 0.5 ML Fe stripe with $\mathbf{B} = 1.5$ T (dotted line) and $\mathbf{B} = 6$ T, and (d) 4.0 ML Fe film on Pt(997). The spectra are taken along the easy magnetization axis found for each sample.

other hand, direct results of the decreased atomic coordination.

It is revealing to compare the results found for Fe with the findings for Co on Pt. Both systems exhibit interesting similarities. For Co chains a characteristic oscillatory magnetic anisotropy with increasing Co coverage has been observed[11] . The magnetic anisotropy energy was found to increase together with the orbital magnetic moment, as the Co coverage decreases. The close relationship between preferred magnetization direction and orbital momentum as a result of the interaction of the magnetic moment with the ligand field was manifested on this example for nanostructures. Differences between Fe and Co stripes are thus more of quantitative than of qualitative nature. This result may surprise since Fe is expected to be more sensitive to structural modifications due to its quite complex exchange interaction and its sensitivity to minute structural modifications found in numerous experiments. However, the similarity might suggest that the element specificities are dwarfed by the interaction of the magnetic structures with the Pt substrate. It appears conceivable that the magnetic moment of the Fe or Co couples to the induced moment found in the Pt, as was actually found for the FePt alloy. In such a picture, the adlayer/substrate surface system acts as a magnetic entity with the strong spin-orbit coupling of the *substrate* governing the magnetic anisotropy.

In summary, the experimental evidence presented in this thesis points out the im-

portance of the local atomic symmetry, the coordination and in particular the inter-action with the substrate material for the magnetism of nanostructures. The role of the nanostructure shape, as is often discussed in terms of a shape anisotropy due to magnetostatics, appears to be of secondary importance.

Chapter 4

Conclusion

This study demonstrates that magnetic properties of the metallic nanostructures are sensitive to chemical ordering, local symmetry and coordination, and the degree of interface hybridization. The vicinal Pt(997) surface was employed to control systematically the local symmetry and coordination of Fe overlayers.

In contrast to Pt(111), the high density of steps on the vicinal Pt(997) surface allows to control morphology and local lattice symmetry of the adlayers, through adsorption site energy and growth kinetics: Fe on Pt(997) forms structures from monatomic chains to pseudomorphic layers at room temperature for coverages less than 1.0 ML, but Fe on Pt(111) shows 3D island growth with a bcc symmetry. Furthermore, surface alloying between Fe and Pt atoms is facilitated at the steps of Pt(997), as a result the alloying occurs at much lower temperatures than on the Pt(111) surface.

Morphology and local lattice symmetry of the Fe adlayer predominantly determine the magnetic properties of the Fe nanostructures: For an Fe coverage of less than 2.0 ML, pseudomorphic Fe layers on Pt(997) exhibit higher perpendicular remanent magnetization than Fe on Pt(111). Both, the increased orbital magnetic moment and the oscillatory anisotropy of Fe chains on Pt(997) as a function of chain width are ascribed to the detailed local symmetry.

The magnetism of the Fe-Pt surface alloy containing 0.5 ML Fe is substantially different from the 0.5 ML pure Fe layer on Pt(997). The large increase of the orbital magnetic moment of Fe in the surface alloy is found to be comparable to that of Fe monatomic chains, due to the similarly reduced coordination of Fe atoms in the two structures. It is demonstrated even for sub-monolayer Fe coverage that in Pt a considerable magnetic moment is induced, which is collinearly coupled to the Fe magnetic moments. Furthermore, the Fe-Pt surface alloy containing 0.5 ML Fe shows a

higher perpendicular magnetization than the 0.5 ML pure Fe layer on Pt(997). Those properties are a result of ordered alloy formation.

Growth of $4d$ metals such as Rh, Ru, and Mo on Pt(997) is studied to investigate the possibility to prepare monatomic chains and monolayers. In fact, a flat monolayer of Rh can be obtained near room temperature while Ru structures with low defect density are only obtained at higher coverages due to a more complicated growth mode. For the case of Mo, the formation of neither monolayers nor monatomic chains on Pt(997) is found.

This study suggests that local coordination and the hybridization at the interface are essential to understand the magnetism of nanostructures. These points are important also for the development of nanoscale magnetic devices in which the control of magnetic anisotropy, exchange interaction, and consideration of the spin-orbit coupling are important. This thesis focusses on static phenomena of magnetic nanostructures. Kinetic phenomena such as magnetization dynamics in nanoscale may be one of the future projects.

Chapter 5

Outlook

5.1 Kinked vicinal surfaces: The ultimate template for the bottom-up approach

In the experiments described in this work, Fe structures were assembled at step edges of the Pt(997) surface. It was shown that these rows could be made tens of nanometers long with a length restriction given by the distance between substrate kinks. It appears feasible to fabricate surfaces in which the miscut angle is not inclined in a symmetry plane of the crystal. Then the step does not form a low index step facet but this step facet becomes vicinal as well. Such a surface exhibits substrate steps of finite, well defined length, separated by monatomic kinks. The kinks provide adsorption sites with higher coordination in comparison to the straight step edge. When diffusion along the step edges is activated the kinks act as efficient nucleation sites for the growth of rows at the steps. This favors a kink-flow growth mode. The control of kink density and kink arrangement may allow us to introduce another parameter determining the construction of new surface structures.

Fig.5.1 depicts the vicinal Pt(39 38 30) surface: The surface index is chosen to have (111) terraces with 8 atoms width separated by step edges of 8 atoms in length[190, 191] . On such a surface is may be possible to create chains with defined length and position. It may also allow assembling structures at a high density in parallel – almost in an atom-by-atom fashion. A complex surface structure with a periodicity defined by the initial kink period may thus be assembled by depositing subsequently sub ML amounts of different adsorbates. Necessary conditions are that a surface can be prepared *in situ* and that the steps are thermodynamically stable. Kinked surfaces have already been
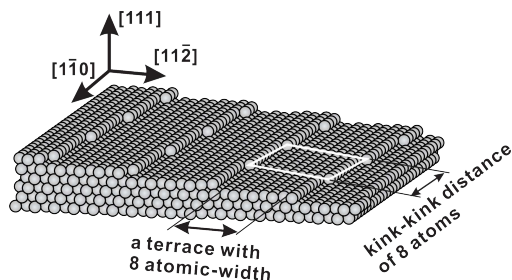
Figure 5.1 Perspective view of the idealized Pt(39 38 30) surface, whose (111) terraces with 8 atomic width are separated by steps of monatomic height, and step-edges are separated by kinks with distance of 8 atoms. A unit super cell from periodic array of kinks are indicated as white solid line.

employed as substrates with chiral selectivity[192] .

There are still many questions arising with respect to structural stability. Under which conditions and for which elements can such surfaces be prepared without kink bunching? Do kinks with the same geometry repel each other so that an ordered array with only small deviations can be prepared? Repulsion between kinks in adjacent steps of 22 meV has, in fact, been found for Ag(115)[193] . It is of fundamental interest to study how the interaction energy between kinks decreases with distance along the step and between adjacent steps. This dependence will eventually determine the maximum size of the super-cell which can be used. Is it possible to prevent ordered structures obtained by sequential deposition of adsorbates from destruction due to alloying? These questions could be addressed in future experiments as a continuing project of this thesis.

5.2 Magnetism of Mo, Ru, and Rh

Although $4d$ metals such as Mo, Ru, and Rh are paramagnetic in the bulk, the emergence of a magnetic moment is predicted for low-dimensional structures such as clusters and monatomic chains as a result of the reduced coordination of the atoms as well as the incomplete hybridization of the electronic wave functions with the Pt and Ag substrate[57–59] . Owing to their borderline magnetism, $4d$ nanostructures are expected to show striking changes in their magnetic properties as a function of their size and shape. This idea is supported by calculations which show that the magnetic
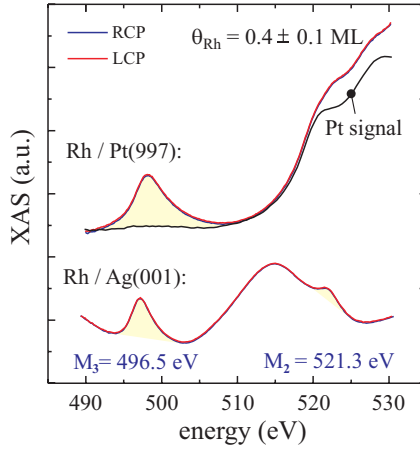
Figure 5.2 XAS signal of the $M_{2,3}$ edges of Rh with ultrathin Rh films on Pt(997) and Ag(001) measured at 10 K. The binding energies at $M_{2,3}$ edges from pure Rh are indicated[143] .

properties are highly sensitive to the local arrangement of the atoms on the surface and will be different for clusters and chains[57] . Therefore, the experimental probe of magnetic moment and magnetic anisotropy of the $4d$ nanostructures is extremely fascinating.

The TEAS study in Sec.2.4 shows that Rh and Ru can be grown in layered structures on Pt(997). On the other hand, only a 3D island growth mode is observed for Mo for the whole studied temperature range. Rh and Ru form chain structures through step decoration on the Pt(997) surface, and magnetic moments may emerge in Rh chains and Ru nanostructures, depending on morphology and width of the structure.

Due to the overlap of the $M_{2,3}$ adsorption edges of both Rh and Ru with edges of Pt in the substrate there were initially some doubts if a study of Rh and Ru at low coverages would be feasible. Measurements of Rh on Pt(997) and Ag(001) with coverages less than 0.5 ML were carried out by XMCD at the beamline ID-08 in the European synchrotron radiation facility (ESRF). Rh was deposited on the Pt(997) and Ag(001) surfaces at 10 K. At this low temperature no surface diffusion is expected to occur. Rh clusters with a size distribution from 1 to 3 atoms are formed according to Monte-Carlo simulations. Measurements of XMCD were done at the Rh $M_{2,3}$ absorption edges. The $M_{2,3}$ edges can be well distinguished from the background which is due to the absorption of the substrate. However, no dichroism is observed in the preliminary measurements. This result already underlines that the occurrence of

magnetism deos not depend only on the reduced dimensionality. Moreover, a particular atomic arrangement such as squared clusters or chains with certain symmetry is necessary, as suggested by theory[57,58] . A more systematic investigation especially at coverages below 0.1 ML is required to check a possible ferromagnetism of chain structures.

Also for Ru nanostructures, the $M_{2,3}$ absorption edges (E_{M_2} = 483.3 eV and $E_{M_3} = 461.5$ eV[143]) could be investigated in the energy range between 450 and 500 eV in future measurements.

The key question to answer is the appearance of magnetic ordering in Ru and Rh nanostructures on Pt and Ag substrates with and without applied magnetic field. The XMCD experiments may focus on (1) atomic chains of Rh formed on stepped Pt(997) as well as on flat Rh monolayers, as a comparison to the non-magnetic impurities. (2) Impurities and atomic chains of Ru on Pt(997) and Ag(001) may be studied.

The experimental results are of particular importance to verify the theoretical models describing the magnetism of $4d$ metals, such as the strong directional dependence of the magnetic moments and large anisotropy energy which are influenced by the electronic interaction with the substrate.

Appendix A

Magneto crystalline anisotropy of a fcc ferromagnet at sub ML coverage from the pair bonding model

The magnetic anisotropy with respect to the given crystal lattice is called magneto crystalline anisotropy (MCA). In this section, a general description of the pair-bonding model and its application to the explanation of MCA of a fcc ferromagnet at sub ML coverage will be discussed.

One can consider an ion as point-charge which interacts with its environment only through the "crystalline field" generated by surrounding "point-charges" at (r, θ, ϕ), which will be referred to as ligands. Then the perturbing electrostatic potential $V(r, \theta, \phi)$ is expressed as following[174,175] :

$$V(r, \theta, \phi) = \sum_j \frac{q_j}{|\vec{R}_j - \vec{r}|} \tag{A.1}$$

where q_j is the charge of the jth ligand at $\vec{R}_j$ from the origin. If the ion has charge q_i at (r_i, θ_i, ϕ_i), then the perturbing potential energy will be

$$W_c = \sum_i q_i V_i = \sum_i \sum_j \frac{q_i q_j}{|\vec{R}_j - \vec{r}|} \tag{A.2}$$

For the case of a "crystal", W_c has a certain directional dependence or anisotropy because the perturbation reflects crystal symmetry.
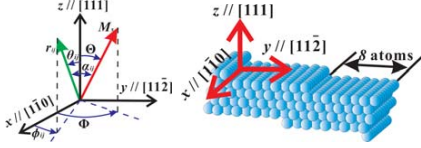
Figure A.1 Local coordinates of reference for the calculation of E_{MCA} on Pt(997) surface.

Without any assumption, Eq.(A.1) can be rewritten for a given symmetry by the use of spherical harmonics in terms of Legendre functions P_m^l for k charges as following:

$$V(r, \theta, \phi) = \sum_m \sum_{l=-m}^{m} r^m \gamma_{ml} Y_m^l(\theta, \phi) \tag{A.3}$$

where

$$\gamma_{ml} = \sum_{j=1}^{k} \frac{4\pi}{(2m+1)} \frac{q_j}{R_j^{m+1}} (-1)^l Y_m^{-l}(\theta_j, \phi_j)$$

$$Y_m^l(\theta, \phi) = (-1)^{(l+|l|)/2} \left[\frac{(2m+1) \cdot (m-|l|)!}{2(m+|l|)!} \right]^{1/2} \cdot \frac{1}{\sqrt{2\pi}} P_m^{|l|}(\cos\theta) \cdot \exp(il\phi)$$

$$P_m^0 \equiv P_m(x) = \sum_{l=0}^{m/2} (-1)^l \cdot \frac{(2m-2l)!}{2^m \cdot l! \cdot (m-l)! \cdot (m-2l)!} \cdot x^{m-2l} \, (\text{LegendrePolynomial})$$

$$P_m^l = (1-x^2)^{l/2} \frac{d^l P_m(x)}{dx^l} \qquad (\text{Associated LegendrePolynomial})$$

In case of a metallic system, the charges of the atomic cores are strongly screened by conduction electrons, and the crystal-field contributions from the ligands are reduced. Analytical expressions from the screened-charge effect were developed by R. Skomski *et al.*[175] .

For a magnetic ion in a crystal, the rotation of the magnetization results in a change of potential energy, which is called the magneto crystalline anisotropy (MCA). The MCA energy E_{MCA} is the relation between direction vector $\mathbf{r}_{ij}$ and magnetization $\mathbf{M_S}$ and should have the same functional form of Eq.(A.3).

One can consider the coordinates of reference shown in the Fig.A.1 . The vector $\mathbf{r}_{ij}$ connecting sites i and j makes an angle α_{ij} with $\mathbf{M_S}$. Within the frame of reference x, y, and z of the major crystallographic directions on the fcc (997) surface, $\mathbf{r}_{ij}$ and $\mathbf{M_S}$ make the angle θ_{ij}, ϕ_{ij}, Θ, and Φ, respectively. If one considers a uniform magnetization $\mathbf{M_S}$ and chemical bond between two atoms at $\mathbf{r}_i$ and $\mathbf{r}_j$, respectively, $\mathbf{M_S}$ and $\mathbf{r}_{ij} = \mathbf{r_i} - \mathbf{r_j}$ can be given as following:

$$\mathbf{M_S} = M_s(\sin\Theta\cos\Phi\, \mathbf{e_x} + \sin\Theta\sin\Phi\, \mathbf{e_y} + \cos\Theta\, \mathbf{e_z}) \tag{A.4}$$

$$\mathbf{r}_{ij} = r_{ij}(\sin\theta_{ij}\cos\phi_{ij}\ \mathbf{e_x} + \sin\theta_{ij}\sin\phi_{ij}\ \mathbf{e_y} + \cos\theta_{ij}\ \mathbf{e_z}) \tag{A.5}$$

where $M_s = |\mathbf{M_S}|$, $r_{ij} = |\mathbf{r}_{ij}|$, and $\mathbf{e_k}$ is the unit vector in direction k ($k = x, y,$ and z). Then, a complete and orthogonal form of E_{MCA} can be obtained from Eq.(A.3)[173] with a coefficient $a_l(r_{ij})$ as

$$E_{MCA} = \frac{1}{2}\sum_{i\neq j}\sum_{l} a_l(r_{ij}) \cdot P_l(\cos\alpha_{ij}) \tag{A.6}$$

From the comparison between Eq.(A.3) and Eq.(A.6), it is readily seen that $a_l(r_{ij})$ is determined by the wave functions of the magnetic ion, not by the symmetry of the crystal[174, 176]. Because $E_{MCA}(\cos\alpha_{ij}) = E_{MCA}(-\cos\alpha_{ij})$, only the orders of even integers $l = 0,\ 2,\ 4,\ \cdots$ contribute to E_{MCA}.

From the addition theorem of the Legendre functions[194], $P_l(\cos\alpha_{ij})$ can be expressed as following:

$$\begin{aligned}P_l(\cos\alpha_{ij}) &= P_l(\cos\Theta) \cdot P_l(\cos\theta_{ij}) \\ &+ 2\sum_{m=1}^{l}\frac{(l-m)!}{(l+m)!} \cdot P_n^{\,m}(\cos\Theta) \cdot P_n^{\,m}(\cos\theta_{ij}) \cdot \cos[m(\Phi - \phi_{ij})]\end{aligned} \tag{A.7}$$

From Eq.(A.6) and Eq.(A.7) one arrives at the formalism

$$\begin{aligned}E_{MCA} &= \sum_{l} G_l \cdot P_l(\cos\Theta) \\ &+ \sum_{l}\sum_{m=1}^{l} G_{lm}^{\,(c)} \cdot P_{\,m}^{\,l}(\cos\Theta) \cdot \cos m\Phi \\ &+ \sum_{l}\sum_{m=1}^{l} G_{lm}^{\,(s)} \cdot P_{\,m}^{\,l}(\cos\Theta) \cdot \sin m\Phi\end{aligned} \tag{A.8}$$

The superscripts (c) and (s) stand for cosine and sine, respectively. It is noted that all the microscopic details about the local symmetry and interaction are contained in the values G_{lm}:

$$G_l = \frac{1}{2}a_l(R_I)S_l \tag{A.9}$$

$$G_{\,lm}^{\,(c)} = a_l(R_I)\frac{(l-m)!}{(l+m)!}S_{\,lm}^{\,(c)} \tag{A.10}$$

$$G_{\,lm}^{\,(s)} = a_l(R_I)\frac{(l-m)!}{(l+m)!}S_{\,lm}^{\,(s)} \tag{A.11}$$

where the sums S_{lm} are purely dependent on the local symmetry as following:

$$S_l = \sum_{r=R_I} P_l(\cos\theta_{ij}) \tag{A.12}$$

$$S_{lm}^{(c)} = \sum_{r=R_I} P_{m}^{l}(\cos\Theta) \cdot \cos m\Phi \tag{A.13}$$

$$S_{lm}^{(s)} = \sum_{r=R_I} P_{m}^{l}(\cos\Theta) \cdot \sin m\Phi \tag{A.14}$$

If there are p independent atomic sites such as terrace sites, step sites, kink sites, *etc.*, and the total number of atoms is $N = N_1 + N_2 + \cdots + N_\mu + \cdots + N_p$, then the averaged magneto-crystalline anisotropy is calculated as

$$E_a = \sum_l \kappa_l P_l(\cos\Theta)$$

$$+ \sum_l \sum_{m=1}^{l} \kappa_{lm}^{(c)} P_{m}^{l}(\cos\Theta) \cdot \cos m\Phi$$

$$+ \sum_l \sum_{m=1}^{l} \kappa_{lm}^{(s)} P_{m}^{l}(\cos\Theta) \cdot \sin m\Phi \tag{A.15}$$

where

$$\kappa_l \equiv \sum_{\mu=1}^{p} \left(\frac{N_\mu}{N}\right) \cdot G_l(\mu) \tag{A.16}$$

$$\kappa_{lm}^{(c)} \equiv \sum_{\mu=1}^{p} \left(\frac{N_\mu}{N}\right) \cdot G_{lm}^{(c)}(\mu) \tag{A.17}$$

$$\kappa_{lm}^{(s)} \equiv \sum_{\mu=1}^{p} \left(\frac{N_\mu}{N}\right) \cdot G_{lm}^{(s)}(\mu) \tag{A.18}$$

In other words, the Néel's macroscopic anisotropy coefficients $\{\kappa\}$ are weighted averages of the local, site-dependent anisotropy coefficients $\{G(\mu)\}$, which are determined by the local symmetry which again is represented by the *structure factors* $\{S_{lm}\}$ and the coefficients a_l.

Historically, E_{MCA} of a bulk cubic ferromagnet has been expressed as a multi-power polynomial of the sine function.

$$E_a = K_1 \sin^2\Theta + K_2 \sin^4\Theta + \cdots \tag{A.19}$$

in which K_1, K_2 $\cdots$ are known as magneto-crystalline anisotropy constants. From the one-to-one correspondence between Eq.(A.19) and Eq.(A.15), the relation between the lower order anisotropy constants K_s ($s = 1, 2, 3, \cdots$) and the anisotropy coefficients κ_q

$(q = 2,4,6,\cdots)$ can be found:

$$K_0 = \kappa_0$$
$$K_1 = -\frac{3}{2}\kappa_2 - 5\kappa_4 - \frac{21}{2}\kappa_6$$
$$K_2 = \frac{35}{8}\kappa_4 + \frac{189}{8}\kappa_6 \qquad (A.20)$$
$$K_3 = -\frac{231}{16}\kappa_6$$

or

$$\kappa_0 = K_0$$
$$\kappa_2 = -\frac{2}{3}K_1 - \frac{16}{21}K_2 - \frac{16}{21}K_3$$
$$\kappa_4 = \frac{8}{35}K_2 + \frac{144}{385}K_3 \qquad (A.21)$$
$$\kappa_6 = -\frac{16}{231}K_3$$

Let us first check the validity of the above equations for a description of bulk ferromagnet anisotropy. For bulk atoms, it is readily seen from Eq.(A.12) to Eq.(A.14) that E_{MCA} is independent of the order $l = 2$ because of the high symmetry of their environment. Therefore E_{MCA} is mostly determined by the structure factors with the order $l = 4$. It is well known that K_2 and K_3 of bulk fcc Ni (bcc Fe) are negative (positive) at temperatures below 20 K[56]. Therefore, κ_4 for fcc and bcc bulk atoms is assumed from Eq.(A.21) to be negative and positive, respectively.

The calculated E_{MCA} with a negative value of κ_4 for a fcc bulk ferromagnet is shown in Fig.A.2. Note that the global minima and maxima correspond to the magnetic easy- and hard- directions, respectively. Therefore, Fig.A.2 shows that the magnetic easy-, mid-, and hard- axes are $\langle 111 \rangle$, $\langle 110 \rangle$, and $\langle 100 \rangle$ directions, respectively, which exactly corresponds to the MCA of bulk fcc Ni.

The calculated E_{MCA} with a positive value of κ_4 for a bcc bulk ferromagnet is shown in Fig.A.3, which exactly describes the MCA of bulk bcc Fe: the magnetic easy-, mid-, and hard- axes are $\langle 100 \rangle$, $\langle 110 \rangle$, and $\langle 111 \rangle$ respectively. Therefore, the above formalism from the spherical harmonic expansion of the cubic crystal field are valid for the qualitative description of the bulk magneto-crystalline anisotropy.

Table.A.1 shows the change in the local coordination of a pseudormophic magnetic overlayer on the fcc (997) surface (in our case Fe on Pt(997)) as a function of coverage. It is clear from Table.A.1 that the atoms at second nearest neighbors' distance in the fcc symmetry appear only when the coverage is higher than 1 ML. Therefore, the pair-interaction with second nearest neighbors does not exist for $\theta_{Fe} < 1$ ML. Considering the
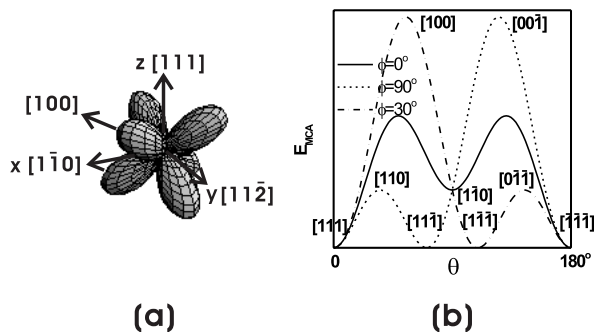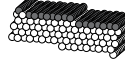
Figure A.2 (a) Distribution of E_{MCA} in the local coordinates xyz for the fcc bulk atom with $\kappa_4 = -1.0$, and (b) E_{MCA} as a function of Θ for several directions (Φ) of high symmetry.

rapid decay of the magnitude of $a_l(r)$ as a function of distance r^{195} , contributions from third, fourth, *etc.* nearest neighbors is ignored here. Only the pair-interaction between nearest neighbors located at $r = R_I$ (R_I is the distance between nearest neighbors) will be treated in this section. Furthermore, the order l of the terms of Legendre polynomial higher than 6 will be ignored because their contribution is $6 \sim 7$ orders of magnitude smaller[195] than those of $l = 2$ and 4. Electronic structure of the elements and local symmetry determines κ. To discriminate those two factors, κ will be expressed as $a_l(R_I)\acute{\kappa}$,
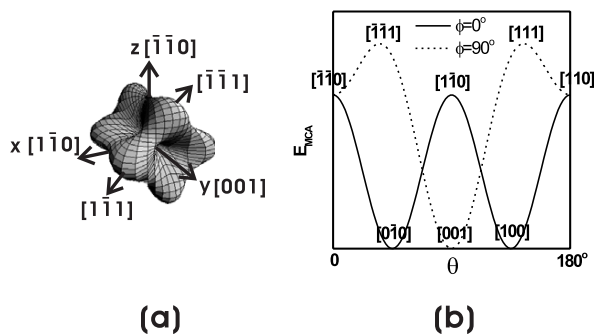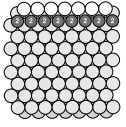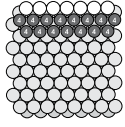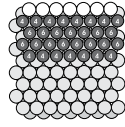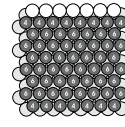

Figure A.3 (a) Distribution of E_{MCA} in the local coordinates xyz for the bcc bulk atom with $\kappa_4 = +1.0$, and (b) E_{MCA} as a function of Θ for several directions (Φ) of high symmetry.

Table A.1 Change of the local coordination of Fe overlayer on Pt(997) as a function of coverage. Black atoms indicate Fe, and white/gray atoms indicate Pt. Number of nearest neighbors are indicated on Fe atoms.

where the coefficient $a_l(R_I)$ contains information on the electronic structure and the coefficient $\acute{\kappa}$ is purely determined by local symmetry.

As illustrated in Fig.A.4 there are only four equivalent atomic sites on fcc (997) surfaces if only the coordination to the nearest neighbors is considered: bulk, surface, step-edge, and step-corner site. Atoms at the surface, step-edge, and step-corner have a lower symmetry environment than the bulk atoms. Therefore, structure factors with order $l = 2$ in Eq.(A.12) to Eq.(A.14) are non-zero, and different contributions from each site should be averaged. With the use of Eq.(A.12) to (A.14), the inequivalent contributions of each site to the macroscopic anisotropy coefficients $\acute{\kappa}$ for a given adlayer coverage can be evaluated as in Table.3.1. Several facts should be noted: First, a structure factor with the order $l = 2$ appears when the coverage is less than 8 atomic rows and for the surface atom. Second, the anisotropy energy will depend on the azimuthal angle Φ because of the non-zero values of the $\acute{\kappa}_{lm}$ terms for sub-ML coverage. This azimuthal dependence rapidly decreases with increasing coverage.

Now the shape of E_{MCA} is determined from the magnitude and signs of a_2 and a_4. From the criterion $\partial E_{MCA}/\partial(\Theta, \Phi) = 0$ and $\partial^2 E_{MCA}/\partial(\Theta, \Phi)^2 = 0$, which corresponds to energy minimization with respect to the variables Φ and Θ, a magnetic phase diagram can be obtained with respect to the values a_2 and a_4. An example of the phase diagram
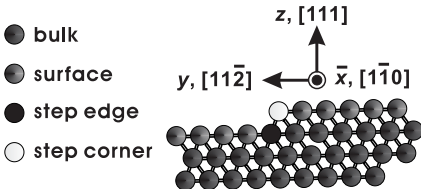
Figure A.4 Side-view of fcc (997) crystal along $[\bar{1}10]$ direction. Four inequivalent atomic sites are indicated with different colors.
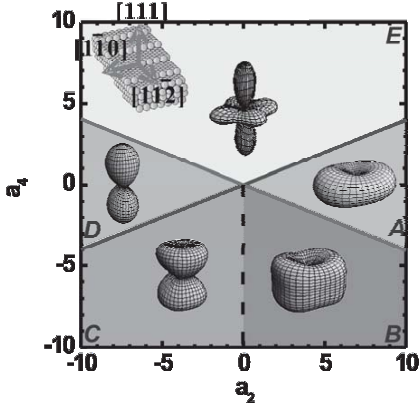
Figure A.5 Magnetic phase diagram of 4 rows or 0.5 ML of fcc ferromagnet on fcc (997) surface. Five areas A, B, C, D, and E with distinctive shape of E_{MCA} with respect to a_2 and a_4 are indicated with typical examples.

for a 4-rows-adlayer is shown in Fig.A.5, in which five distinctive areas are obtained with respect to the traits of E_{MCA} shape: E_{MCA} in region A has a global minimum in $\langle 111 \rangle$ direction. E_{MCA} in region B has a global minimum in $\langle 111 \rangle$ direction and local minima in $\langle 1\bar{1}0 \rangle$ and $\langle 11\bar{2} \rangle$ directions. In region C, the global minima appear in $\langle 1\bar{1}0 \rangle$ and $\langle 11\bar{2} \rangle$ directions, and a local minimum in $\langle 111 \rangle$ direction. In region D, the global minimum is degenerate around the $\{111\}$ plane. E_{MCA} in region E is characterized by local maxima in the $\langle 111 \rangle$, $\langle 1\bar{1}0 \rangle$, and $\langle 11\bar{2} \rangle$ directions.

Appendix B

Correction of hysteresis loops in XMCD measurements from the total electron yield current

In hysteresis loops measured by XMCD with total electron yield (TEY) artifacts appear near $\mathbf{B} \approx 0$ as shown in Fig.3.4. The artifacts become stronger as the angle of incidence increases (grazing geometry). They make it difficult to extract important information from the data such as *e.g.* the remanent magnetization. Their origin is the motion of secondary electrons after escaping from the sample. In this section, a method is presented which allows to remove the artifacts in a more efficient way than the conventional method which is usually employed.

The background

As discussed in Sec.3.1.1, hysteresis loops are obtained in XMCD from the ratio of the absorption coefficients at two different photon energies, namely the XMCD peak energy (here at the L_3 edge: E_{L_3}) and the pre-edge energy (E_{pre}) as defined in Fig.3.2. The division by the intensity at the pre-edge energy is necessary to normalize to variations of external parameters like *e.g.* the incident X-ray beam intensity.

Only the normalized TEY current provides a value proportional to the absorption coefficient μ[129, 130, 135, 136] because the following processes occur: An incident photon creates a core hole in a near-surface region. The hole is filled with an electron from an upper energy level. As a result secondary electrons with low kinetic energy of a

few eV are generated, and low-energy electrons are emitted thus creating the detected photoelectron current, which corresponds to the TEY current. The yield of secondary electrons which are emitted from the surface by single photon excitation which is defined as the total-electron-yield (TEY) can be expressed as follows[130, 135, 136] :

$$\eta = K(E)\frac{\mu_\theta}{1/L_s + \mu_\theta}\left\{1 - \exp\left[-\left(\frac{1}{L_s} + \mu_\theta\right)d\right]\right\} \approx K(E) \cdot \mu_\theta \cdot d \qquad \text{(B.1)}$$

in which $\mu_\theta = \mu/\cos\theta$, L_s is the escape length of the secondary electrons, d is the penetration depth of the photon, and K is a proportionality factor which depends on E, the energy of the incident photons. For the systems discussed in this thesis the studied adlayer is smaller than both L_s and d, while $L_s \ll d$ due to the weak attenuation of the X-rays.

For TEY measurements one has to take into account that the details of absorption and the energy distribution of the emitted electrons depend on the incident photon energy. One has to include the energy dependence in $K(E)$ and thus write:

$$I_{\text{TEY}} = -K(E) \cdot d \cdot \mu_\theta(E) \cdot \xi(t) \qquad \text{(B.2)}$$

where $\mu_\theta(E)$ is the absorption coefficient at photon energy E and incidence angle θ. From here on the explicit indication the angular dependence of μ will be omitted. $\xi(t)$ introduces in addition temporal variation occurring in all measured signals *e.g.* due to the time dependence of the X-ray intensity at a beamline. The method used for normalization in the literature is $N_{conventional}$ and is defined as:

$$N_{conventional}(B) = \frac{S_+(\mathbf{B})}{P_+(\mathbf{B})} = \frac{K(E_{L_3}, \mathbf{B}) \cdot \xi(t_1)}{K(E_{pre}, \mathbf{B}) \cdot \xi(t_1)} \cdot \frac{\mu_+(E_{L_3}, \mathbf{M})}{\mu_+(E_{pre})} \qquad \text{(B.3)}$$

Here S is the signal on the XMCD peak and P is the signal at the pre-edge energy. The superscript plus indicates the use of right-circularly polarized light. The polarization is assumed to leave the signal at the pre-edge energy unaffected but provides the sensitivity of the absorption on sample magnetization M on the L_3 absorption edge as indicated by the factor $\mu_+(E_{E_{L_3}}, M)$. The factor ξ does not contribute to $N_{conventional}$ and cancels because the measurements at the peak and the pre-edge are made almost at the same time, *i.e.* within a few seconds.

It is noted that for $N_{conventional}$ the photon energy dependence cancels out only if the ratio $K(E_{L_3})/K(E_{pre})$ is independent of $\mathbf{B}$. Else, the artifacts will not be completely removed. In fact, this ratio changes with the size of applied electric and magnetic fields as the electron trajectories depend on the resulting Lorentz force which depends on these fields and, most importantly here, on the distribution of kinetic energy of the electrons.

The trajectories will thus be bent so that a significant fraction of escaping electrons will return to the sample and thus do not contribute to the TEY current. An improved normalization procedure should thus eliminate the energy dependence as is suggested in this work:

$$
\begin{aligned}
N_0(\mathbf{B}, M) &= \frac{S_+(\mathbf{B}, \mathbf{M}, \xi(t_1))}{P_+(\mathbf{B}, \xi(t_1))} \cdot \frac{P_0(\mathbf{B}, \xi(t_2))}{S_0(\mathbf{B}, \mathbf{M}, \xi(t_2))} \\
&= \left\{ \frac{K(E_{L_3}, \mathbf{B}) \cdot \xi(t_1)}{K(E_{pre}, \mathbf{B}) \cdot \xi(t_1)} \cdot \frac{\mu_+(E_{L_3}, \mathbf{M})}{\mu_+(E_{pre})} \right\} \cdot \left\{ \frac{K(E_{pre}, \mathbf{B}) \cdot \xi(t_2)}{K(E_{L_3}, \mathbf{B}) \cdot \xi(t_2)} \cdot \frac{\mu_0(E_{pre})}{\mu_0(E_{L_3})} \right\}
\end{aligned}
$$
(B.4)

where the subscript '0' denote a full hysteresis loop, however, measured with unpolarized light at a time t_2.

The K factors as well as the ξ cancel out, and assuming an independence of the preedge absorption on the beam polarization $\mu_+(E_{pre}) = \mu_0(E_{pre})$ we find the result:

$$
N_0(\mathbf{B}, \mathbf{M}) = \frac{\mu_+(E_{L_3}, \mathbf{M})}{\mu_0(E_{L_3})} = 1 + \hat{\mu}_+(E_{L_3}, \mathbf{M})
$$
(B.5)

which is independent of the energy distribution of emitted electrons and of the changes of beam intensity. In Eq.(B.5) the absorption coefficient was separated into a $\mathbf{M}$ dependent and a magnetization independent part which is identical to the term in the denominator. $\hat{\mu}_+(E_{L_3}, \mathbf{M})$ is the actual XMCD signal. A drawback to Eq.(B.5) is that it requires the additional measurement with an unpolarized beam which results in a doubling of measuring time. In addition, the beam position on the sample can depend on the polarization state of the beam due to the X-ray optics of the beamline so that new artifacts might be introduced. Therefore, it is suggested to replace the measurement with an unpolarized beam by the average of two data points obtained by a beam of identical polarizations but for a sample with reversed magnetization and a reversed magnetic field:

$$
S_0(\mathbf{B}, \mathbf{M}) \approx \frac{S_+(\mathbf{B}, \mathbf{M}) + S_+(-\mathbf{B}, -\mathbf{M})}{2}
$$
(B.6)

If we denote with $i = 1, 2$ the two branches of a hysteresis curve one can alternatively write:

$$
S_0(\mathbf{B}, i) \approx \frac{S_+(\mathbf{B}, i) + S_+(-\mathbf{B}, 3 - i)}{2}
$$
(B.7)

Equivalent relations are used for $P(B, i)$. Then, for the original measurement of two branches of a single hysteresis curve one obtains the new normalization:

$$
N_{new}(\mathbf{B}, i) = \frac{S(\mathbf{B}, i)}{P(\mathbf{B}, i)} \cdot \frac{P(\mathbf{B}, i) + P(-\mathbf{B}, 3 - i)}{S(\mathbf{B}, i) + S(-\mathbf{B}, 3 - i)}
$$
(B.8)

Using Eq.(B.2) one obtains:

$$N_{new}(\mathbf{B}, \mathbf{M}) = \left\{ \frac{K(E_{L_3}, \mathbf{B}) \cdot \xi(t_1)}{K(E_{pre}, \mathbf{B}) \cdot \xi(t_1)} \cdot \frac{\mu_+(E_{L_3}, \mathbf{M})}{\mu_+(E_{pre})} \right\} \times$$
$$\left\{ \frac{K(E_{pre}, \mathbf{B}) \cdot \xi(t_1) \cdot \mu_+(E_{pre}) + K(E_{pre}, -\mathbf{B}) \cdot \xi(t_2) \cdot \mu_+(E_{pre})}{K(E_{L_3}, \mathbf{B}) \cdot \xi(t_1) \cdot \mu_+(E_{L_3}, \mathbf{M}) + K(E_{L_3}, -\mathbf{B}) \cdot \xi(t_2) \cdot \mu_+(E_{L_3}, \mathbf{M})} \right\}$$

$$(B.9)$$

which simplifies to:

$$N_{new}(\mathbf{B}, \mathbf{M}) = \frac{\mu_+(E_{L_3}, \mathbf{M}) \big[\xi(t_1) + \xi(t_2) \big]}{\mu_+(E_{L_3}, \mathbf{M}) \cdot \xi(t_1) + \mu_+(E_{L_3}, -\mathbf{M}) \cdot \xi(t_2)} \qquad (B.10)$$
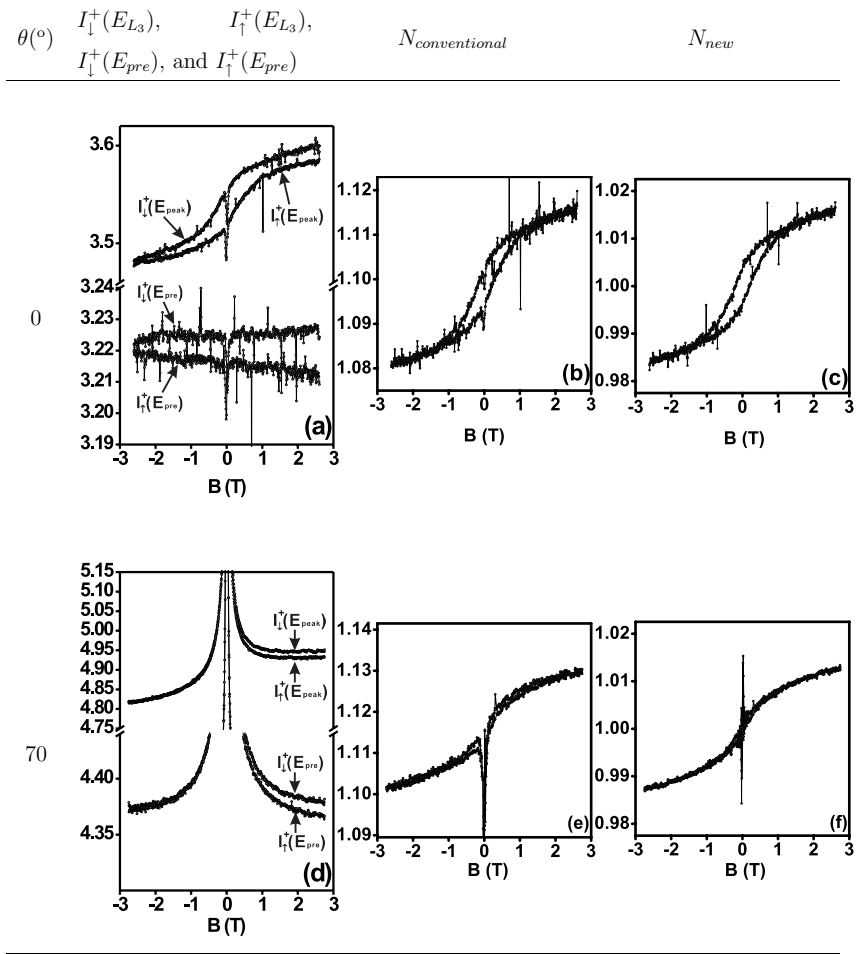
Here the electron energy dependence in K has, in fact, cancelled out. A remark has to be made, however, because a cancelling of the photon energy dependence implies that the time dependence remains entangled in the averaging procedure. This is, however, a much smaller effect than the one due to the energy dependence as will be shown in the examples below. The values t_1 and t_2 only refer to the times when the two branches of a single loop are measured. A simple solution to this remaining problem is the explicit normalization of all signals to the electron ring current of the synchrotron. This value is continuously monitored during each measurement.

It has to be emphasized that Eq.(B.8) does not implement a simple curve symmetrization which would lead to a substantial loss of information in the data. It implements a normalization which, however, also uses the symmetry properties of the artifact by assuming that the escape probability depends on the magnitude but not on the direction of the magnetic field. Contributions to the artifact for which this symmetry does not hold cannot be removed completely.

Examples and Discussion

Table B.1 shows the TEY current normalized by the beam current (referred to as TEY signal hereafter) of 0.5 ML of Fe on Pt(997) measured at the L_3 edge with $\theta = 0^\circ$ and 70° from PM3 beamline in BESSY II. TEY signals at the pre-edge and peak were obtained at the photon energy of $E_{pre} = 695.0$ eV and $E_{L_3} = 708.5$ eV, respectively. In Table B.1 (a) the TEY signals $I_\downarrow^+(E_{L_3})$, $I_\uparrow^+(E_{L_3})$, $I_\downarrow^+(E_{pre})$, and $I_\uparrow^+(E_{pre})$ measured at $\theta = 0^\circ$ are shown, in which ↑ and ↓ indicate continuous change of magnetic field from $+\mathbf{B}$ to $-\mathbf{B}$ and from $-\mathbf{B}$ to $+\mathbf{B}$, respectively. Apart from the noise, $I_\downarrow^+(E_{L_3})$ and $I_\uparrow^+(E_{L_3})$ show clear hysteric behavior with respect to the change of the $\mathbf{B}$, on the other hand $I_\downarrow^+(E_{pre})$ and $I_\uparrow^+(E_{pre})$ is almost insensitive to the change of $\mathbf{B}$. The decrease of the intensity of the four curves near $\mathbf{B} = 0$ is visible. Because the magnitude and

Table B.1 TEY signals and hysteresis loops from normalization with the value of $N_{conventional}$ and N_{new} of 0.5 ML of Fe on Pt(997) measured at L_3 edge at $\theta = 0^\circ$ and 70°.

$\theta(^\circ)$	$I_\downarrow^+(E_{L_3})$, $I_\uparrow^+(E_{L_3})$, $I_\downarrow^+(E_{pre})$, and $I_\uparrow^+(E_{pre})$	$N_{conventional}$	N_{new}
0			
70			

distribution of the TEY current measured at the peak and pre-edge are not identical, this artifact is still visible in the value of $N_{conventional}$ of Table B.1(b). In contrast, the artifact is absent in N_{new} shown in Table B.1 (c). It is shown that the overall shape of the hysteresis loop remains the same as in Table B.1 (b). Therefore, the normalization implemented in N_{new} makes it possible to access information such as remnant magnetization which cannot be evaluated from the normalization through $N_{conventional}$.

The artifact becomes stronger when θ increases. This is due to the fact that the component perpendicular to the surface in the Lorentz force is reduced which leads to a trajectory which is more likely to bring the electron back to the sample surface. In Table B.1 (d) four TEY signals at the peak and pre-edge are shown for 0.5 ML of Fe on Pt(997) measured at $\theta = 70^o$. In contrast to Table B.1 (e) the N_{new} correction in Table B.1 (f) removes most of the artifact. The still incomplete removal may be due to non-linearities in signal recording, charging effects or a residual odd symmetry in the B-field dependence of the artifact.

In the following, the effect of an externally applied electric field on N_{new} will be described. The electric field is employed to accelerate the escaping electrons perpendicular to the surface and thus increase the measured emission current. In Table B.2 measurements of TEY signals and hysteresis loops of 2.0 ML Fe on Pt(997) measured at the L_3 edge are shown for an incidence angle of $\theta = 60^o$. In this measurement at the BL 4.2 beamline at ELETTRA, B was not scanned but changed discontinuously. TEY signals at pre-edge and peak were obtained at the photon energies $E_{pre} = 705.6$ eV and $E_{L_3} = 711.8$ eV, respectively. All TEY signals in Table B.2 (a) show an artefact near $\mathbf{B} = 0$. When the a high voltage is applied to an electrode close to the sample surface the resulting electric field $\mathcal{E}$ leads to an increase of the TEY signal by a factor of two. The artefact near $\mathbf{B} = 0$ splits into two and shifts to $\mathbf{B} = \pm 0.02$ T. It is found that there is no substantial difference between applied potentials at the counter electrode of 1 kV and 2 kV. Table B.2 demonstrates that the N_{new} correction (Eq.(B.8)) reduces the artifact with respect to the conventional correction and even succeeds to remove it completely is many cases.

Table B.2 TEY signals and hysteresis loops from normalization with the value of $N_{conventional}$ and N_{new} of 2.0 ML of Fe on Pt(997) measured at L_3 edge at $\theta = 70^{\circ}$ with and without application of the electric field.
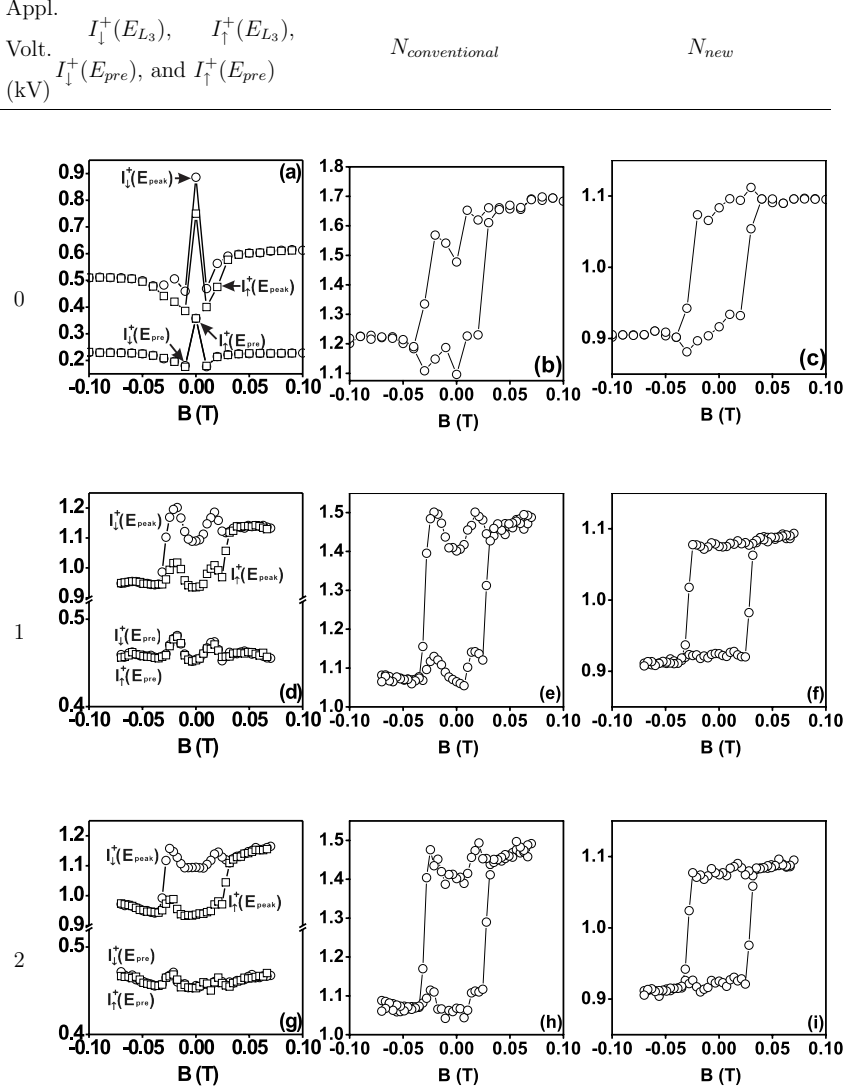
Appl. Volt. (kV)	$I_{\downarrow}^{+}(E_{L_3})$, $I_{\uparrow}^{+}(E_{L_3})$, $I_{\downarrow}^{+}(E_{pre})$, and $I_{\uparrow}^{+}(E_{pre})$	$N_{conventional}$	N_{new}

Bibliography

[1] V. S. Speriosu, D. A. Herman, I. L. sanders, and T. Yogi, IBM J. Res. Develop. **44**, 186 (2000).

[2] R. L. Comstock, J. Mater. Sci. -Mater. El. **13**, 509 (2002).

[3] R. Carey, D. M. Newman, and B. W. J. Thomas, J. Phys. D :Appl. Phys. **28**, 2207 (1995).

[4] G. Grynkewich, J. Åkerman, P. Brown, B. Butcher, R. W. Dave, M. DeHerrera, M. Durlam, B. N. Engel, J. Janesky, S. Pietambaram, N. D. Rizzo, J. M. Slaughter, K. Smith, J. J. Sun, and S. Tehrani, MRS Bull. **11**, 818 (2004).

[5] P. Grüberg, Phys. Today **54**, 31 (2001).

[6] R. Victora and J. MacLaren, Phys. Rev. B **47**, 11583 (1993).

[7] J. Stöhr, J. Mag. Mag. Mat. **200**, 470 (1999).

[8] E. Plummer, Ismail, R. Matzdorf, A. Melechko, J. Pierce, and J. Zhang, Surf. Sci. **500**, 1 (2002).

[9] S. Bader, Surf. Sci. **500**, 172 (2002).

[10] H. Hauser, R. Chabicovsky, and K. Riedling, *Thin Magnetic Films*, volume 5 of *Nanomaterials and Magnetic Thin Films, Handbook of Thin Film Materials*, Academic Press, San Diego, 2002.

[11] P. Gambardella, A. Dallmeyer, K. Maiti, M. C. Malagoli, S. Rusponi, P. Ohresser, W. Eberhardt, C. Carbone, and K. Kern, Phys. Rev. Lett. **93**, 077203 (2004).

[12] D. Weller, Y. Wu, J. Stöhr, M. Samant, B. Hermsmeier, and C. Chappert, Phys. Rev. B **49**, 12888 (1994).

[13] J. Thiele, C. Boeglin, K. Hricovini, and F. Chevrier, Phys. Rev. B **52**, R11934 (1996).

[14] J. Nogués and I. K. Schuller, J. Mag. Mag. Mat. **192**, 203 (1999).

[15] A. E. Berkowitz and K. Takano, J. Mag. Mag. Mat. **200**, 552 (1999).

[16] N. Nakajima, T. Koide, T. Shidara, H. Miyauchi, H. Fukutani, A. Fujimori, K. Iio, T. Katayama, M. Nývlt, and Y. Suzuki, Phys. Rev. Lett. **81**, 5229 (1998).

[17] H. J. Levinson and W. H. Arnold, *Optical Lithograpny*, volume 1 of *SPIE Press monograph; IEEE materials and devices series*, chapter 1, pages 11–138, SPIE Optical Engineering Press, Bellingham, 1997.

[18] F. Cerrina, *X-Ray Lithography*, volume 1 of *SPIE Press monograph; IEE materials and devices series*, chapter 3, pages 251–320, SPIE Optical Engineering Press, Bellingham, 1997.

[19] B. Michel, A. Bernard, A. Bietsch, E. Delamarche, M. Geissler, D. Juncker, H. Kind, J.-P. Renault, H. Rothuizen, H. Schmid, P. Schmidt-Winkel, R. Stutz, and H. Wolf, IBM J. Res. Develop. **45**, 697 (2001).

[20] E. F. Wassermann, M. Thielen, S. Kirsch, A. Pollmann, H. Weinforth, and A. Carl, J. Appl. Phys. **83**, 1753 (1998).

[21] A. N. Boto, P. Kok, D. S. Abrams, S. L. Braunstein, C. P. Williams, and J. P. Dowling, Phys. Rev. Lett. **85**, 2733 (2000).

[22] M. A. McCord and M. J. Rooks, *Electron Beam Lithography*, volume 1 of *SPIE Press monograph; IEEE materials and devices series*, chapter 2, pages 139–250, SPIE Optical Engineering Press, Bellingham, 1997.

[23] S. Y. Chou, P. R. Krauss, and P. J. Renstrom, Science **272**, 85 (1996).

[24] S. Y. Chou, C. Keimel, and J. Gu, Nature **417**, 835 (2002).

[25] J. von Neumann, *Theory of self-reproducing automata*, Univ. of Illinois Press, Urbana, 1966.

[26] J. Z. Zhang, Z. L. Wang, J. Liu, S. Chen, and G. Y. Liu, *Self-assembled Nanostructures*, Kluwer Academic/Plenum Publishers, New York, 2003.

[27] M. Knez, M. Sumser, A. Bittner, C. Wege, H. Jeske, D. Hoffmann, K. Kuhnke, and K. Kern, Langmuir **20**, 441 (2004).

[28] F. Y. Li, L. Zhang, and R. M. Metzger, Chem. Mat. **10**, 2470 (1998).

[29] W. C. Hu, D. W. Gong, Z. Chen, L. M. Yuan, K. Saito, C. A. Grimes, and P. Kichambare, Appl. Phys. Lett. **79**, 3083 (2001).

[30] H. Gao, C. Mu, F. Wang, D. S. Xu, K. Wu, Y. C. Xie, S. Liu, E. G. Wang, J. Xu, and D. P. Yu, J. Appl. Phys. **93**, 5602 (2003).

[31] S. U. Yuldashev, S. W. Choi, T. W. Kang, and L. A. Nosova, J. Korean Phys. Soc. **42**, S216 (2003).

[32] U. Welp, Z. L. Xiao, J. S. Jiang, V. K. Vlasko-Vlasov, S. D. Bader, G. W. Crabtree, J. Liang, H. Chik, and J. M. Xu, Phys. Rev. B **66**, 212507 (2002).

[33] J. Y. Cheng, C. A. Ross, E. L. Thomas, H. I. Smith, and G. J. Vancso, Adv. Mater. **15**, 1599 (2003).

[34] J. Y. Cheng, C. A. Ross, V. Z. H. Chan, E. Thomas, R. G. H. Lammertink, and G. Vancso, Adv. Mater. **13**, 1174 (2001).

[35] J. Y. Cheng, W. Jung, and C. A. Ross, Phys. Rev. B **70**, 064417 (2004).

[36] S. Sun, C. Murray, D. Weller, L. Folks, and A. Moser, Science **287**, 1989 (2000).

[37] D. Zitoun, C. Amiens, B. Chaudret, M. C. Fromen, P. Lecante, M. J. Casanove, and M. Respaud, J. Phys. Chem. B **107**, 6997 (2003).

[38] Y. H. Gao, Y. P. Bao, M. Beerman, A. Yasuhara, D. Shindo, and K. M. Krishnan, Appl. Phys. Lett. **84**, 3361 (2004).

[39] H. Brune, M. Giovannini, K. Bromann, and K. Kern, Nature **394**, 451 (1998).

[40] E. Kumacheva, R. K. Golding, M. Allard, and E. H. Sargent, Adv. Mat. **14**, 221 (2002).

[41] R. K. Golding, P. C. Lewis, E. Kumacheva, M. Allard, and E. H. Sargent, Langmuir **20**, 1414 (2004).

[42] M. Crommie, C. Lutz, and D. Eigler, Science **262**, 218 (1993).

[43] H. Manoharan, C. Lutz, and D. Eigler, Nature **403**, 512 (2000).

[44] J. M. Howe, *Interfaces in Materials: Atomic Structure, Thermodynamics and Kinetics of Solid-Vapor, Solid-Liquid and Solid-Solid Interfaces*, John Wiley & Sons, Inc., New York, 1997.

[45] B. Poelsema, L. K. Verheij, and G. Comsa, Phys. Rev. Lett. **53**, 2500 (1984).

[46] L. K. Verheij, J. A. V. D. Berg, and D. G. Armour, Surf. Sci. **122**, 216 (1982).

[47] Y. Li, T. J. Raeker, and A. E. DePristo, Phys. Rev. B **50**, 14742 (1994).

[48] E. Hahn, H. Schief, V. Marsico, A. Fricke, and K. Kern, Phys. Rev. Lett. **72**, 3378 (1998).

[49] F. K. Men, F. Liu, P. J. Wang, C. H. Chen, D. L. Cheng, J. L. Lin, and F. J. Himpsel, Phys. Rev. Lett. **88**, 096105 (2002).

[50] S. Rousset, V. Repain, G. Baudot, Y. Garreau, and J. Lecoeur, J. Phys. :Condens. Matter. **15**, S3363 (2003).

[51] P. Gambardella, M. Blanc, L. Burgi, K. Kuhnke, and K. Kern, Surf. Sci. **449**, 93 (2000).

[52] V. Marsico, M. Blanc, K. Kuhnke, and K. Kern, Phys. Rev. Lett. **78**, 94 (1997).

[53] P. Gambardella, M. Blanc, H. Brune, K. Kuhnke, and K. Kern, Phys. Rev. B **61**, 2254 (2000).

[54] J. Kübler, *Theory of Itinerant Electron Magnetism*, Oxford University Press, New York, 2000.

[55] S. Blundell, *Magnetism in Condensed Matter*, Oxford Master Series in Condensed Matter Physics, Oxford University Press, Oxford, 2001.

[56] R. O'Handley, *Modern Magnetic Materials: Principles and Applications*, John Wiley & Sons, Inc., New York, 2000.

[57] P. Lang, V. Stepanyuk, K. Wildberger, R. Zeller, and P. Dederichs, Solid State Comm. **92**, 755 (1994).

[58] K. Wildberger, V. Stepanyuk, P. Lang, R. Zeller, and P. Dederichs, Phys. Rev. Lett. **75**, 509 (1995).

[59] H. Dryssé and C. Demangeat, Surf. Sci. Rep. **28**, 65 (1997).

[60] M. van Hove and S. Tong, *Surface Crystallography by LEED: Theory, Computation and Structural Results*, volume 2 of *Springer Series in Chemical Physics*, Springer-Verlag, Berlin, 1979.

[61] L. C. Feldman and J. W. Mayer, *Fundamentals of Surface and Thin Film Analysis*, North-Holland, Amsterdam, 1986.

[62] J. A. Stroscio and W. J. Kaiser, editors, *Scanning Tunneling Microscopy*, volume 27 of *Methods of Experimental Physics*, Academic Press Inc., San Diego, 1993.

[63] B. Poelsema and G. Comsa, *Scattering of Thermal Energy Atoms from Disordered Surfaces*, volume 115 of *Springer Tracts in Modern Physics*, Springer-Verlag, Berlin, 1989.

[64] G. Comsa, G. Mechtersheimer, B. Poelsema, and S. Tomoda, Surf. Sci. **89**, 123 (1979).

[65] A. Zangwill, *Physics at Surfaces*, Cambridge University Press, Cambridge, 1996.

[66] J. A. Venables, G. D. T. Spiller, and M. Manbrücken, Rep. Prog. Phys. **47**, 399 (1984).

[67] M. Blanc, K. Kuhnke, V. Marsico, and K. Kern, Surf. Sci. **414**, L964 (1998).

[68] G. Brusdeylins, R. Doak, and J. Toennies, Phys. Rev. B **27**, 3662 (1983).

[69] J. Toennies, J. Vac. Sci. Technol. A. **2**, 1055 (1984).

[70] P. Zeppenfeld, K. Kern, R. David, K. Kuhnke, and G. Comsa, Phys. Rev. B **38**, 12329 (1988).

[71] D. Favias and K.-H. Rieder, Rep. Prog. Phys. **61**, 1575 (1998).

[72] P. Gambardella, Z. Sljivancanin, B. Hammer, M. Blanc, K. Kuhnke, and K. Kern, Phys. Rev. Lett. **87**, 056103 (2001).

[73] T. J. Raeker and A. E. DePristo, J. Vac. Sci. Tech. A **10**, 2396 (1992).

[74] C. Félix, G. Vandoni, W. Harbich, J. Buttet, and R. Monot, Phys. Rev. B **54**, 17039 (1995).

[75] C. de Beauvais, Y. Girard, C. Pérard, B. Croset, and B. Mutaftschier, Surf. Sci. **367**, 129 (1996).

[76] K. Kuhnke, E. Hahn, R. David, P. Zeppenfeld, and K. Kern, Surf. Sci. **272**, 118 (1992).

[77] M. Blanc, *Step Decoration and Growth at the Vicinal Pt(997) Surface*, PhD thesis, Ecole Polytechnique Fedrale de Lausanne, 1998.

[78] H. Schief, *Vicinal Surfaces as Nanoscopic Echelette Gratings for Atomic Waves and their Application to He-Surface Spectroscopy*, PhD thesis, Ecole Polytechnique Fedrale de Lausanne, 1995.

[79] V. Marsico, *Proprietes des Surfaces Metalliques Vicinales: Structure de Pt(997) et Adsorption des Gaz Rares*, PhD thesis, Ecole Polytechnique Fedrale de Lausanne, 1995.

[80] K.Kern, R.David, and G.Comsa, Rev. Sci. Instrum. **56**, 369 (1985).

[81] R. David, K. Kern, P. Zeppenfeld, and G. Comsa, Rev. Sci. Instrum. **57**, 2771 (1986).

[82] S. Sarbach, *Growth of Metallic Nanostructures on the Vicinal Pt(997) Surface*, PhD thesis, Ecole Polytechnique Fedrale de Lausanne, 2002.

[83] T. Hufnagel, M. Kautzky, B. Daniels, and B. Clemens, J. Appl. Phys. **85**, 2609 (1999).

[84] M. Abid, H. Lassri, R. Krishnan, M. Nyvlt, and S. Visnovsky, J. Mag. Mag. Mat. **214**, 99 (2000).

[85] M. Ritter, W. Ranke, and W. Weiss, Phys. Rev. B **57**, 7240 (1998).

[86] Y. Kim, C. Westphal, R. Ynzunza, Z. Wang, H. Galloway, M. Salmeron, M. V. Hove, and C. Fadley, Surf. Sci. **416**, 68 (1998).

[87] D. Jerdev and B. Koel, Surf. Sci. **513**, L391 (2002).

[88] W. Weiss and M. Ritter, Phys. Rev. B **59**, 5201 (1999).

[89] P. Gambardella, A. Dallmeyer, K. Maiti, M. Malagoli, W. Eberhardt, K. Kern, and C. Carbone, Nature **416**, 301 (2002).

[90] P. Gambardella, J. Phys. :Condens. Matter. **15**, S2533 (2003).

[91] T. Massalski, J. Murray, L. Bennett, and H. Baker, editors, *Binary Alloy Phase Diagrams*, American Society for Metals, Metals Park, Ohio, 1986.

[92] H. Okamoto, editor, *Phase Diagrams of Binary Iron Alloys*, Monograph Series on Alloy Phase Diagrams, The Materials Information Society, Materials Park, Ohio, 1993.

[93] H. King, Bull. Alloy Phase Diagrams **2**, 401 (1981).

[94] K. Simiyama, M. Shiga, M. Morioka, and Y. Nakamura, J. Phys. F, Met. Phys. **9**, 1665 (1979).

[95] A. Kussmann and G. von Rittberg, Zeitschrift fur Metallkunde **41**, 470 (1950).

[96] A. G. Jackson, *Handbook of Crystallography: For Electron Microscopists and Others*, Springer-Verlag, New York, 1991.

[97] W. Jellinghaus, Z. Tech. Phys **17**, 33 (1936).

[98] A. Christensen, A. V. Ruban, P. Stoltze, K. W. Jacobsen, H. L. Skriver, J. K. Nørskov, and F. Besenbacher, Phys. Rev. B **56**, 5822 (1997).

[99] S. Rusponi, T. Cren, and H. Brune, unpublished result, 2004.

[100] L. Davis, N. MacDonald, P. Palmberg, G. Riach, and R. Weber, *Handbook of Auger Electron Spectroscopy*, Perkin-Elmer Corp., New York, 1978.

[101] M. Schmid and P. Varga, *Segregation and Surface Chemical Ordering - an Experimental View on the Atomic Scale*, volume 10 of *The Chemical Physics of Solid Surfaces*, chapter 4, page 118, Elsevier, Amsterdam, 2002.

[102] P. Beccat, Y. Gauthier, R. Baudoing-Savois, and J. Bertolini, Surf. Sci. **238**, 105 (1990).

[103] C. Creemers and P. Deurinck, Surf. Interf. Anal. **25**, 177 (1997).

[104] D. Payer, Co-adsorption auf PtFe-legierungsschichten, Diploma Thesis, 2001, Technischen Universitaet Wien.

[105] K. Hermann and M. A. van Hove, Sarch/Latuse/Plot3d package, http://w3.rz-berlin.mpg.de/ hermann/SLP/, 2000.

[106] Z. Nishiyama, Sci. Rep. Tohoku Imperial Univ. **23**, 368 (1934).

[107] G. Wassermann, Arch. Eisenhuttenwesen **16**, 647 (1933).

[108] G. K. Kurdjumov and G. Sachs, Z. Physik **64**, 325 (1939).

[109] W. B. Pearson, *The Crystal Chemistry and Physics of Metals and Alloys*, John Wiley & Sons, Inc., New York, 1972.

[110] Q. J. Gao and T. T. Tsong, Surf. Sci. **191**, L787 (1987).

[111] G. A. Attard, R. Price, and A. Al-Akl, Surf. Sci. **335**, 52 (1995).

[112] H. Hoster, T. Iwasita, H. Baumgartner, and W. Vielstich, Phys. Chem. Chem. Phys. **3**, 337 (2001).

[113] T. Jarvi, T. Madden, and E. Stuve, Electrochem. Solid St. **2**, 224 (1999).

[114] J. C. Davies, B. E. Hayden, and D. J. Pegg, Electrochim. Acta **44**, 1181 (1998).

[115] D. Bassett, Surf. Sci. **325**, 121 (1995).

[116] K. Kuhnke and K. Kern, J. Phys. :Condens. Matter. **15**, S3311 (2003).

[117] P. Gambardella, M. Blanc, K. Kuhnke, K. Kern, F. Picaud, C. Ramseyer, C. Girardet, C. Barreteau, D. Spanjaard, and M. Desjonquères, Phys. Rev. B **64**, 045404 (2001).

[118] O. Andersen and O. Jepsen, Physica B **91**, 317 (1977).

[119] W. R. Tyson and W. A. Miller, Surf. Sci. **62**, 267 (1977).

[120] C. Kittel, *Introduction to Solid State Physics*, John Wiley & Sons, Inc., New York, 7 edition, 1996.

[121] A. Hubert and R. Schäfer, *Magnetic Domains: The Analysis of Magnetic Microstructures*, Springer-Verlag, Berlin, 1998.

[122] B. Cullity, *Introduction to Magnetic Materials*, Addison Wesley, New York, 1972.

[123] R. Celotta, D. Pierce, and J. Unguris, MRS Bull. **20**, 30 (1995).

[124] S. Gunther, B. Kaulich, L. Gregoratti, and M. Kiskinova, Prog. Surf. Sci **70**, 187 (2002).

[125] A. Kubetzka, M. Bode, O. Pietzsch, and R. Wiesendanger, Phys. Rev. Lett. **88**, 057201 (2002).

[126] S. Lovesey and S. Collins, *X-ray Scattering and Absorption by Magnetic Materials*, Oxford Series on Synchrotron Radiation, Oxford University Press, Oxford, 2000.

[127] J. Stöhr and H. Koenig, Phys. Rev. Lett. **75**, 3748 (1995).

[128] D. Attwood, *Soft X-rays and Extreme Ultraviolet Radiation: Principles and Applications*, Cambridge University Press, Cambridge, 2000.

[129] W. Gudat and C. Kunz, Phys. Rev. Lett. **29**, 169 (1972).

[130] A. Erbil, G. C. III, R. Frahm, and R. Boehme, Phys. Rev. B **37**, 2450 (1988).

[131] V. Chakarian, Y. Idzerda, and C. Chen, Phys. Rev. B **57**, 5312 (1988).

[132] B. Thole, P. Carra, F. Sette, and G. van der Laan, Phys. Rev. B **68**, 1943 (1992).

[133] M. Altarelli, Phys. Rev. B **47**, 597 (1993).

[134] P. Carra, B. Thole, M. Altarelli, and X. Wang, Phys. Rev. Lett. **70**, 1993 (1993).

[135] B. Henke, J. Smith, and D. Attwood, J. Appl. Phys. **48**, 1852 (1977).

[136] B. Henke, J. Liesegang, and S. Smith, Phys. Rev. B **19**, 3004 (1979).

[137] G. Fraser, Nucl. Instrum. Meth. **206**, 251 (1983).

[138] B. Saleh and M. Teich, *Fundamentals of Photonics*, Wiley Series in Pure and Applied Optics, John Wiley & Sons, Inc., New York, 1991.

[139] G. Schütz, R. Wienke, W. Wilhelm, W. Wagner, P. Kienle, R. Zeller, and R. Frahm, Z. Phys. B **75**, 495 (1989).

[140] T. Koide, T. Shidara, K. Yamaguchi, A. Fujimori, H. Fukutani, N. Nakajima, T. Sugimoto, T. Katayama, and Y. Suzuki, Phys. Rev. B **53**, 8219 (1996).

[141] H. Maruyama, F. Matsuoka, K. Kobayashi, and H. Yamazaki, J. Mag. Mag. Mat. **140-144**, 43 (1995).

[142] T. Shishidou, S. Imada, T. Muro, F. Oda, A. Kimura, S. Suga, T. Miyahara, T. Kanomata, and T. Kaneko, Phys. Rev. B **55**, 3749 (1997).

[143] J. C. Fuggle and N. Mårtensson, J. Electron. Spectrosc. **21**, 275 (1980).

[144] J. Erskine and E. Stern, Phys. Rev. B **12**, 5016 (1975).

[145] N. Smith, C. Chen, F. Sette, and L. Mattheiss, Phys. Rev. B **46**, 1023 (1999).

[146] J. Stöhr and R. Nakajima, IBM J. Res. Develop. **42**, 73 (1998).

[147] S. Bader, J. Mag. Mag. Mat. **100**, 440 (1991).

[148] D. Peterka, G. Haas, A. Enders, and K. Kern, Rev. Sci. Instr. **74**, 2744 (2003).

[149] R. Kubo, J. Phys. Soc. Jpn. **12**, 570 (1993).

[150] R. Wallis and M. Balkanski, *Many-body Aspects of Solid State Spectroscopy*, page 29, North-Holland, Amsterdam, 1986.

[151] D. K. Cheng, *Field and Wave Electromagnetics*, Addison-Wesley Series in Electrical Engineering, Addison-Wesley, Massachusetts, 2 edition, 1992.

[152] Z. Yang and M. Scheinfein, J. Appl. Phys. **74**, 6810 (1993).

[153] R. P. Hunt, J. Appl. Phys. **38**, 1652 (1967).

[154] J. H. Weaver, E. Colavita, D. W. Lynch, and R. Rosei, Phys. Rev. B **19**, 3850 (1979).

[155] W. Voigt, *Magneto- und Elektrooptik*, Teubner, Leipzig, 1908.

[156] J. Zak, E. Moog, C. Liu, and S. Bader, J. Mag. Mag. Mat. **89**, 107 (1990).

[157] J. Zak, E. Moog, C. Liu, and S. Bader, J. Appl. Phys. **68**, 4203 (1990).

[158] J. Zak, E. Moog, C. Liu, and S. Bader, Phys. Rev. B **43**, 6423 (1991).

[159] Z. Qiu and S. Bader, Rev. Sci. Instr. **71**, 1243 (2000).

[160] S. Müller, P. Bayer, C. Reischl, K. Heinz, B. Feldmann, H. Zilligen, and M. Wuttig, Phys. Rev. Lett. **74**, 765 (1994).

[161] B. Schirmer and M. Wuttig, Phys. Rev. B **60**, 12945 (1999).

[162] J. Shen, M. Klaua, P. Ohresser, H. Jenniches, J. Barthel, C. Mohan, and J. Kirschner, Phys. Rev. B **56**, 11134 (1997).

[163] C. Ederer, M. Komelj, and M. Fähnle, Phys. Rev. B **68**, 052402 (2003).

[164] P. Ohresser, G. Ghiringhelli, O. Tjernberg, N. B. Brookes, and M. Finazzi, Phys. Rev. B **62**, 5803 (2000).

[165] J. Shen, R. Skomski, M. Klaua, H. Jenniches, S. S. Manoharan, and J. Kirschner, Phys. Rev. B **56**, 2340 (1997).

[166] D. sheng Wang, R. Wu, and A. Freeman, Phys. Rev. B **47**, 14932 (1993).

[167] D. Wang, R. Wu, and A. Freeman, J. Mag. Mag. Mat. **129**, 237 (1994).

[168] L. Néel, J.Phys.Radium **15**, 225 (1954).

[169] Y. Millev, R. Skomski, and J. Kirschner, Phys. Rev. B **58**, 6305 (1998).

[170] R. Kawakami, E. J. Escorcia-Aparicio, and Z. Qiu, Phys. Rev. Lett. **77**, 2570 (1996).

[171] Z. Qiu and S. Bader, J. Mag. Mag. Mat. **200**, 664 (1999).

[172] D. Chuang, C. Ballentine, and R. O'Handley, Phys. Rev. B **49**, 15084 (1994).

[173] R. Skomski, H. Oepen, and J. Kirschner, Phys. Rev. B **58**, 11138 (1998).

[174] M. Hutchings, Solid State Phys. **16**, 227 (1964).

[175] R. Skomski, Phil.Mag. **70**, 175 (1994).

[176] T. Suzuki, D. Weller, C. Chang, R. Savoy, T. Huang, B. Gurney, and V. Speriosu, Appl. Phys. Lett. **64**, 2736 (1994).

[177] C. Chantler, J. Phys. Chem. Ref. Data **24**, 71 (1995).

[178] C. Chantler, J. Phys. Chem. Ref. Data **29**, 597 (2000).

[179] V. Anisimov and M. Korotin, Phys. Met. Metall. **68**, 53 (1989).

[180] M. Podgórny, Phys. Rev. B **43**, 11300 (1991).

[181] J.-C. Shih, H.-H. Hsiao, J.-L. Tsai, and T.-S. Chin, IEEE. Trans. Magn. **37**, 1280 (2001).

[182] T. Suzuki, T. Kiya, N. Honda, and K. Ouchi, J. Mag. Mag. Mat. **235**, 312 (2001).

[183] R. F. C. Farrow, D. Weller, R. F. Marks, M. F. Toney, D. J. Smith, and M. R. McCartney, J. Appl. Phys. **84**, 934 (1998).

[184] R. F. C. Farrow, D. Weller, R. F. Marks, M. F. Toney, A. Cebollada, and G. R. Harp, J. Appl. Phys. **79**, 5967 (1996).

[185] C.-M. Kuo, P. C. Kuo, and H.-C. Wu, J. Appl. Phys. **85**, 2264 (1999).

[186] M. Sakurai, Phys. Rev. B **50**, 12945 (1994).

[187] T. Shishidou, T. Muro, F. Oda, A. Kimura, S. Imada, S. Suga, S. Y. Park, T. Miyahara, T. Kaneko, and T. Kanomata, J. Electron. Spectrosc. **78**, 267 (1996).

[188] S. Imada, T. Shishidou, T. Muro, S. Suga, H. Maruyama, K. Kobayashi, H. Yamazaki, and T. Kanomata, Physica B **237**, 369 (1997).

[189] K. Shinagawa, *Faraday and Kerr Effects in Ferromagnets*, chapter 5, page 137, Magneto-Optics: Springer Series in Solid-State Sciences, Springer-Verlag, Berlin, 2000.

[190] D. R. Eisner and T. L. Einstein, Surf. Sci. **286**, L559 (1993).

[191] M. A. van Hove and G. A. Somorjai, Surf. Sci. **92**, 489 (1980).

[192] J. Horvath and A. Gellman, J. Am. Chem. Soc. **124**, 2384 (2002).

[193] M. Hoogeman, D. Schloßer, J. Sanders, L. Kuipers, and J. Frenken, Phys. Rev. B **53**, R13299 (1996).

[194] E. Jahnke, F. Emde, and F. Losch, *Table of Special Functions*, Teubner, Leipzig, 1960.

[195] R. Skomski and J. Coey, J. Mag. Mag. Mat. **140**, 965 (1995).

Curriculum Vitae

Name:	Tae-Yon Lee
Date of Birth:	August 31, 1975
Nationality:	Republic of Korea (South Korea)

1995–1999	Undergraduate studies in materials science and engineering at the Seoul National University in Seoul, Korea
1999–2001	Master studies in materials science and engineering at the Seoul National University in Seoul, Korea
1999–2001	Research and teaching assistant in the group of Prof. Ki-Bum Kim at the school of materials science and engineering of the Seoul National University in Seoul, Korea
1999–2001	Joint research studies with the group of Dr. Byungki Cheong at the Electronic Materials and Device Research Center of the Korea Institute of Science and Technology (KIST) in Seoul, Korea
2001	Master thesis: **"A Study on the Recording Layer made with $(GeSbTe)_{1-x}(SnBiTe)_x$ Thin Film for Phase Change Optical Storage"**, Seoul National University, Korea
2001-2005	Ph.D. study in experimental physics at the Max-Planck-Institute of Solid State Research in Stuttgart, Germany
2005	Ph.D. thesis: **"Growth and Magnetism of Low-Dimensional Metallic Nanostructures on the Pt(997) Surface"**, The Swiss Federal Institute of Technology Lausanne, Switzerland

Acknowledgement

In the course of writing this thesis, I come to realize that I'm finishing another chapter of my life with a few knowledge which is not sufficient yet. At least, I can point out what I don't know regarding what I did. And I have to admit that all the works along with such lessons cannot be achieved without helps and concerns from a number of people and institutions.

A first thank should go to my thesis advisor, Prof. Klaus Kern, whose ongoing interests and supports have made the research project possible. I appreciate the advices and concern of Prof. Ki-Bum Kim, who understood my situation and motivated to start this research in Stuttgart, not in Seoul. I have to acknowledge an one year financial support from the Korean Ministry of Education and Human Resources Development through the program of the Brain Korea 21 through Materials Education and Research division in Seoul National University. I thank Prof. Francis Lévy and Prof. Danilo Pescia for the kind reading of the thesis and presence as members of jury.

This research would not be possible without the coordination and instruction of Dr. Klaus Kuhnke. He showed me the attitude of being serious and careful to every aspect of research. I appreciate also his careful reading of the thesis. Dr. Axel Enders is the researcher and colleague who showed me the way of having a efficient strategy to tackle a given problem. He also showed me how to drive a car manually in Trieste. Vielen Dank! I'm also grateful to Dr. Jan Honolka. With him, I have been always stimulated and encouraged to be more exact. I'd like to express my gratitude to Dr. Samuel Sarbach for his kind advices and discussion in the TEAS experiments. I'm grateful to Dr. Peter Wahl. He was my office-mate, and I remember we had a lot of dialogues which were related not only to the research but also to the normal life. I thank Diego Repetto for his assistance of MOKE experiments as well as relaxed and humorous response to me. I'm grateful to Dr. Ulrich Starke for the useful discussion on the LEED experiments and careful reading of my thesis. And I thank all the staffs in MPI-FKF in Stuttgart I have omitted. I appreciated their efforts and helps nontheless.

This thesis cannot be made without the support from several synchrotron facilities.